Sune Hansborg Pettersen

Subject Specific Finite Element Analysis of Bone

for evaluation of the healing of a leg lengthening and evaluation of femoral stem design

Thesis for the degree of Philosophiae Doctor

Trondheim, May 2009

Norwegian University of Science and Technology
Faculty of Engineering Science and Technology
Department of Structural Engineering

NTNU
Norwegian University of
Science and Technology

NTNU
Norwegian University of Science and Technology

Thesis for the degree of Philosophiae Doctor

Faculty of Engineering Science and Technology
Department of Structural Engineering

ISBN 978-82-471-1579-4 (printed ver.)
ISBN 978-82-471-1580-0 (electronic ver.)
ISSN 1503-8181

Doctoral theses at NTNU, 2009:99

Printed by NTNU-trykk

Summary

The present thesis concerns employing the finite element method together with computed tomography to solve problems relevant to clinical orthopaedics.

The first part of the thesis describes a procedure of relating the gray-scale values from computed tomography to the local density of bone. Calibration procedures used today, simplify the composition of bone to consist of bone mineral and water-equivalent organic tissue. The procedure described in the present thesis accounts for both the mineral, collagen and fluid content in bone.

The geometry of the bone is extracted from the CT images to build the finite element models and assigned material properties according to local densities derived from the gray-scale values. Two different methods of building finite element models are described; voxel-based models, and geometry-based models.

Voxel-based finite element models are generated directly from the tomographic images and are thus relatively easy to use to study the stiffness of a bone segment. The voxel-based models are here used to assess the mechanical stability of a leg lengthening.

Geometry-based models are created by segmenting the tomographic images and building a 3D model, which in turn is meshed to create the finite element models. These models can be used to simulate surface conditions between implants and bone. They are here used to simulate the stress-shielding effect and stability of a cementless femoral stem in human cadaver femurs.

Acknowledgements

The present thesis is submitted to the Norwegian Unitversity of Science and Technology (NTNU) for the degree Philosophiae Doctor. The work was carried out at the Norwegian Orthopaedic Implant Research Unit (NKSOI) and the Department of Structural Engineering at NTNU. The project was funded by NKSOI.

I would like to extend my appreciation to professor Bjørn Skallerud, who has been my supervisor ever since I first ventured into the field of biomechanics during my Master degree back in 2002. Bjørn has been the primus motor of establishing the biomechanics division at the Department of Structural Engineering, and I would like to thank him for all his support and helpful advice through all these years. I would also like to thank my co-supervisor dr. Arild Aamodt at the Department of Orthopaedic Surgery. His experience in orthopaedics and biomechanical testing of implants has been of great value to me.

Radiographer Liv Nesje at St. Olavs Hospital has been very important for the work presented in this thesis. Always helpful whenever I needed to get something CT scanned. Her positive attitude and cooperation has been an immense help.

I have been fortunate to be surrounded by supportive and inspirational co-workers at NKSOI. Without them, I would never have started or completed this work. I would like to extend my sincere gratitude to: Kristin Haugan for her cheerful humour, keeping up the spirit on dark and rainy days. Jomar Klaksvik, head of the biomechanics laboratory and fellow engineer, for all the good discussions on technical and not-so-technical matters. Tina S. Wik for all her constructive criticism during the preparation of articles. Olav Foss, orthopaedic surgeon and my boss, for all his encouragment and support.

... and last but not least, a big "Thank You" to my dear parents for all their love and care, and for not asking too many questions about work whenever I came home on vacations.

Table of contents

Chapter 1: General introduction

The primary functions of bones are to provide mechanical support for the body and protect vital organs. The shape of bones is strictly functional, and can be seen at muscle attachment sites where bony ridges and protuberances, like the greater and lesser trochanter, provide lever arms for the muscles and give increased mobility. That the geometry of bones follows function is shown not only on the macroscale, but also in its microstructural architecture. Already in the 19th century, scientists noted that the trabecular orientation in cancellous bone reflected the stress and strain pattern in the bone (Huiskes, 2000). Also in cortical bone, canals and lamellar structure of the bone are found to align in the principal load directions (Petrtyl et al., 1996). The shape and microstructure of bones is not only determined by our genetics, but also adapts according to loading history, hormonal changes and the healing of injuries. Thus, we can recognise the same characteristic shapes of bones between different species, such as in a leg of lamb and a human femur. Conversely, we can also see a wide variation in geometry and mechanical properties among individuals of the same species.

The development in computational mechanics and tomographic methods of medical imaging has enabled us to study the biomechanics of bones in a new way. Computed tomography (CT) can be used to noninvasively retrieve the bone geometry and determine its local material properties. Methods of computational mechanics, such as the finite element (FE) method, is a versatile tool that can be used analyse load configurations that are difficult to replicate experimentally and access stress and strain results from areas not accessible for measurements. By coupling these two together, FE models can be built that include both the individual geometry and mechanical properties of a patient. Such subject specific FE models have been used to analyse stress and strain patterns in bone (Lengsfeld et al., 1998), predict fracture (Keyak et al., 1998) and to simulate the course of adaptive bone remodelling around implants (Rietbergen et al., 1993). Although FE models are used extensively in construction and the industry in general, the employment of FE models in medicine has been largely limited to academic studies. In the present work two applications of subject specific FE models will be presented. Both examples are based on CT images, but differ in the type of cases they are used on, the way the FE models are built, and the way the analyses are run.

The first example concerns how subject specific FE models could be employed on patients undergoing limb lengthening in order to estimate the mechanical stability of the bone regenerate and determine when to remove the external fixation. Today, orthopaedic surgeons assess the mechanical stability of limb lengthenings from plain radiographs, and studies have reported refracture rates due to premature frame removal of 10-20% (Marsh et al., 1997; Forriol et al., 1999; Maini et al., 2000; Simpson and Kenwright, 2000; Garcia-Cimbrelo and Marti-Gonzalez, 2004). We have written a program that generates FE models directly from the CT scans, and can be used by persons without any specific training in computational mechanics. The generation of the FE models and analysis is largely automated, and is usually finished within a few minutes. It is therefore a tool that can be used by the orthopaedic surgeon in the treatment of the patient.

The second example concerns the pre-clinical evaluation of hip implants. New prosthetic designs undergo in vitro mechanical testing using human cadaver bones before being introduced on the market. In the present thesis, subject specific FE models of human femurs are used to simulate the type of testing used for pre-clinical evaluation of hip implants. In this case, the FE models are not generated from the CT images directly. Instead, segmentation techniques are used to extract contours from the CT images and reconstruct a 3D model of the bone, before generating the FE models. Both the construction and analyses of the FE models are very time consuming; requiring several hours for building the model, and sometimes several days to complete the calculations. This kind of FE analyses requires an operator trained in computational mechanics. These subject specific FE models are not meant to be used in the direct treatment of patients, but rather in the development process and testing of new implants.

The thesis is organised as follows. Chapter 2 describes the attenuation of x-rays in different materials, and explain how this was employed to calculate the material properties of bone from the CT attenuation values. The procedure of leg lengthening and how to assess stability of the lengthened section with subject specific FE models is covered in the Chapter 3. Chapter 4 concerns the procedure of building the subject specific FE models for testing hip implants.

References

Forriol, F., Iglesias, A., Arias, M., Aquerreta, D., Canadell, J., (1999). Relationship between radiologic morphology of the bone lengthening formation and its complications. J.Pediatr.Orthop B 8, 292-298.

Garcia-Cimbrelo, E., Marti-Gonzalez, J. C., (2004). Circular external fixation in tibial nonunions. Clin.Orthop Relat Res. 65-70.

Huiskes, R., (2000). If bone is the answer, then what is the question? J.Anat. 197 (Pt 2), 145-156.

Keyak, J. H., Rossi, S. A., Jones, K. A., Skinner, H. B., (1998). Prediction of femoral fracture load using automated finite element modeling. J.Biomech. 31, 125-133.

Lengsfeld, M., Schmitt, J., Alter, P., Kaminsky, J., Leppek, R., (1998). Comparison of geometry-based and CT voxel-based finite element modelling and experimental validation. Med.Eng Phys. 20, 515-522.

Maini, L., Chadha, M., Vishwanath, J., Kapoor, S., Mehtani, A., Dhaon, B. K., (2000). The Ilizarov method in infected nonunion of fractures. Injury 31, 509-517.

Marsh, D. R., Shah, S., Elliott, J., Kurdy, N., (1997). The Ilizarov method in nonunion, malunion and infection of fractures. J.Bone Joint Surg Br. 79, 273-279.

Petrtyl, M., Hert, J., Fiala, P., (1996). Spatial organization of the haversian bone in man. J.Biomech. 29, 161-169.

Rietbergen, B. v., Huiskes, R., Weinans, H., Sumner, D. R., Turner, T. M., Galante, J. O., (1993). ESB Research Award 1992. The mechanism of bone remodeling and resorption around press-fitted THA stems. J.Biomech. 26, 369-382.

Simpson, A. H., Kenwright, J., (2000). Fracture after distraction osteogenesis. J.Bone Joint Surg.Br. 82, 659-665.

Chapter 2: Relating CT gray-scale values to bone density

2.1 Background

Computed tomography (CT) is regularly used in biomechanics as it provides a noninvasive method for retrieving the geometry of bones and estimating local material properties. It is commonly known that the attenuation of electromagnetic radiation in a material depends on the density and chemical composition of the material (Rutherford et al., 1976). It is also commonly known that the mechanical properties (elastic stiffness and strength) of bone are highly dependent on its density (Carter and Hayes, 1977; Keller, 1994). The question that will be addressed in the present chapter is how the gray-scale pixel values, or attenuation values, in the CT images can be linked to the density of bone.

Calibration phantoms are often used to link the pixel attenuation values of CT scans to a standardized unit of measure. They are made up of different materials with known mineral content. Thus, from the gray-scale values of the different phantom materials in the images, one can establish a relationship between mineral content and CT attenuation values. Dipotassium phosphate (K_2HPO_4) is soluble in water, and has radiographic properties similar to bone mineral - calcium hydroxyapatite (HA). Cann et al. (1985) therefore employed K_2HPO_4 dissolved in water to make a calibration phantom. However, problems with liquid calibration phantoms due to bubble formation in the solution and evaporation through imperfect seals were reported, and solid calibration standards using mixtures of calcium HA and water equivalent polymer were introduced instead (Goodsitt, 1992). The composition of the solid phantom was kept as simple as possible - only calcium HA and water equivalent polymer - to avoid discussion about the proportions of the non-mineral components of bone (Kalender et al., 1995). However, apart from calcium HA and water, bone also contains a considerable portion of collagen which has a higher density than water. In theory, the calibration phantoms will therefore give an overestimation of the mineral content in bone because they ignore that collagen will attenuate more radiation than water due to its higher density. The calcium HA phantom has been found to overestimate bone mineral density by approximately 15% (Kaneko et al., 2003; 2004; Schileo et al., 2008). Keyak et al. (1994) found the K_2HPO_4 phantom to give an accurate estimate of the bone mineral content, while Les et al. (1994) found it to underestimate bone mineral content by almost 20%! The question therefore remains: what is the relationship between the density of bone and the CT attenuation values?

Some studies of subject specific FE models use the calibration coefficients derived directly from the phantom (Bessho et al., 2006; Taddei et al., 2006; Reggiani et al., 2007), while others adjust for the over- and underestimation of the calibration phantom (Schileo et al., 2008; Trabelsi et al., 2009; Yosibash et al., 2007; Keyak and Falkinstein, 2003; Keyak and Rossi, 2000). In the present chapter an alternative approach will be described for relating the pixel attenuation values of a CT scan to the density of bone tissue. The attenuation of radiation in different materials has been described in studies concerning radiotherapy and radiation dose calculation (Rutherford et al., 1976; Schneider et al., 1996; Watanabe, 1999; Schneider et al., 2000). Instead of using a traditional calibration phantom with materials representing different degrees of tissue mineralization, we will take the long route via radiation physics to derive a relationship between bone density and CT attenuation values. First, the procedure for characterising the emitted x-ray spectrum will be described. Secondly, the calibration phantom will be presented; the different materials used and their chemical composition, and how the pixel values for each phantom material are obtained from the CT images. Thirdly, a relation between the density and the chemical composition of bone is set up, which is then employed to convert the CT pixel values into bone mineral density. Finally in this chapter, the different conversion factors used in our subject specific FE models will be presented and compared to conversion factors reported in literature.

2.2 Characterising the x-ray spectrum

The pixel value in a CT image gives a measure of how much radiation is attenuated in the material at the location of the pixel, the linear attenuation coefficient ($\overline{\mu}$). The pixel values are given in Hounsfield units (HU), which means that they are normalised according to the linear attenuation coefficient in water:

$$HU = 1000 \cdot \left(\frac{\overline{\mu}}{\overline{\mu}_{H_2O}} - 1 \right), \tag{2.1}$$

The pixels are stored as 12-bit values, and have a range from -1024 to 3071. As defined by equation (2.1), water has a HU value of zero. The attenuation of x-rays in air is practically zero, which gives a HU value of -1000. In bone the values might range between 200 and 600 HU for cancellous bone and between 1000 and 2000 HU for cortical bone.

The total attenuation of x-rays in a material depends on the material density, composition and the radiation spectrum from the x-ray tube. In materials with a chemical composition (or effective atomic number) close to water, the HU values will remain largely unaffected by changes in the x-ray spectrum. In bone, however, photons will be attenuated differently due to its calcium content. The relationship between HU values and mineral density will therefore depend on the x-ray spectrum used in the CT scanner. In explaining how x-rays are absorbed and how we can use CT attenuation values to estimate bone mineral density, we will start by explaining a little about the x-ray tube and how x-rays are absorbed in the tissue.

The radiation from the x-ray tube is made up of a spectrum of photon energies that depends on different parameters. The x-rays are produced by accelerating electrons in an electric field determined by the electric potential (x-ray tube voltage, kV) between the cathode and anode (figure 2.1). The kinetic energy of the electrons is equal to electric potential multiplied by the electron charge. Hence, an x-ray tube voltage of 80 and 140 kV gives the electrons a kinetic energy of 80 and 140 keV, respectively. The electrons hit the anode and are decelerated by the material, thereby producing electromagnetic radiation, socalled braking radiation or *Bremsstrahlung*.

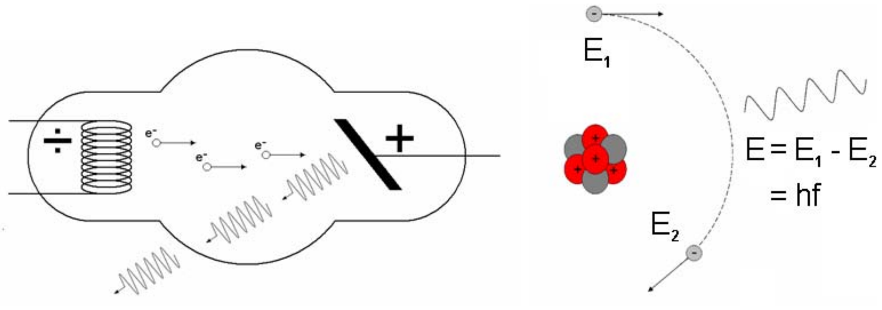

Figure 2.1: Principle sketch of the X-ray tube (left) and production of braking radiation in the anode material (right).

If the electron is completely decelerated in one single interaction with an atom, all the kinetic energy of the electron is converted into one single photon with the exact same energy. The highest photon energy that can be produced by the x-ray tube is therefore equal to the kinetic energy of the electrons. However, in most cases the electron is slowed down in several stages producing several lower energy photons and creating a continuous spectrum of radiation energies.

Electrons in an atom are organised in shells (K-, L- and M-shell) around the nucleus. In some cases an incident electron collides with electrons around the nucleus and ejects the electron from its shell. Another electron from an outer shell must then replace the ejected electron, thereby emitting a photon with energy equal to the difference in energy of the two shell positions. Tungsten, which is usually used for x-ray machines and CT scanners, has binding energies of 69.5, 11.5 and 2.5 keV (Seibert, 2004) for the K-, L- and M-shells, respectively. An electron from the L- or M-shell jumping down to the K-shell would thus produce photons with energies 58 keV and 67 keV. Since electron shell binding energies are characteristic for the chemical element, this type of radiation is called characteristic radiation. The characteristic radiation of the anode material is shown as sharp peaks in the x-ray spectrum (figure 2.2).

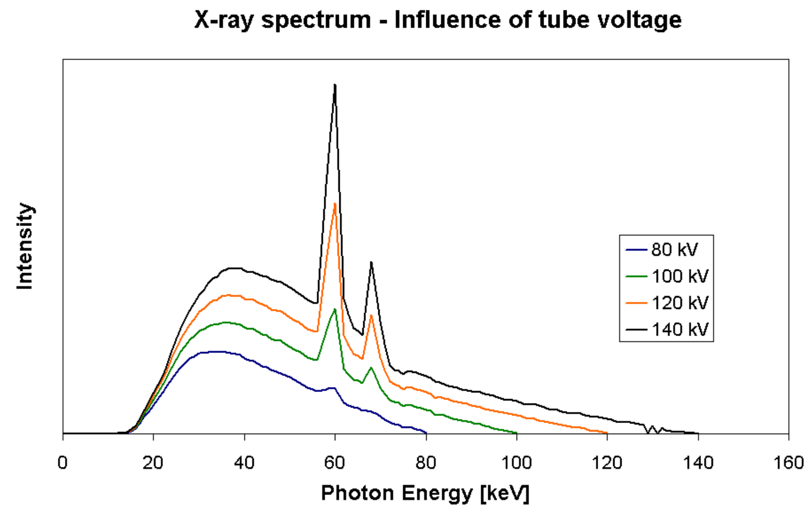

Figure 2.2: The output radiation from the X-ray tube with tungsten anode at different peak voltages. The graphs were created using the TASMIP algorithm (Boone and Seibert, 1997).

Attenuation of x-rays in a material is a combination of different absorption and scattering effects - mainly photoelectric absorption, Rayleigh scattering and Compton scattering. For the range of photon energies used in clinical radiology (figure 2.3), the degree of photoelectric absorption and Rayleigh scattering depends on photon energy, while the degree of Compton scattering remains largely constant. In biological tissue photoelectric absorption dominates for photon energies lower than 25 keV, while Compton scattering dominates for photon energies higher than 25 keV (Dance, 2003). One property that distinguishes Compton scattering from photoelectric absorption and Rayleigh scattering, is that the latter are highly dependent on the atomic number (Z) of the absorbing material. Compton scattering is usually described using the Klein-Nishina formula (Seibert and Boone, 2005) which defines it as invariant of atomic number.

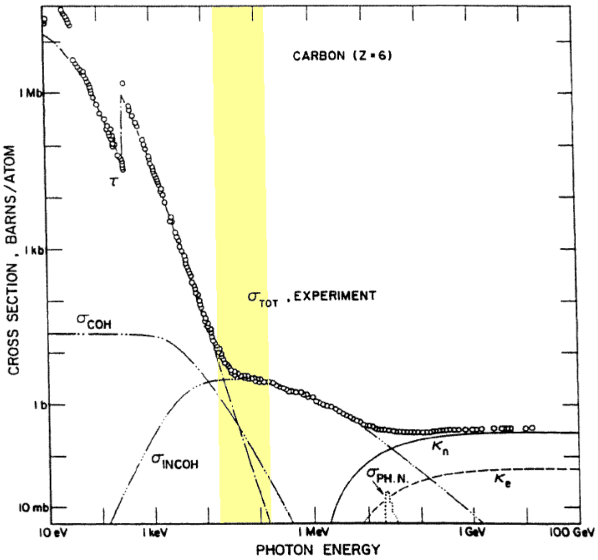

Figure 2.3: The contributions of photoeletric absorption (τ), Compton scattering (σ_{INCOH}) and Rayleigh scattering (σ_{COH}) in carbon at different photon energies (reproduced from Hubbell (1999)). The highlighted area marks the range photon energies in clinical radiology (17 to 150 keV).

For monochromatic radiation the linear attenuation coefficient , μ, in a mixed material can be expressed as (Schneider et al., 2000):

$$\mu(E)=\rho\cdot N_A\cdot\sum_i\left[\frac{w_i}{A_i}\left(Z_i\cdot K_C(E)+Z_i^{2.86}\cdot K_R(E)+Z_i^{4.62}\cdot K_\tau(E)\right)\right], \tag{2.2}$$

where ρ is the material density, N_A is Avogadro's number and w_i, A_i and Z_i is the weight fraction, atomic weight and atomic number of the ith chemical component. K_C, K_R and K_τ are the coefficients of Compton scattering, Rayleigh scattering and photoelectric absorption for a given photon energy (E). The exponentials of Compton and Rayleigh scattering were determined experimentally by Rutherford et al. (1976). The total attenuation in the material depends on the distribution of photon energies from the x-ray tube. Schneider et al. (2000) expressed the total attenuation coefficient for polychromatic radiation as:

$$\bar{\mu}=\rho\cdot N_A\cdot\sum_i\left[\frac{w_i}{A_i}\left(Z_i\cdot\bar{K}_C+Z_i^{2.86}\cdot\bar{K}_R+Z_i^{4.62}\cdot\bar{K}_\tau\right)\right], \tag{2.3}$$

where the superscript bar denotes that these are the mean values for a polychromatic spectrum. By expressing the total attenuation of a material relatively to that of water we get:

$$\frac{\bar{\mu}}{\bar{\mu}_{H_2O}}=\frac{\rho}{\rho_{H_2O}}\cdot\frac{\sum_i\left[\left(w_i/A_i\right)\cdot\left(Z_i+Z_i^{2.86}\cdot k_1+Z_i^{4.62}\cdot k_2\right)\right]}{\left(w_H/A_H\right)\cdot\left(1+k_1+k_2\right)+\left(w_O/A_O\right)\cdot\left(8+8^{2.86}\cdot k_1+8^{4.62}\cdot k_2\right)},\tag{2.4}$$

where

$$k_1\equiv\frac{\bar{K}_R}{\bar{K}_C}\text{ and }k_2\equiv\frac{\bar{K}_\tau}{\bar{K}_C}.\tag{2.5}$$

The values of k_1 and k_2 will be determined using a calibration phantom with materials with known densities and chemical composition. Their values are found by iterating on k_1 and k_2 until the error between HU values calculated for the different phantom materials and HU values measured in the CT images reaches a minimum:

$$Error=\sum_n\left\{\left[\frac{\bar{\mu}}{\bar{\mu}_{H_2O}}\left(k_1,k_2\right)\right]_n-\left[\frac{HU_{measured}}{1000}+1\right]_n\right\}^2,\tag{2.6}$$

where n is the number of phantom material. The values k_1 and k_2 tell us the amount of Rayleigh scattering and photoelectric absorption relative to Compton scattering for the given x-ray spectrum.

2.3 CT calibration phantom

The calibration phantom used in the present thesis was made from materials spanning a wide range of atomic numbers and material densities. The phantom consists of rods and tubes with different materials (figure 2.4): water, polyoxymethylene (POM), polyvinylidene fluoride (PVDF), teflon, calcium carbonate powder ($CaCO_3$), polymethyl methacrylate (PMMA; MelioDent Rapid Repair, Heraus Kulzer GmbH, Germany) and four different mixtures of PMMA and $CaCO_3$ (20%, 40%, 60% and 70% by weight of $CaCO_3$).

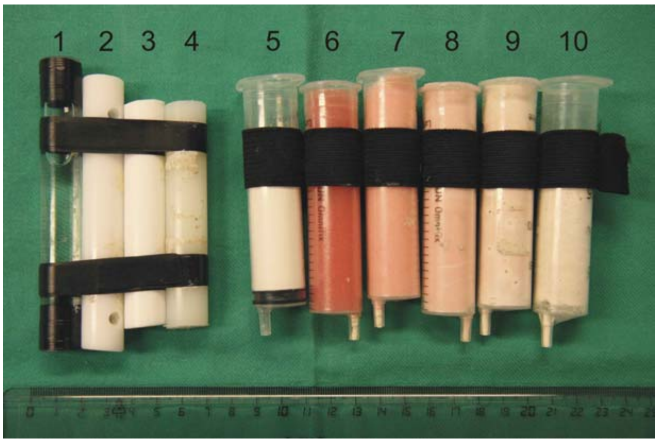

Figure 2.4: The different materials of the calibration phantom: water (1), POM (2), Teflon (3), PVDF (4), $CaCO_3$ powder (5), PMMA (6), 20% $CaCO_3$ (7), 40% $CaCO_3$ (8), 60% $CaCO_3$ (9) and 70% $CaCO_3$ (10).

For a material with a given chemical composition we can calculate the elemental weight fraction:

$$w_i = \frac{n_i \cdot A_i}{\sum_j n_j \cdot A_j}, \tag{2.7}$$

where n_i is the number of atoms of the ith chemical component in a molecule consisting of j chemical components. Table 2.1 shows the densities, elemental weight fractions and effective atomic numbers of the phantom materials. The effective atomic numbers of a compound with respect to photoelectric absorption and Rayleigh scattering are defined as (Watanabe, 1999):

$$Z_{\tau,R} = \left(\sum_i \xi_i \cdot Z_i^{(m-1),(n-1)} \right)^{1/(m-1),(n-1)}, \tag{2.8}$$

where m is 4.62 and n is 2.86, which are identical to the exponentials of photoelectric absorption and Rayleigh scattering in equation (2.2) and (2.3). ξ_i is the electron fraction of the ith chemical component for a compound made up of a total of j chemical components:

$$\xi_i = \frac{n_i \cdot Z_i}{\sum_j n_j \cdot Z_j} = \frac{w_i \cdot Z_i}{A_i} \cdot \left(\sum_j \frac{w_j \cdot Z_j}{A_j} \right)^{-1} \tag{2.9}$$

Table 2.1: Density and chemical composition of the phantom materials. Z and A is the atomic number and atomic weight of each chemical element (hydrogen, H; carbon, C; oxygen, O; fluoride, F; calcium, Ca). Z_τ and Z_R are the *effective* atomic numbers of the phantom material for photoelectric absorption and Rayleigh scattering, respectively.

Material	**Density***	**Elemental weight fractions, %**					**Z_τ**	**Z_R**
	[g/cm^3]	**H** Z=1, A=1.008	**C** Z=6, A=12.01	**O** Z=8, A=16.00	**F** Z=9, A=19.00	**Ca** Z=20, A=40.08		
Water H_2O	1.00	11.19	-	88.81	-	-	7.52	7.12
POM $[H_2CO]_n$	1.40	6.71	40.00	53.29	-	-	7.05	6.72
Teflon $[C_2F_4]_n$	2.16	-	24.02	-	-	-	7.64	7.56
PVDF $[H_2C_2F_2]_n$	1.79	3.15	37.51	-	59.34	-	7.99	7.65
$CaCO_3$ (powder)	1.25	-	12.00	47.96	-	40.04	15.73	13.78
PMMA $[C_5H_8O_2]_n$	1.1	8.05	59.98	31.96	-	-	6.58	6.21
PMMA+20% $CaCO_3$	1.23	6.44	50.39	35.16	-	8.01	10.39	8.10
PMMA+40% $CaCO_3$	1.42	4.83	40.79	38.36	-	16.02	12.28	9.72
PMMA+60% $CaCO_3$	1.62	3.22	31.19	41.56	-	24.02	13.65	11.17
PMMA+70% $CaCO_3$	1.76	2.42	26.4	43.16	-	28.03	14.23	11.85

*apparent density, mass per bulk volume.

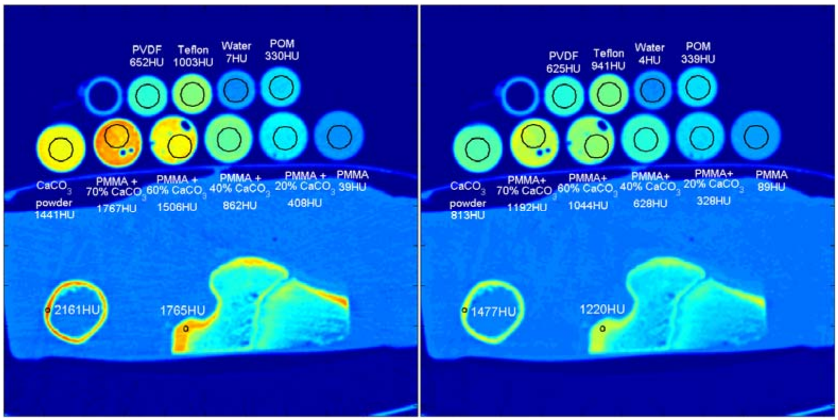

Figure 2.5: Two CT scans showing the calibration phantom and two bone specimen at 80 kV (left) and 140 kV (right). The materials with atomic density higher than water exhibit a considerable shift in HU values from 80kV to 140kV. The same effect is observed in bone.

Figure 2.5 shows that the x-ray tube voltage does not have any notable effect on the attenuation in polymers which have effective atomic numbers close to that of water. At lower voltages photoelectric absorption and Rayleigh scattering is much more prevalent and x-rays are much more effectively absorbed in materials with higher effective atomic number. This shift in attenuation is very clear for the chambers with high amount of $CaCO_3$ powder, and can also be observed in the bone samples in the CT scans.

We will now explain the basic steps of our program written to obtain the HU values of the phantom and calculate k_1 and k_2 for different x-ray tube voltages. Two CT images representing the top and bottom end of a phantom section were selected. Circles were drawn in the images to define the ends of a cylinder for each phantom material. HU values for each phantom material were collected from all CT images within the defined cylinder (figure 2.6, right).

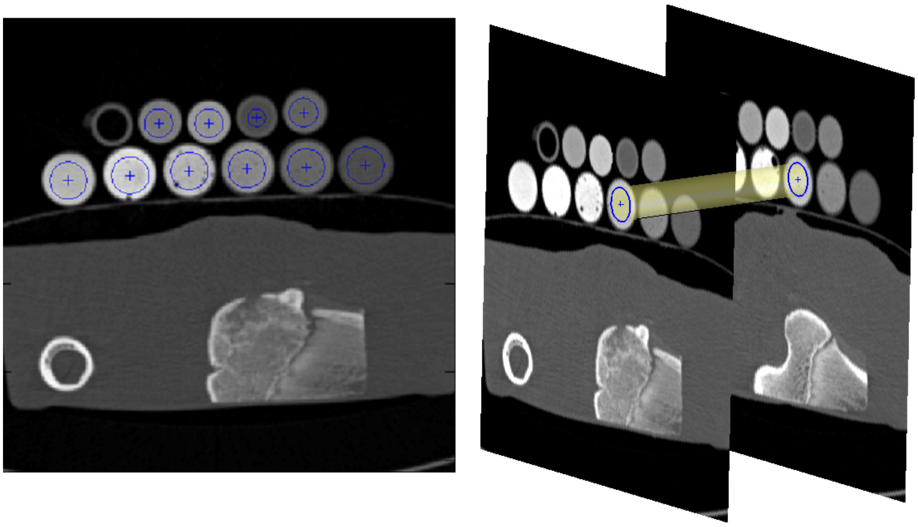

Figure 2.6: Circles drawn on the CT scan, marking the location of each phantom material (left). The yellow cylinder (right) between the circle pair of one phantom material, marks were the HU values should be collected in the CT scans lying inbetween.

Figure 2.7 shows that some of the phantom materials have a small peak at -1000 HU telling us that they contain some small pores of air, which can also be seen in the CT scans in figure 2.5 and figure 2.6. To avoid the pores and other flaws in the phantom materials from influencing the calculations, the median HU value of each phantom chamber were used to estimate k_1 and k_2, rather than the mean value. The values of k_1 and k_2 were calculated by minimizing the error in equation (2.6) through iteration. Values of k_1 and k_2 obtained at different x-ray tube voltages are given in table 2.2.

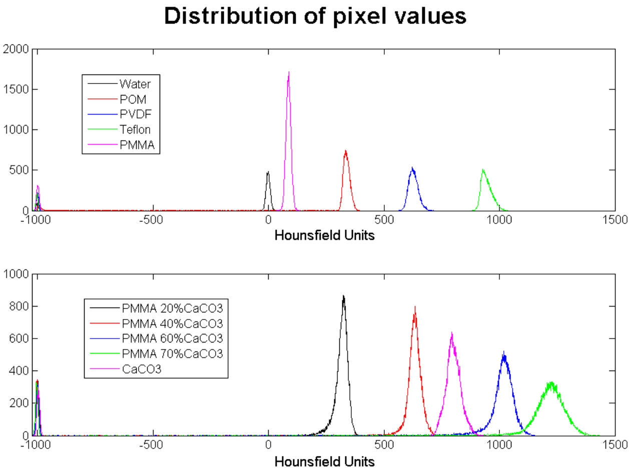

Figure 2.7: Distribution of CT pixel values (HU) obtained from the different phantom materials at 140 kV x-ray tube voltage. Some of the phantom materials have a small secondary peak at -1000HU, due to small pores of air.

Table 2.2: Estimates of k_1 and k_2 at different x-ray tube voltages.

X-ray tube voltage [kV]	k_1	k_2
80	$3.280 \cdot 10^{-3}$	$5.240 \cdot 10^{-5}$
100	$1.680 \cdot 10^{-3}$	$3.960 \cdot 10^{-5}$
120	$1.196 \cdot 10^{-3}$	$3.173 \cdot 10^{-5}$
140	$0.740 \cdot 10^{-3}$	$2.760 \cdot 10^{-5}$

The values of k_1 and k_2 in table 2.2 show how photoelectric absorption and Rayleigh scattering decreases when increasing the x-ray tube voltage. Schneider et al. (2000) reported $k_1=1.24 \cdot 10^{-3}$ and $k_2=3.06 \cdot 10^{-5}$ at 120 kV, which is very close to our values.

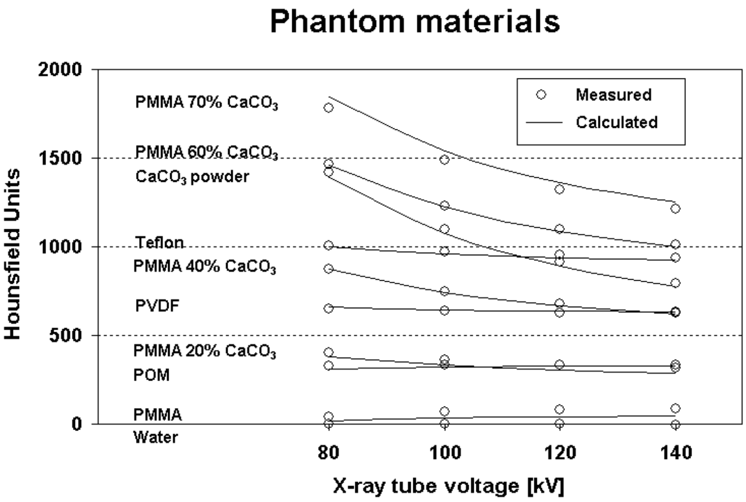

Figure 2.8: The measured HU values of the phantom together with calculated values based on estimates of k_1 and k_2.

Figure 2.8 shows that the effective atomic number of a material together with x-ray tube voltage plays an important role for the HU value of the material. Carbon based materials like polymers and organic tissues usually have effective atomic number close to that of water (see table 2.1), and the HU values of these materials are therefore not particularly affected by changes in the x-ray tube current. Mineralized tissue, however, has a higher effective atomic number than water due to its calcium content, and is therefore affected by x-ray tube voltage.

2.4 The composition of bone tissue

The relation between bone composition and mechanical properties has been subject to extensive research, and bone is usually treated as a mix of collagen, calcium hydroxyapatite (calcium HA) and water (Hellmich and Ulm, 2002; Lees, 2003; Raum et al., 2006). Cortical bone has a dense structure, with a porosity of 5-10% (Martin et al., 2007), forming the outer wall or shell around the bones. Cancellous bone, or trabecular bone, is found in the ends of long bones and inside flat and cuboidal bones, and has a porosity of approximately 75-95% (Martin et al., 2007). The marrow in the pores can be characterised as two distinct types; red bone marrow which is active in the formation of blood cells and has a high water content, and yellow marrow which largely consists of fat cells. The water content of bone marrow is around 80% in children and drops to 50% in elderly people (Ishijima et al., 1996), which means that red marrow is converted into yellow marrow with aging. The density of bone marrow has been reported to be 1.03 and 0.98 g/cm^3 (Goodsitt et al., 1991) for red and yellow bone marrow, respectively. Lunde et al. (2008) extracted the fluid from morsellized bovine bone, and found it to have a density of 1.0 g/cm^3 despite a very high fat content (~80%).

In order to calculate the chemical composition of bone, we will make the following assumptions:

1. The ash fraction (α) is constant at 0.6 (Hernandez et al., 2001; Schileo et al., 2008).
2. The amount of fluid bound in the bone tissue is negligible (Broz et al., 1995). Bone tissue consists only of calcium HA and collagen, and fluid is only found in the pores and canals.
3. The bone fluid and marrow has a density of 1.0 g/cm^3, and is a mixture of water and fat.

From the assumptions above we can define the mineral ($\rho_{\min}$) and apparent (ρ_{app}) density of bone, and establish a relationship between the two:

$$\rho_{min} = \frac{m_{HA}}{V_{tot}} \tag{2.10}$$

$$\rho_{app} = \frac{m_{HA} + m_{coll}}{V_{tot}} \tag{2.11}$$

$$\alpha = \frac{m_{HA}}{m_{HA} + m_{coll}} = \frac{\rho_{min}}{\rho_{app}} \approx 0.6 \Rightarrow \rho_{app} = \frac{\rho_{min}}{\alpha} \tag{2.12}$$

Using the densities of calcium HA and collagen (ρ_{HA}=3.06 g/cm^3 and $\rho_{coll.}$=1.38 g/cm^3 (Steenbeek et al., 1992)), we can calculate the tissue density of bone:

$$\rho_{coll} = \frac{m_{coll}}{V_{coll}} \Rightarrow V_{coll} = \frac{m_{coll}}{\rho_{coll}} \tag{2.13}$$

$$\rho_{HA} = \frac{m_{HA}}{V_{HA}} \Rightarrow V_{HA} = \frac{m_{HA}}{\rho_{HA}} \tag{2.14}$$

$$\alpha = \frac{m_{HA}}{m_{coll} + m_{HA}} \Rightarrow m_{HA} = \alpha \cdot \left(m_{HA} + m_{coll} \right) \tag{2.15}$$

$$(1-\alpha)=\frac{m_{coll}}{m_{coll}+m_{HA}}\Rightarrow m_{coll}=(1-\alpha)\cdot\left(m_{HA}+m_{coll}\right) \tag{2.16}$$

$$V_{coll}+V_{HA}=\frac{m_{coll}}{\rho_{coll}}+\frac{m_{HA}}{\rho_{HA}}=\frac{m_{coll}+m_{HA}}{\rho_{coll}\cdot\rho_{HA}}\cdot\left[\alpha\cdot\rho_{coll}+(1-\alpha)\cdot\rho_{HA}\right] \tag{2.17}$$

$$\Rightarrow\rho_{tissue}=\frac{m_{HA}+m_{coll}}{V_{HA}+V_{coll}}=\frac{\rho_{coll}\cdot\rho_{HA}}{\alpha\cdot\rho_{coll}+(1-\alpha)\cdot\rho_{HA}}\approx 2.06\ \text{g/cm}^3 \tag{2.18}$$

The estimate of tissue density corresponds with the results of Morgan et al. (2003) who found the trabecular tissue density to be 2.05 g/cm^3. From this we can define the bone volume fraction (BV/TV) of a sample:

$$\frac{BV}{TV}=\frac{\rho_{app}}{\rho_{tissue}}=\frac{\rho_{min}}{\alpha\cdot\rho_{tissue}}=\rho_{min}\cdot\frac{\alpha\cdot\rho_{coll}+(1-\alpha)\cdot\rho_{HA}}{\alpha\cdot\rho_{coll}\cdot\rho_{HA}} \tag{2.19}$$

The bone volume fraction is then used to express the total density of the bone sample as a function of its mineral density (ρ_{min}):

$$\begin{aligned}&\rho_{total}=\rho_{tissue}\cdot\frac{BV}{TV}+\rho_{fluid}\cdot\left(1-\frac{BV}{TV}\right)\\&\Rightarrow\rho_{total}\left(\rho_{min}\right)=\frac{\rho_{min}}{\alpha}+\rho_{fluid}\cdot\left[1-\rho_{min}\cdot\frac{\alpha\cdot\rho_{coll}+(1-\alpha)\cdot\rho_{HA}}{\alpha\cdot\rho_{coll}\cdot\rho_{HA}}\right]\approx 0.857\cdot\rho_{min}+1\end{aligned} \tag{2.20}$$

The bone fluid, or marrow, has been defined to have a density equal to 1.0, and is regarded as a mixture of fat and water. The ratio between the two is the fat fraction (FF), which is known to vary depending on age and gender (Ishijima et al., 1996). Later on, two different compositions of the bone fluid (FF=0 and FF=0.5) will be tested to see what effect it has on the calibration coefficients. The weight fractions of the different constituents of bone can thus be expressed as functions of the bone mineral density (ρ_{min}):

$$\begin{aligned}&w_{fat}=\text{FF}\cdot\rho_{fluid}\cdot\left(1-\frac{BV}{TV}\right)\\&\Rightarrow w_{fat}\left(\rho_{min}\right)=\text{FF}\cdot\rho_{fluid}\cdot\left(1-\rho_{min}\cdot\frac{\alpha\cdot\rho_{coll}+(1-\alpha)\cdot\rho_{HA}}{\alpha\cdot\rho_{coll}\cdot\rho_{HA}}\right)\end{aligned} \tag{2.21}$$

$$\begin{aligned}&w_{water}=(1\text{-FF})\cdot\rho_{fluid}\cdot\left(1-\frac{BV}{TV}\right)\\&\Rightarrow w_{water}\left(\rho_{min}\right)=(1\text{-FF})\cdot\rho_{fluid}\cdot\left(1-\rho_{min}\cdot\frac{\alpha\cdot\rho_{coll}+(1-\alpha)\cdot\rho_{HA}}{\alpha\cdot\rho_{coll}\cdot\rho_{HA}}\right)\end{aligned} \tag{2.22}$$

$$w_{HA}\left(\rho_{min}\right)=\frac{\rho_{min}}{\rho_{total}\left(\rho_{min}\right)} \tag{2.23}$$

$$w_{coll.}\left(\rho_{min}\right)=1-w_{HA}-w_{water}-w_{fat} \tag{2.24}$$

Knowing the chemical composition of water (H_2O) and calcium hydroxyapatite ($Ca_{10}(PO_4)_6(OH)_2$), the elemental weight fractions are calculated using equation (2.7). Fatty acids are long chains of carbon and hydrogen ($[CH_2]_n$). Collagen is made up of different proteins, and we therefore use the elemental weight fraction of protein (Steenbeek et al., 1992): 7% hydrogen, 54% carbon, 16% nitrogen, 23% oxygen.

Table 2.3: Density and elemental weight fractions of the chemical constituents of bone (hydrogen, H; carbon, C; oxygen, O; nitrogen, N; phosphorus, P; calcium, Ca).

	Density	**Elemental weight fractions, %**						Z_T	Z_R
	[g/cm^3]	**H** Z=1, A=1.008	**C** Z=6, A=12.01	**N** Z=7 A=14.01	**O** Z=8, A=16.00	**P** Z=15, A=30.97	**Ca** Z=20, A=40.08		
Water	1.00	11.19	0	0	88.81	0	0	7.52	7.12
Fat	~1.00	14.37	85.63	0	0	0	0	5.54	5.17
Ca. HA	3.06	0.2	0	0	41.4	18.5	39.9	16.32	14.94
Collagen	1.38	7	54	16	23	0	0	6.55	6.24

By combining the weight fractions of water, fat, calcium HA and collagen in equations (2.21) through (2.24) with the weight fractions given in table 2.3, the elemental weight fractions of bone can be expressed as functions of the mineral density:

$$w_H\left(\rho_{min}\right)=0.1119\cdot w_{water}+0.1437\cdot w_{fat}+0.002\cdot w_{HA}+0.07\cdot w_{coll} \tag{2.25}$$

$$w_C\left(\rho_{min}\right)=0.8563\cdot w_{fat}+0.54\cdot w_{coll} \tag{2.26}$$

$$w_N\left(\rho_{min}\right)=0.16\cdot w_{coll} \tag{2.27}$$

$$w_O\left(\rho_{min}\right)=0.8881\cdot w_{water}+0.414\cdot w_{HA}+0.23\cdot w_{coll} \tag{2.28}$$

$$w_N\left(\rho_{min}\right)=0.185\cdot w_{HA} \tag{2.29}$$

$$w_{Ca}\left(\rho_{min}\right)=0.399\cdot w_{HA} \tag{2.30}$$

Figure 2.9 shows the weight fractions in bone as a function of mineral density when assuming a fat fraction of 50% in the bone fluid (FF=0.5).

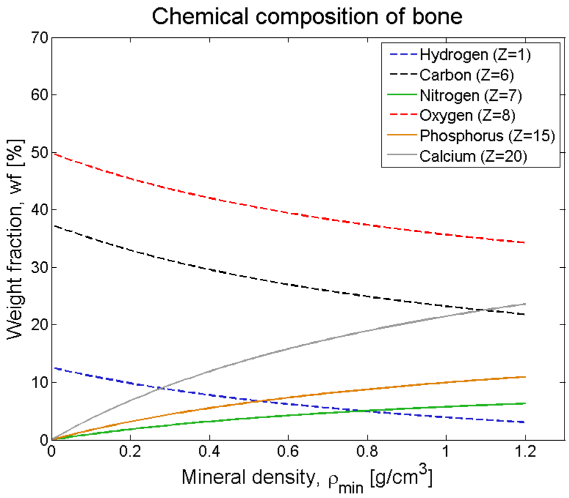

Figure 2.9: Weight fractions of the elemental compounds of bone presented as a function of mineral density (ρ_{min}). The bone fluid was assumed to be 50% fat and 50% water.

The parameters k_1 and k_2, characterising the radiation spectre of the CT scanner, have been determined from the calibration (table 2.2). Thus we can insert k_1 and k_2, the weight fractions (equation (2.25)-(2.30)) and the total bone density (equation (2.20)) into equation (2.4) and (2.1) to calculate HU values for any mineral density. Figure 2.10 shows HU values of bone calculated using the values of k_1 and k_2 from table 2.2.

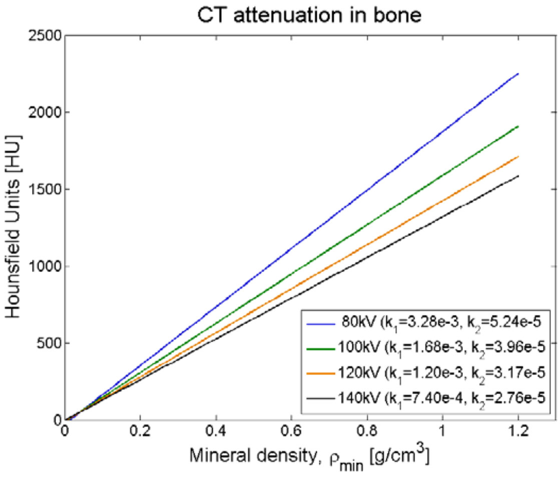

Figure 2.10: HU values calculated for bone tissue at different x-ray tube voltages. The bone fluid was assumed to be 50% fat and 50% water.

The relationship between mineral density and HU values in figure 2.10 can be simplified into a linear function on the form:

$$\rho_{min} = a \cdot HU + b \, [\text{g/cm}^3] \tag{2.31}$$

The slopes (*a*) and y-intercepts (*b*) calculated for the different x-ray tube voltages are shown in table 2.4. The table shows the calibration coefficients when assuming the bone fluid to be an even mixture of water and fat, and when assuming it to only be water:

Table 2.4: Calibration coefficients derived from our procedure.

	kV	***Slope [$a \cdot 10^3$]***	***Y-int. [$b \cdot 10^3$]***
50% water, 50% fat:			
	80	0.522	15.0
	100	0.625	9.5
	120	0.699	6.6
	140	0.756	3.7
100% water, 0% fat:			
	80	0.533	0
	100	0.629	0
	120	0.703	0
	140	0.758	0

The slope increases with increasing x-ray tube voltage, from $0.522 \cdot 10^{-3}$ and $0.533 \cdot 10^{-3}$ at 80 kV to $0.756 \cdot 10^{-3}$ and $0.758 \cdot 10^{-3}$ at 140 kV. A mineral density of 0 g/cm^3 means that the sample only contains fluid. Thus, assuming that the fluid is 100% water, gives a y-intercept of 0 HU as defined in equation (2.1).

In this example, the fat in the bone fluid was assumed to have the same density as water, but a lower effective atomic number due to its carbon content (Z_τ=5.54 versus Z_τ=7.52). This means that a fluid with 50% fat and water will have a lower photon stopping power than pure water, hence the positive y-intercept. As the x-ray tube voltage increases, the amount of photoelectric absorption and Rayleigh scattering is reduced and the atomic number of the material has less effect on the HU values, while material density becomes dominant. Our assumption that the bone fluid has a density equal to water means that fat content in the fluid will affect the calibration coefficients at 80 kV, but be almost negligible at 140 kV. This stands in contrast to other studies who found the error induced by fat to be greater at 130 and 140 kV than at 80 kV (Laval-Jeantet et al., 1986; Goodsitt et al., 1988). Those observations can be explained, if the fat content in marrow and bone fluid gives a significantly lower density than assumed here. The assumption of the bone fluid having a density of 1.0 g/cm^3 was chosen as a compromise between yellow marrow (ρ=0.98 g/cm^3), red marrow (ρ=1.03 g/cm^3) and the fluid extracted from morsellized bone (ρ=1.0 g/cm^3) (Goodsitt et al., 1991; Lunde et al., 2008).

2.5 Evaluation of the calibration procedure

The aim of this chapter was to describe the theory behind the calibration method used in the present thesis. The method is somewhat complicated, but can be used to calculate the HU value of any material with a known density and chemical composition. Unfortunately, we did not have the opportunity to properly validate our calibration coefficients against a standard calibration phantom for bone densitometry. Instead we will evaluate the calibration coefficients used in our subject specific FE models (table 2.5) against those reported in literature (table 2.6). In the CT calibration for our FE models, the bone fluid was assumed to be equivalent to water, which per definition gives a y-intercept of 0.

Table 2.5: Calibration coefficients used in the present thesis (value ± SD). [1]The slope used in the FE models employing equation (2.32). [2]The corrected slope when employing equation (2.18).

	kV	*Slope*[1] [$a \cdot 10^3$]	*Corrected slope*[2] [$a \cdot 10^3$]
Section 3.5			
Callus distraction, Initial	140	0.715	0.773
Callus distraction, Final	140	0.700	0.758
Section 4.3, 4.4 & 4.5			
Femur pair 01	140	0.720	0.778
Femur pair 02	140	0.711	0.772
Femur pair 03	140	0.714	0.773
Femur pair 08	140	0.696	0.755
Femur pair 11	140	0.717	0.774
Femur pair 13	140	0.725	0.789
Femur pair 16	140	0.715	0.773
Femur pair 18	140	0.678	0.734
Femur pair 19	140	0.690	0.748
Mean	140	0.707±0.01	0.766±0.02

The calibration coefficient used to convert HU values to mineral density are shown in table 2.5 to be slightly lower than the ones given for 140 kV in table 2.4. The reason for this discrepancy was an error in the calculation of bone tissue density that was discovered later in the project. Instead of calculating the tissue density as given in equation (2.18), the density was mistakenly calculated as:

$$\rho_{tissue} = \alpha \cdot \rho_{HA} + (1-\alpha) \cdot \rho_{coll.} \approx 2.39\ [\mathrm{g/cm^3}] \tag{2.32}$$

As a result of this mistake, the calibration coefficients used in the FE models are 8% lower than they would have been if equation (2.18) had been employed.

CT calibration coefficients for different calibration phantoms and bone reported in literature are shown in table 2.6. The density derived directly from the calibration phantom is referred to as ρ_{QCT}, while ρ_{min} refers to bone mineral density or ash density.

Table 2.6: Calibration coefficients reported in literature (value ± SD): $\rho_{QCT}=a \cdot HU+b$ and $\rho_{min}=a \cdot HU+b$. Adjusting the calibration coefficients according to: ^{1}Keyak et al. (1994), ^{2}Les et al. (1994), ^{3}Schileo et al. (2008).

		Calibration coefficients, ρ_{QCT}		***Calibration coefficients,*** ρ_{min}	
	kV	$[a \cdot 10^3]$	$[b \cdot 10^3]$	$[a \cdot 10^3]$	$[b \cdot 10^3]$
Liquid phantom, K_2HPO_4:					
Goodsitt et al. (1988)	80	0.538	-27.4		
Keyak et al. (1994)	80	0.529	-1.3	0.498^1	33.5^1
Chen and Lam (1997)	120	0.691	-19.8		
Trabelsi et al. (2009) in air	120	0.663	-18	0.809^2	30.3^2
Trabelsi et al. (2009) in water	120	0.810	-11	0.988^2	38.9^2
Hindelang and Maclean (1997)	130	0.7	-13.6		
Goodsitt et al. (1988)	140	0.787	-6.65		
Keyak et al. (1994)	140	0.673	4.15	0.713^1	43^1
Keyak et al. (1994)	140	0.692	-9.39	0.659^1	30^1
Yosibash et al (2007)	140	0.682	-5.48	0.832^2	45.6^2
Solid phantom, Calcium HA:					
Homolka et al. (2002)	120	0.760±0.03	2.8±3.7		
Homolka et al. (2002)	120	0.804±0.06	5.2±4.2		
Taddei et al. (2006)	120	0.656	15.4		
Taddei et al. (2006)	120	0.644	19.0		
Reggiani et al. (2007)	120	0.808	-5.64		
Schileo et al. (2008)	120	0.776	-5.61	0.681^3	74.02^3
Bone, apparent density:					
Hvid et al. (1989)	100	1.06	94.9	0.610	57.8
Hvid et al. (1989)	120	1.20	101	0.688	61.3
Ciarelli et al. (1991)	130	1.141	118.4		
Hvid et al. (1989)	140	1.30	103	0.746	62.5

The calibration coefficients for ρ_{min} found in bone specimen (Hvid et al., 1989; Ciarelli et al., 1991) show that the slope (*a*) increases with the x-ray tube voltage (kV) similar to our results in table 2.4. Ciarelli et al. (1991) found good correlation between HU values and apparent and mineral density of bone, but only reported calibration coefficients for the apparent density. The positive y-intercepts (*b*) found by Hvid et al. (1989) and Ciarelli et al. (1991) may indicate presence of fatty marrow in the samples (Laval-Jeantet et al., 1986; Goodsitt et al., 1988). Liquid phantoms use K_2HPO_4 dissolved in water, while solid phantoms use calcium HA in water equivalent polymer resin (Kalender et al., 1995; Homolka et al., 2002). Thus, all y-intercepts (*b*) for solid and liquid calibration phantoms listed in table 2.6 should be 0 under ideal circumstances.

The calibration coefficients reported for ρ_{QCT} from the K_2HPO_4 phantom agree very well with our result in table 2.4 and those found for ρ_{min} of bone specimen in table 2.6. Two studies (Yosibash et al., 2007; Trabelsi et al., 2009) adjust ρ_{QCT} according to Les et al. (1994), who found K_2HPO_4 phantoms to underestimate the mineral density of bone considerably. However, judging by the results of Keyak et al. (1994), Hvid et al. (1989) and derived from our method (table 2.4) it seems that the ρ_{QCT} from liquid calibration phantoms hardly needs any adjustment at all. The calibration coefficients reported for the solid calcium HA phantoms show a wide spread of values even at the same x-ray tube voltage. While the values reported by Taddei et al. (2006) are in agreement with our values in table 2.4, the values of *a* reported by the rest are significantly higher. Studies have found calcium HA phantoms to overestimate the mineral density in bone (Kaneko et al., 2003; 2004; Schileo et al., 2008). The adjusted calibration coefficients of Schileo et al. (2008) agree with those reported by Hvid et al. (1989) and our results in table 2.4. Bone tissue consists of a considerable portion collagen (~40%) with a higher density than water (Steenbeek et al., 1992; Hellmich and Ulm, 2002). Collagen will therefore attenuate more radiation than water, which would explain a systematic overestimation of bone mineral density by the calibration phantoms using calcium HA and water equivalent polymer resin. Goodsitt (1992) found that liquid calibration phantoms produced lower estimates of bone mineral content than solid phantoms. This would explain why calibration coefficients from calcium HA phantoms need to be adjusted to relate them to bone mineral density, while calibration coefficients from K_2HPO_4 phantoms do not seem to need any adjustment.

The calibration coefficients presented in table 2.5 and table 2.6 exhibit a wide variation even at the same x-ray tube voltage. A small variation would be expected due to fluctuations in the x-ray spectrum of the CT scanner, but the variation seen for the solid calibration standards still seems excessive. Homolka et al. (2002) reported values for the slope varying between 0.724 (mandible specimen) and 0.868 (patient). A similarly excessive variation in calibration coefficients were reported for the European Spine Phantom at 120 kV; with slopes varying between 0.644 (Taddei et al., 2006) and 0.808 (Reggiani et al., 2007). One explanation for this variation may be that the range of mineral densities in the calibration phantom is not sufficiently wide. The maximum mineral densities in the solid calibration phantoms are 0.15 and 0.20 g/cm^3 in the Dental Phantom and European Spine Phantom (Homolka et al., 2002; Schileo et al., 2008), respectively. Fully mineralized bone on the other hand, has a mineral density of about 1.2 g/cm^3. The extrapolation outside the range of the materials in the calibration phantom, thus make the calibration coefficients much more susceptible to errors due to noise or artefacts in the CT images. In our calibration phantom, the materials span the range of material densities and atomic numbers found in bone, and should therefore provide more stable results. Although the range and standard deviation of the calibration coefficients is less in our phantom, there is still a considerable variation in the calibration coefficients used in our FE models (table 2.5) – with a ranging from $0.678 \cdot 10^{-3}$ to $0.725 \cdot 10^{-3}$ at 140 kV ($0.734 \cdot 10^{-3}$ to $0.789 \cdot 10^{-3}$, corrected coefficients). Some of this variation may be attributed to inaccuracies in the mixing of the phantom materials. Trabelsi et al. (2009) found the calibration coefficients to differ considerably if scanned in air or while immersed in water. The calibration coefficients in table 2.4 and for the callus distractions in (table 2.5) were derived from the phantom scanned in air, while the calibration coefficients for the femurs (table 2.5) while surrounded by water. Our calibration phantom does not seem to be affected by the surrounding medium.

Our method of calibration is clearly much more complicated than the standard procedures, and we even discovered an error in the calculation of bone tissue composition. The error gave a systematic underestimation of bone mineral density of 8% percent. Still, the calibration coefficients used in our FE models are within the range reported for standard calibration procedures at the same x-ray tube voltages. We have therefore chosen not to redo the FE analyses with corrected calibration coefficients. The procedure described in this chapter was used because we did not have any standard calibration phantom available, and therefore had to improvise a phantom. The phantom could be improved by using K_2HPO_4 dissolved in water instead of PMMA and $CaCO_3$ mixtures, as it easier to ensure homogenous material distribution in a liquid solution than in a solid mixture. Aluminium could also be included as it has radiological properties (Z=13, ρ=2.7 g/cm^3) close to that of fully mineralized bone. The main advantage of the presented procedure is that it enables the contribution of collagen to be included in the calibration, something that is disregarded in the standard solid and liquid calibration phantoms.

References

Bessho, M., Ohnishi, I., Matsuyama, J., Matsumoto, T., Imai, K., Nakamura, K., (2006). Prediction of strength and strain of the proximal femur by a CT-based finite element method. J.Biomech.

Boone, J. M., Seibert, J. A., (1997). An accurate method for computer-generating tungsten anode x-ray spectra from 30 to 140 kV. Med.Phys. 24, 1661-1670.

Broz, J. J., Simske, S. J., Greenberg, A. R., (1995). Material and compositional properties of selectively demineralized cortical bone. Journal of Biomechanics 28, 1357-1368.

Carter, D. R., Hayes, W. C., (1977). The compressive behavior of bone as a two-phase porous structure. J.Bone Joint Surg Am. 59, 954-962.

Chen, X., Lam, Y. M., (1997). Technical note: CT determination of the mineral density of dry bone specimens using the dipotassium phosphate phantom. Am.J.Phys.Anthropol. 103, 557-560.

Ciarelli, M. J., Goldstein, S. A., Kuhn, J. L., Cody, D. D., Brown, M. B., (1991). Evaluation of orthogonal mechanical properties and density of human trabecular bone from the major metaphyseal regions with materials testing and computed tomography. J.Orthop.Res. 9, 674-682.

Dance, D. R., (2003). Diagnostic Radiology with X-rays. In: Webb, S. (Ed.), The Physics of Medical Imaging. Institute of Physics Publishing, pp. 20-73.

Goodsitt, M. M., (1992). Conversion relations for quantitative CT bone mineral densities measured with solid and liquid calibration standards. pp. 145-158.

Goodsitt, M. M., Johnson, R. H., Chesnut, C. H., III, (1991). A new set of calibration standards for estimating the fat and mineral content of vertebrae via dual energy QCT. Bone Miner. 13, 217-233.

Goodsitt, M. M., Kilcoyne, R. F., Gutcheck, R. A., Richardson, M. L., Rosenthal, D. I., (1988). Effect of collagen on bone mineral analysis with CT. Radiology 167, 787-791.

Hellmich, C., Ulm, F. J., (2002). Are mineralized tissues open crystal foams reinforced by crosslinked collagen? Some energy arguments. J.Biomech. 35, 1199-1212.

Hernandez, C. J., Beaupre, G. S., Keller, T. S., Carter, D. R., (2001). The influence of bone volume fraction and ash fraction on bone strength and modulus. Bone 29, 74-78.

Hindelang, M., MacLean, A. L., (1997). Bone density determination of moose skeletal remains from Isle Royale National Park using digital image enhancement and quantitative computed tomography (QCT). International Journal of Osteoarchaeology 7, 193-201.

Homolka, P., Beer, A., Birkfellner, W., Nowotny, R., Gahleitner, A., Tschabitscher, M., Bergmann, H., (2002). Bone mineral density measurement with dental quantitative CT prior to dental implant placement in cadaver mandibles: pilot study. Radiology 224, 247-252.

Hubbell, J. H., (1999). Review of photon interaction cross section data in the medical and biological context. Phys.Med.Biol. 44, R1-22.

Hvid, I., Bentzen, S. M., Linde, F., Mosekilde, L., Pongsoipetch, B., (1989). X-ray quantitative computed tomography: the relations to physical properties of proximal tibial trabecular bone specimens. J.Biomech. 22, 837-844.

Ishijima, H., Ishizaka, H., Horikoshi, H., Sakurai, M., (1996). Water fraction of lumbar vertebral bone marrow estimated from chemical shift misregistration on MR imaging: normal variations with age and sex. AJR Am.J.Roentgenol. 167, 355-358.

Kalender, W. A., Felsenberg, D., Genant, H. K., Fischer, M., Dequeker, J., Reeve, J., (1995). The European Spine Phantom--a tool for standardization and quality control in spinal bone mineral measurements by DXA and QCT. Eur.J.Radiol. 20, 83-92.

Kaneko, T. S., Bell, J. S., Pejcic, M. R., Tehranzadeh, J., Keyak, J. H., (2004). Mechanical properties, density and quantitative CT scan data of trabecular bone with and without metastases. pp. 523-530.

Kaneko, T. S., Pejcic, M. R., Tehranzadeh, J., Keyak, J. H., (2003). Relationships between material properties and CT scan data of cortical bone with and without metastatic lesions. Med.Eng Phys. 25, 445-454.

Keller, T. S., (1994). Predicting the Compressive Mechanical-Behavior of Bone. Journal of Biomechanics 27, 1159-1168.

Keyak, J. H., Falkinstein, Y., (2003). Comparison of in situ and in vitro CT scan-based finite element model predictions of proximal femoral fracture load. Med.Eng Phys. 25, 781-787.

Keyak, J. H., Lee, I. Y., Skinner, H. B., (1994). Correlations between orthogonal mechanical properties and density of trabecular bone: use of different densitometric measures. J.Biomed.Mater.Res. 28, 1329-1336.

Keyak, J. H., Rossi, S. A., (2000). Prediction of femoral fracture load using finite element models: an examination of stress- and strain-based failure theories. J.Biomech. 33, 209-214.

Laval-Jeantet, A. M., Roger, B., Bouysee, S., Bergot, C., Mazess, R. B., (1986). Influence of vertebral fat content on quantitative CT density. Radiology 159, 463-466.

Lees, S., (2003). Mineralization of type I collagen. Biophys.J. 85, 204-207.

Les, C. M., Keyak, J. H., Stover, S. M., Taylor, K. T., Kaneps, A. J., (1994). Estimation of material properties in the equine metacarpus with use of quantitative computed tomography. J.Orthop.Res. 12, 822-833.

Lunde, K. B., Sletmoen, M., Stokke, B. T., Skallerud, B., (2008). The fluid phase of morsellized bone: Characterization of viscosity and chemical composition. Journal of the Mechanical Behavior of Biomedical Materials 1, 199-205.

Martin, R. B., Burr, D. B., Sharkey, N. A., (2007). Skeletal Biology. Skeletal Tissue Mechanics. Springer-Verlag, pp. 29-78.

Morgan, E. F., Bayraktar, H. H., Keaveny, T. M., (2003). Trabecular bone modulus-density relationships depend on anatomic site. J.Biomech. 36, 897-904.

Raum, K., Cleveland, R. O., Peyrin, F., Laugier, P., (2006). Derivation of elastic stiffness from site-matched mineral density and acoustic impedance maps. Phys.Med.Biol. 51, 747-758.

Reggiani, B., Cristofolini, L., Varini, E., Viceconti, M., (2007). Predicting the subject-specific primary stability of cementless implants during pre-operative planning: Preliminary validation of subject-specific finite-element models. J.Biomech. 40, 2252-2258.

Rutherford, R. A., Pullan, B. R., Isherwood, I., (1976). Measurement of effective atomic number and electron density using an EMI scanner. Neuroradiology 11, 15-21.

Schileo, E., Dall'ara, E., Taddei, F., Malandrino, A., Schotkamp, T., Baleani, M., Viceconti, M., (2008). An accurate estimation of bone density improves the accuracy of subject-specific finite element models. J.Biomech. 41, 2483-2491.

Schneider, U., Pedroni, E., Lomax, A., (1996). The calibration of CT Hounsfield units for radiotherapy treatment planning. Phys.Med.Biol. 41, 111-124.

Schneider, W., Bortfeld, T., Schlegel, W., (2000). Correlation between CT numbers and tissue parameters needed for Monte Carlo simulations of clinical dose distributions. Phys.Med.Biol. 45, 459-478.

Seibert, J. A., (2004). X-ray imaging physics for nuclear medicine technologists. Part 1: Basic principles of x-ray production. J.Nucl.Med.Technol. 32, 139-147.

Seibert, J. A., Boone, J. M., (2005). X-ray imaging physics for nuclear medicine technologists. Part 2: X-ray interactions and image formation. J.Nucl.Med.Technol. 33, 3-18.

Steenbeek, J. C., van, K. C., Grashuis, J. L., (1992). Influence of calibration materials in single- and dual-energy quantitative CT. Radiology 183, 849-855.

Taddei, F., Martelli, S., Reggiani, B., Cristofolini, L., Viceconti, M., (2006). Finite-element modeling of bones from CT data: sensitivity to geometry and material uncertainties. IEEE Trans.Biomed.Eng 53, 2194-2200.

Trabelsi, N., Yosibash, Z., Milgrom, C., (2009). Validation of subject-specific automated p-FE analysis of the proximal femur. J.Biomech. 42, 234-241.

Watanabe, Y., (1999). Derivation of linear attenuation coefficients from CT numbers for low-energy photons. Phys.Med.Biol. 44, 2201-2211.

Yosibash, Z., Trabelsi, N., Milgrom, C., (2007). Reliable simulations of the human proximal femur by high-order finite element analysis validated by experimental observations. J.Biomech. 40, 3688-3699.

Chapter 3: Subject specific FE analysis of a callus distraction

3.1 Background

Callus distraction, also known as distraction osteogenesis and callotasis, is the procedure of correcting and reconstructing the length of a limb by slowly stretching an osteotomy site. The procedure was pioneered and developed by the Soviet orthopaedic surgeon Gavriil Ilizarov, who observed new bone tissue being formed in the distracted fracture gap of a patient (Ilizarov, 1990). Ilizarov found that by using a system of external ring fixators it was possible to gradually distract the fracture gap and achieve the desired lengthening of the bone. Eventually, the distracted bone would remodel and regain its ideal tubular shape, making it indistinguishable from the original bone.

Previous methods of limb lengthening were associated with many complications and great risk for the patient, and were generally avoided by the surgeons unless amputation was the only other alternative. Grafting of bone is generally not used as blood supply in bone is poor, thereby making successful integration of graft and host bone difficult (Brutscher, 1994). One-stage lengthening of bones by grafting or the use orthopaedic implants may also cause damage to nerves and soft tissue due to the sudden elongation (Cauchoix and Morel, 1978; Herron et al., 1978). A slow lengthening of the bone callus takes longer time, but allows the formation of new bone and lets the soft tissue adapt more gently. Although not being free from complications, the Ilizarov method of limb lengthening is considered safe and is now a standard procedure for limb lengthening worldwide. The procedure may be used to lengthen limbs in patients with bone deformities, congenital or due to illness, or to regenerate bone after cancer surgery or complicated fractures.

Callus distraction is initiated by fracturing the bone and letting it heal for about a week to allow a fracture callus to form before starting the distraction. The callus is then stretched by 1 mm a day until the desired lengthening is achieved (figure 3.1, left). In addition to limb lengthening, callus distraction can be used for bone transport (figure 3.1, right). Bone transport is used after a section of bone has been resected (tumor, complicated fracture etc.) leaving a gap. A second osteotomy is then performed and slowly stretched to bridge the gap. Bone transport maintains the original length of the limb during treatment, thereby reducing the impact of the treatment to soft tissue and keeping the functionality of the limb.

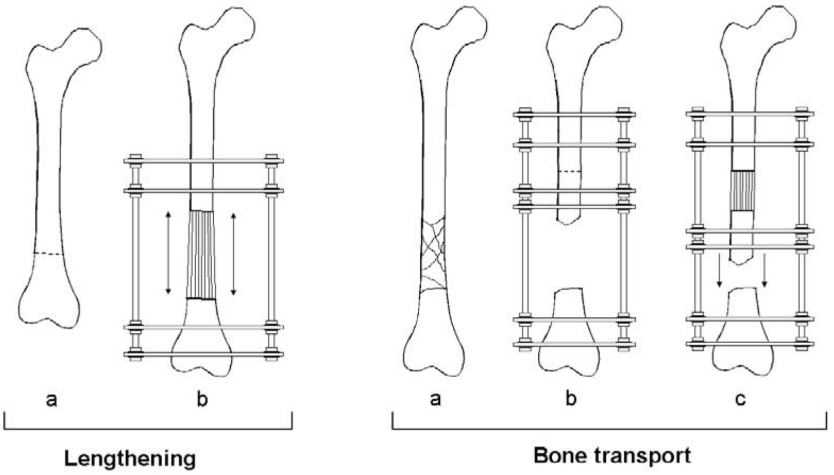

Figure 3.1: Callus distraction used for lengthening a limb (left) and to bridge a bone defect (right).

When the desired lengthening is achieved, the distraction is stopped and the callus tissue is left to consolidate and mineralize. This consolidation process may last two to three times the duration of the distraction process (Brutscher, 1994). Thus, in some cases the external fixation frame must remain in place for as much as a year. The frame cannot be removed until the bone tissue is sufficiently strong and stable to carry the load of the patient. On the other hand, bone tissue needs mechanical stimulus to develop and maintain its strength. Leaving the frame on for too long to be "on the safe side" may therefore be counterproductive as it may lead to bone resorption and delayed healing, in addition to increased risk of pin tract infection. Determining when to remove the external fixation frame is therefore crucial for the success of the treatment.

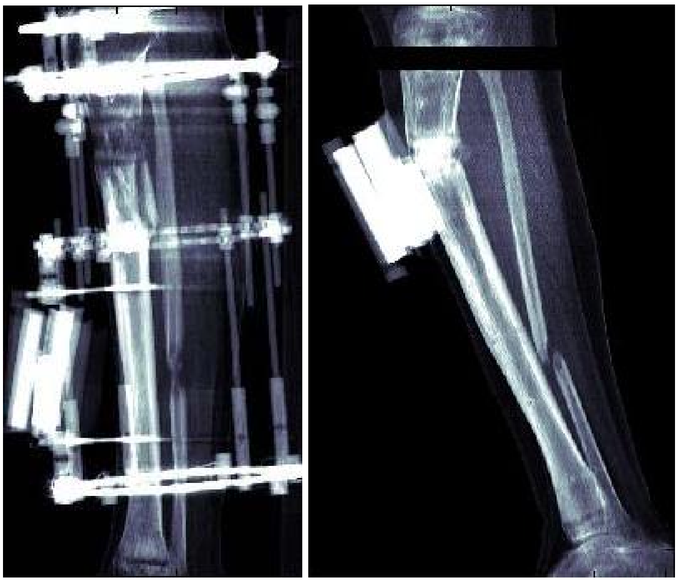

Figure 3.2: Callus distractions in two patients. Left: During the consolidation phase, with the external fixation still in place. Right: The fixation was removed prematurely and the bone regenerate failed after a couple of days.

Plain radiography is usually used to decide when the external frame should be removed. However, it has been found that plain radiography provides poor indication of the mechanical stability of the callus (Blokhuis et al., 2001; Starr et al., 2004; Anand et al., 2006). In figure 3.2 on the right we see an example where the bone regenerate of a leg lengthening had been deemed healed from radiographs, but failed shortly after the fixation was removed.

As will be discussed in this chapter, the callus formed during distraction has a different structure than found in a normal fracture, making it mechanically less stable. Various methods of assessing its stability have been studied: either by direct mechanical measurement on the patient, or indirectly by measuring the mineral content and evaluating the callus structure from radiographic images. In many cases the external fixation frame does not permit measurement of the mechanical stability of the callus. The present chapter will describe how CT images can be used to build subject specific FE models of the distracted section in order to assess its mechanical stability. Only one previous study using subject specific FE models of a callus distraction was found (Harp et al., 1994). The FE model used in that study only had eight elements for each CT scan level, which is too coarse to reflect the heterogeneous structure of the callus distraction. The present chapter will discuss some of the mechanical characteristics of the bone regenerate (section 3.2), the problems with determining its mechanical stability (section 3.3), and how to generate FE models directly from CT scans with only a few manual operations (section 3.4). Such FE models can be used by the orthopaedic surgeon to get an assessment of the stiffness of the lengthened section, and thus be employed to determine when the external fixation can be removed. In section 3.5, the method has been used on a patient. Unfortunately, the external fixation on the patient could not be dismantled to allow direct mechanical testing of the callus distraction. The FE models could therefore not be properly validated. The work presented in section 3.5 is thus only a preliminary study to assess different variables that might influence the results. This is of course a major limitation to the study, but also underlines the main motivation of the study: there is no way to measure the stability of the callus distraction directly, we therefore wish to use subject specific FE models evaluate its stability indirectly.

3.2 Formation of the fracture callus

The trauma of a bone fracture sets off a sequence of biological reactions in cells found in the marrow, on the bone surface and in the bone itself, in order to regenerate the bone and bridge the fracture gap. This section will not go into the biochemistry and cellular reactions, but merely focus on the mechanical aspects of fracture healing and how the healing of a distracted callus differs from a normal fracture.

In general, there are two types of fracture healing: primary and secondary (Phillips, 2005). Primary fracture healing occurs when the fracture is perfectly aligned and stabilized with no relative motion at the fracture interface. It does not produce a fracture callus, instead the osteons in the cortical bone remodel directly across the fracture line thus fusing together the fracture site. Primary fracture healing is usually only seen when internal fixation is used to stabilize the fracture site, and is therefore not relevant for callus distraction. Secondary fracture healing occurs when there is a slight interfragmentary micromotion, and a callus is formed to stabilize and repair the fracture. New bone is formed at the fracture gap by two processes: direct bone formation (intramembranous ossification), and through the formation of cartilage and fibrocartilage that mineralizes over time (endochondral ossification). It has been suggested that the type of tissue that is formed is governed by the stress or strain state at the site (Carter et al., 1998). The cells responsible for generating bone (osteoblasts) need an environment with relatively little strain ($\varepsilon<1\%$) to form woven bone (Wraighte and Scammell, 2006). It has a disorganized structure and inferior mechanical properties compared to mature bone, but it is formed more rapidly. Woven bone created through direct bone formation occurs predominantly on the periosteal surface adjacent to the fracture gap, but can also be found on the endosteum. In areas with strain exceeding the strain limit for bone formation, cartilage and fibrocartilage is generated. As the cartilage stabilizes and reduces the tissue strains at the site, it gradually turns into woven bone. Cartilage is typically formed in and around the fracture gap. A fracture callus usually has a larger diameter than the original bone, which increases its second moment of area and contributes to the structural rigidity of the callus (figure 3.3, left).

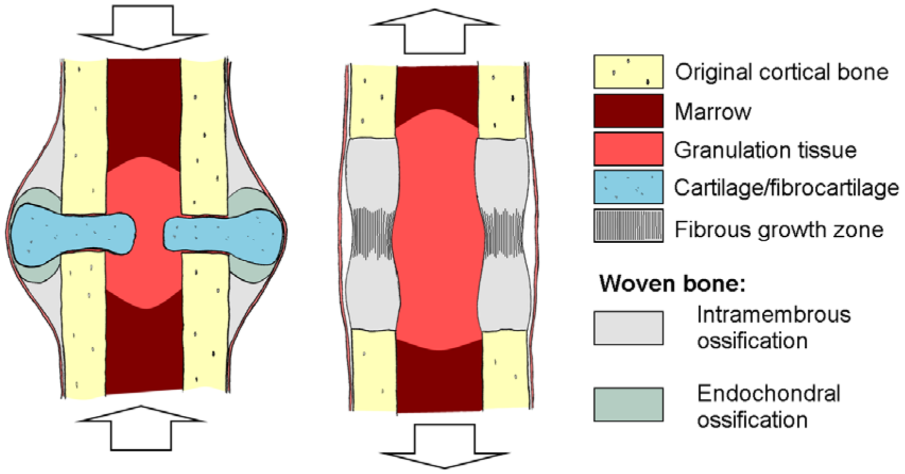

Figure 3.3: The tissue differentiation in fracture healing when subjected to compression (normal fracture healing) and tension (distraction osteogenesis).

Studies have shown that under ideal circumstances the pattern of bone formation in a distracted callus is different from the normal fracture healing (Aronson et al., 1990; Garcia et al., 2008). A fibrous tissue is formed between the two osteotomy surfaces with fiber orientation parallel to the direction of distraction. New bone is formed along these fibers, creating small columns extending from the osteotomy towards the center of the fracture gap (figure 3.3, right). A fibrous growth zone is maintained in the center of the fracture gap during distraction. The new bone generated along the fibers is formed in a process similar to intramembrous ossification without an intermittent cartilage phase (Ilizarov, 1989; Karaharju et al., 1993; Garcia et al., 2008). After distraction has been completed, the fibrous growth zone ossifies and a structure of trabecular bone oriented parallel with the distraction direction is formed in the distraction gap.

Carter et al. (1998) used a simple FE model to demonstrate the two tissue differentiation patterns seen in a normal fracture callus and a callus undergoing distraction. It was assumed that muscle contractions and partial load bearing would subject a regular fracture to compressive forces, while a fracture gap undergoing distraction is subjected to tension. Compression produced a stress/strain pattern indicating a tissue differentiation similar to what is observed in regular fracture healing: direct bone formation on the periosteum, cartilage formation in the medullary cavity, and fibrocartilage in the fracture gap. They also found that bony bridging across the fracture would occur on the periphery of the callus. Under tension, representing the callus distraction, the pattern of tissue differentiation was opposite. Here the FE model predicted direct bone formation in the fracture gap and cartilage formation on the periosteum. FE models incorporating tissue differentiation schemes, have been used to demonstrate the effect of mechanical loading on bone repair and regeneration in normal fracture healing (Isaksson et al., 2006) and callus distraction (Isaksson et al., 2007). Also here the simulations predicted that a compressive load would give an external callus with early bony bridging in the periphery of the callus, while tensile forces gave bone formation in the fracture gap. A fracture undergoing distraction will therefore not get the characteristic bulging callus shape, but more likely a straight or even hourglass shaped callus. This gives it a very unfortunate cross sectional shape, which in combination with its wide fracture gap (~50 mm) makes it considerably less stable than a normal fracture callus.

3.3 Various methods of evaluating the consolidation of a callus distraction

Plain radiography is the main method in orthopaedics for examining fractures. When examining the consolidation of callus distractions, antero-posterior and medio-lateral radiographs are used. The fixation should be removed when the formation of a cortical wall is evident and can be seen in 3 of 4 sides in the two radiographs (Beaty, 1992; Starr et al., 2004; Fischgrund et al., 1994). This is a very subjective and not very reliable criterion (Blokhuis et al., 2001; Starr et al., 2004). Studies have therefore explored the possibilities of using other methods for determining the consolidation of the bone regenerate: ultrasound, quantitative radiography (DEXA, quantitative CT) and mechanical testing.

3.3.1 Imaging techniques

As opposed to radiographic imaging (plain radiography, DEXA, CT etc.) ultrasound does not expose the patient to any harmful radiation. It has even been suggested that ultrasound can help promote and accelerate bone regeneration in fracture healing (Malizos et al., 2006). The method has shown good results for the early phases of distraction when the mineralization of the bone regenerate is low. However, as the mineralization of the bone regenerate increases, ultrasound loses precision and cannot be used to predict the stability and strength during the consolidation phase of the treatment (Bail et al., 2002; Young et al., 1990; Hamdy et al., 1995).

Plain radiography is used by the orthopaedic surgeon to make subjective evaluation of examined body part. The introduction of digital radiography has made it possible to retrieve more reliable quantitative information from the radiographic images. One simple way of calibrating the pixel grayscales in the images to standardized attenuation values, is to include an aluminium step wedge in the images. Kolbeck et al. (1999) found good correlation ($R^2=0.8$) between the torsional stiffness of regenerate bone and equivalent aluminium thickness. Dual energy x-ray absorptiometry (DEXA) utilizes the attenuation values aquired at two different x-ray tube voltages to separate the contribution of attenuation in soft tissue and bone in the image. Thus, DEXA gives an accurate measurement of the amount of bone mineral content within a projection area. It is widely used to monitor osteoporosis, and has also shown good results in assessing the consolidation of leg lengthenings (Eyres et al., 1993a; Eyres et al., 1993b; Reichel et al., 1998; Aronson and Shin, 2003). Tselentakis et al. (2001) found good correlation (R^2=0.77) between bending stiffness and the mineral content across the weakest section of the distracton. The radiation dose from a DEXA examination is lower than from plain radiography (Njeh et al., 1999), which makes it safer for the patient. However, the image resolution of DEXA is considerably poorer than for plain radiography, which makes it difficult to assess the formation of and possible defects in the cortical wall (Eyres et al., 1993a; Aronson and Shin, 2003). In addition, both plain radiography and DEXA are projected images, which means that the structural properties of the bone regenerate are difficult to determine.

CT images can be used to quantify both the mineral density and spatial distribution of the bone tissue. It has therefore been suggested as an alternative method for assessing healing of regular fractures (Augat et al., 1997; den Boer et al., 1998) and limb lengthening (Aronson et al., 1990; Markel and Chao, 1993; Reichel et al., 1998; Aronson and Shin, 2003). The question is how the information provided in the CT images should be analysed. Aronson and Shin (2003) calculated the mean pixel value within a manually drawn region of interest, while Reichel et al. (1998) calculated mean values in the cortical and cancellous zones. Both methods are quite crude and do not take into account how the tissue is distributed over the cross sectional area. Due to the high radiation dose of CT imaging and the lack of a good method of analysing the information in the images, the use of CT for determining callus stability has remained largely academic.

3.3.2 In vivo mechanical testing

Several studies have tried to develop standardised methods for measuring the mechanical stability of fractures and callus distractions on patients. Usually parts of the external fixation must be removed to allow mechanical testing, and thus the feasibility of using this method is limited by the fixation type. Figure 3.4 shows different types of external fixation used for callus distractions.

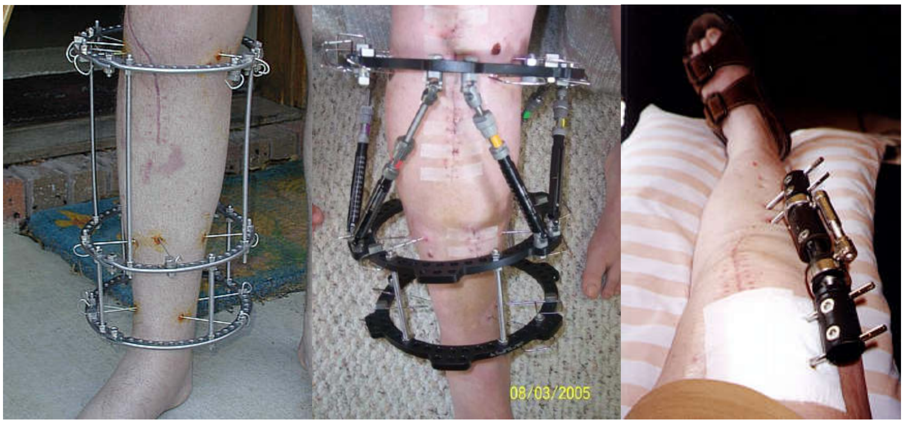

Figure 3.4: Three different fixation systems: From left to right: Ilizarov frame and Taylor spatial frame and the Orthofix unilateral frame.[1]

Unilateral frames are usually preferred when performing mechanical tests, as they are easily removed (Richardson et al., 1994). Dwyer et al. (1996) measured bending stiffness on patients who had undergone leg lengthening with unilateral frames. They proposed that a bending stiffness of 15 and 20 Nm/° for tibia and femur, respectively, could be used as a criterion for when the fixation could be removed. A study by Hammer et al. (1984) arrived at a similar healing criterion of 12.5 Nm/° bending stiffness for tibial fractures. Bending stiffness has shown promising results as an indicator of the maturity of leg lengthenings, and the manufacturer of the Orthofix fixator also supplies measuring equipment to be used with their frame (Orthometer, Orthofix SRL, Verona, Italy). It has therefore been adopted in various studies as an indicator of maturity of a leg lengthenings (Tselentakis et al., 2001; Chotel et al., 2008a; Chotel et al., 2008b). The major limitation with this method is that it requires a unilateral frame. Ring fixators, such as the Ilizarov frame, are easier to customize for each clinical case, and are often preferred for correcting angular deformities in bones.

---

[1] Images were copied from "Ilizarov & External fixator wearers support group" home page: http://www.ilizarov.org.uk/

Another advantage of ring fixators is that the load is more evenly distributed over the osteotomy, which results in a more uniform bone formation in the fracture gap (Aronson et al., 1989). In contrast, unilateral frames have shown to give poor bone formation on the side closest to the frame (Aronson et al., 1989; Hamanishi et al., 1992; Li et al., 2006). Ring fixators are therefore preferred by many orthopaedic surgeons, and bending tests are not feasible on a large portion of the patients.

The Ilizarov frame uses an assembly of halfpins and transosseus wires, which makes temporary dismantling and direct mechanical testing of the lengthened section very difficult. Windhagen et al. (1999) presented a metering device using a sliding halfring system in the frame in order to measure the torsional stiffness of fractures and callus distractions without dismantling the frame. The method has been used in animal studies, and has shown that torsional stiffness is a good predictor of the strength of distracted sections (Windhagen et al., 2000; Floerkemeier et al., 2005). However, the method has not been tested clinically on human patients and no healing criterion based on torsional stiffness has yet been proposed. A more indirect way of measuring the healing of a leg lengthening is to measure the load share ratio of the frame during axial compression (Aarnes et al., 2005; Aarnes et al., 2006). By measuring the forces going through the axial fixator rods, one can assess the load carrying capability of the bone regenerate. Aarnes et al. (2005) proposed that it was safe to remove the frame once the load share ratio of the frame dropped to 10%. This method can be used on patients wearing the Ilizarov ring fixator, but may produce misleading results. The load share ratio depends on the stiffness of the frame, which will vary depending on frame design and tension in the transosseus wires (Fleming et al., 1989). If the frame is very rigid, the load share ratio may not reveal if the lengthened section is fully consolidated. Also, axial testing will not be able to differentiate between an ideal tubular shape and a very undesirable hourglass shape as long as the cross sectional area is the same. Bending and torsional stiffness depend on the cross sectional structure (2. moment of area and polar 2. moment of area) and therefore give a much better indication of the stability of the lengthened section. Ideally, a mechanical test procedure should include several load cases in order to determine if it is safe to remove the frame. The different measuring methods of mechanical testing of callus distractions are shown in figure 3.5.

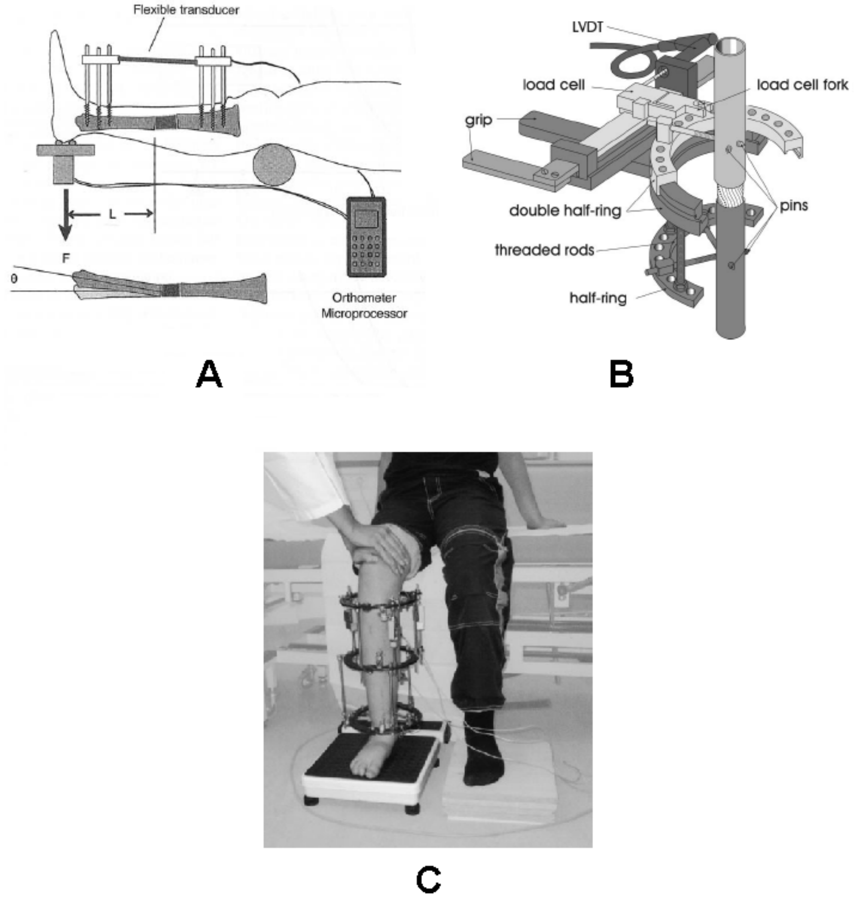

Figure 3.5: Three different methods of measuring the stability of the bone regenerate presented in literature: bending stiffness on a tibia with a unilateral frame (A) (reproduced from Dwyer et al. (1996)), torsional stiffness using a frame with sliding halfrings (B) (reproduced from Windhagen et al. (1999), and load share ratio under axial compression with an Ilizarov frame (reproduced from Aarnes et al. (2006)).

A variation of the ring fixator is the Taylor spatial frame which uses telescopic diagonal rods instead of threaded axial rods. As opposed to the axial rods of the traditional Ilizarov frame, the diagonal rods of the Taylor frame can be disconnected, making it possible to perform direct measurement of mechanical stability. However, we are not aware of any studies exploiting the possibilities with the Taylor frame to perform multiaxial mechanical testing of the bone regenerate.

3.4 Creating the FE model of a callus distraction

3.4.1 Retrieving the geometry of the bone regenerate

As explained in the previous section, the traditional imaging techniques used by orthopaedic surgeons today only have limited capability at predicting the stability of a callus distraction. Images from CT contain information about the tissue mineralization and its distribution over the cross sectional area. The challenge for the orthopaedic surgeon is how the information provided by the CT images should be analysed. Our suggestion is to use the CT images to build a subject specific FE model of the callus, and analyse its total stiffness when subjected to bending, torsion and compression. Thus, the degree of tissue mineralization is put in context of its spatial distribution, and presented in terms of the mechanical properties of the distracted section. Since the FE models are intended to be used by orthopaedic surgeons, the generation of the model, the analyses, and post-processing of the results need to be as automated as possible. Voxel elements will therefore be used in the FE models, as they can be generated directly from the CT pixels. In order to capture the heterogeneous structure of the bone regenerate, CT scans with pixel size less than 0.5 mm and a slice distance of 0.7 mm were used to generate the FE models that will be presented in section 3.5. A program was written in MATLAB 7.0 to generate the voxel FE models directly from the CT scans, submit the models to the FE solver (ABAQUS 6.7, Simulia, Providence, USA) and post-process the results. All actions by the user are performed through a graphic user interface (GUI).

The steps for creating the FE model will now be presented. Figure 3.6 shows the main GUI of the program; the upper part is for generating the FE model, and the lower part for running the FE analysis and post-processing the results. The user assigns a name to the case to be evaluated, browses to find the folder containing the CT scan series of the patient, and selects the desired mesh refinement. With the "fine" mesh refinement, every CT pixel is converted into one voxel element. The "medium" model is created by reducing the CT image resolution from 512 by 512 to 256 by 256, thus doubling the pixel size and reducing the number of elements to a fourth. For the "coarse" model, every two images are merged together in addition to reducing the image resolution, thus doubling both pixel size and image thickness.

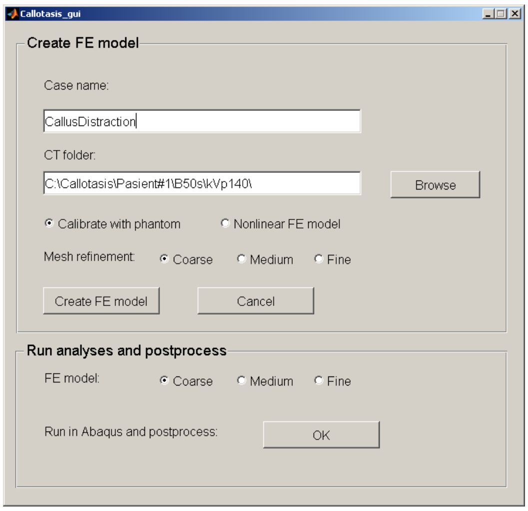

Callotasis_gui

Create FE model

Case name: CallusDistraction

CT folder: C:\Callotasis\Pasient#1\B50s\kVp140\

● Calibrate with phantom ○ Nonlinear FE model

Mesh refinement: ● Coarse ○ Medium ○ Fine

Run analyses and postprocess

FE model: ● Coarse ○ Medium ○ Fine

Run in Abaqus and postprocess:

Figure 3.6: The main GUI of the program. The users enter the path of the CT images and the desired mesh refinement.

The program gathers all the CT images in the selected folder to create antero-posterior and lateral projected images of the scanned limb (figure 3.7, left and center). The user then marks the section he wants to model, by clicking directly in the two images.

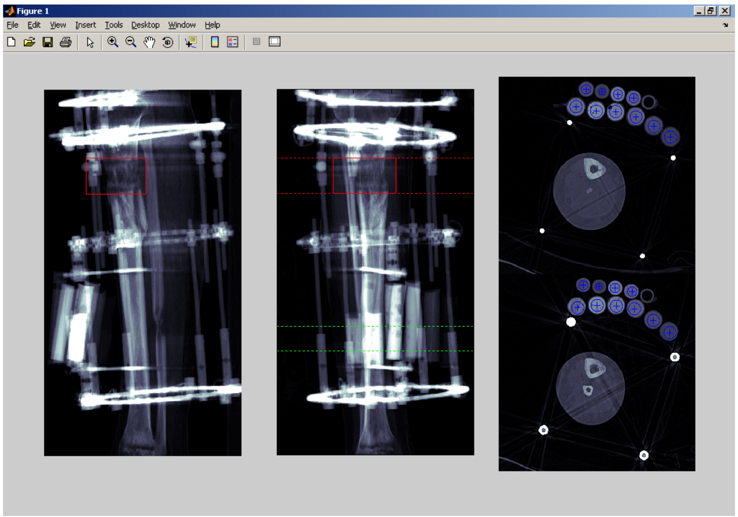

Figure 3.7: The operator selects the sections to be modelled in the two projection images (red box). The center image also shows the top and bottom sections of the calibration phantom selected by the operator. The position of each phantom compartment is marked by the operator (blue circles).

The bone regenerate has a speckled appearance in the CT images with no clearly defined cortex. It is therefore difficult to use automated segmentation techniques to isolate the bone regenerate in the images. Instead, the operator has to define the regions of interest (ROI) in five images from the selected section; top and bottom, center and the two quartiles. The operator draws a closed spline curve around the bone regenerate in each of the five images to define the boundary of the ROI. Once the operator has drawn the ROIs, the program generates the FE model automatically. The program partitions each of the five splines into four quadrants defined by "north-south" and "east-west" from the center of the ROIs, and each segment is again divided into 250 equally spaced points. Thus, every point on the manually defined ROI spline has a corresponding point on each of the other four. Using these sets of corresponding points, the program can automatically calculate a ROI boundary of any CT image in the selected section by interpolation. Figure 3.8 shows the 5 manually defined ROIs (yellow) with interconnecting lines (black) used to calculate the boundaries of the ROIs in all the CT images inbetween (red). The piece-wise cubic hermite interpolation (pchip) scheme in MATLAB 7.1 was used to calculate the interconnecting lines.

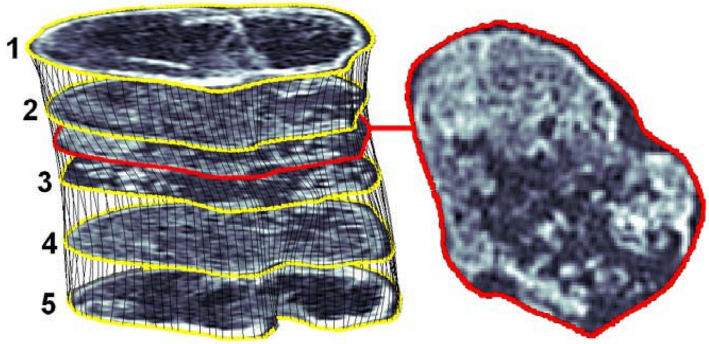

Figure 3.8: ROIs are defined by the user in 5 CT scans (yellow). The ROIs are divided into an equal set of points which are used to link them together. The interconnecting lines (black) are used to automatically generate ROIs in all CT images of the bone regenerate. An automatically generated ROI is seen in red.

The CT pixels inside the ROIs were used to build the FE model, using 8-noded brick elements (element type C3D8). Every element was assigned a Young's modulus according to the HU value of the pixels. As shown in figure 3.8, some areas inside the ROIs contain nonmineralized soft tissue and marrow, which does not contribute to the stability of the distracted section. Therefore a lower threshold of ρ_{min}=0.05 g/cm^3 was defined in the FE models. All elements below this threshold were considered mechanically inactive and assigned a Young's modulus equal to 1% of the modulus for the threshold value. Figure 3.9 shows the finished FE models generated by the program. The model consists of the distracted callus section where the voxel elements reflect the material heterogeneity of the bone regenerate. The bottom nodes are constrained. On top of the callus section, the program adds a layer rigid of elements (E = 900 GPa). The top of the rigid element layer is connected to a beam element (element type B31) using connector elements (element type CONN3D2, *beam*). Thus, loads can be applied to the top node of the beam and the rigid element layer ensures that displacements are evenly distributed over the top of the bone regenerate. The axial direction of the beam goes through the centroids of the first and last ROI, so that it aligns with the axial direction of the leg. Since beam elements have six nodal degrees of freedom (3 translations and 3 rotations) loads can be applied to the model via the top node either on the form of forces and moments, or as displacements and rotations.

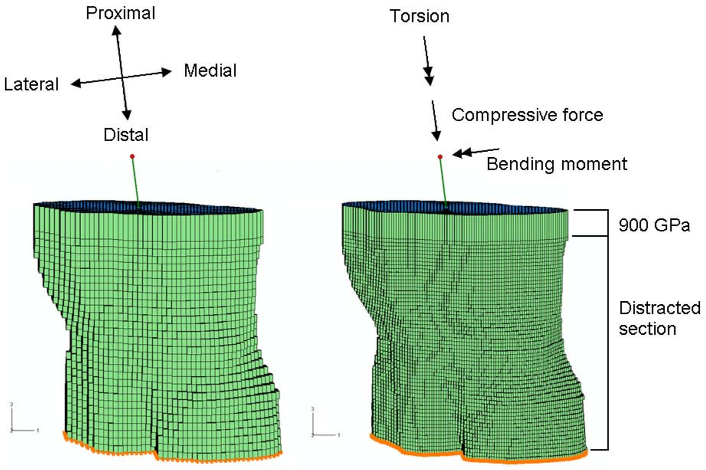

Figure 3.9: FE models bone regenerate with coarse (left) and fine (right) mesh refinement. A layer of rigid elements (900 GPa) is used to ensure that diplacements are evenly distributed on the top of the FE model.

The operator submits the FE model for analysis, by pressing the button marked "Run in Abaqus and postprocess" in the main GUI (figure 3.6). In order to evaluate the stability of the bone regenerate, four load cases are analysed; axial compression, torsion, and bending about the mediolateral and anteroposterior axis. The results are automatically post-processed and presented as force per displacement (kN/mm) and moment per degree deflection (Nm/°). The program does not require any prior knowledge of the FE method, and only a few manual operations are needed to build the models.

3.4.2 Element size and material considerations for modelling bone regenerate

The limited availability of bone regenerate and the heterogeneity of the tissue make it very difficult establish a relationship between its Young's modulus and density. Indentation studies on callus tissue have shown that the stiffness of the tissue depend both on mineral content and maturity of the tissue (Aro et al., 1989; Markel et al., 1990; Leong and Morgan, 2008), with stiffnesses ranging from < 1 MPa in granulation tissue to ~1 GPa for woven bone (Leong and Morgan, 2008). The Young's modulus (E) of bone is usually expressed as a power function of the amount of bone material in the test specimen - bone volume fraction (BV/TV), apparent or mineral density (ρ_{app}, ρ_{min}):

$$E = E_{tissue} \cdot \left(BV/TV\right)^{A} = \left(\frac{E_{tissue}}{\rho_{tissue}^{A}}\right) \cdot \rho_{app}^{A} = \left[\frac{E_{tissue}}{\left(\alpha \cdot \rho_{tissue}\right)^{A}}\right] \cdot \rho_{min}^{A}, \qquad (3.1)$$

where E_{tissue} and ρ_{tissue} is the Young's modulus and density of the trabecular bone tissue, and α is the ash fraction (~0.6). The exponential A is assumed to indicate the type of cellular structure in a porous material, where exponentials of 1, 2 and 3 are associated with columnar, open and closed cell porous structures, respectively (Gibson, 1985). To satisfy a continuum assumption for cancellous bone, the element sides should span at least 5 trabeculae (Harrigan et al., 1988). In cancellous bone the trabecular thickness and spacing is approximately 0.15 mm and 0.5 mm, which means that element sides should be approximately 3 mm. Figure 3.10 shows the midsection of the bone regenerate, the least mineralized level, at two instances during consolidation compared to cancellous regions in the femur. Whereas the cancellous bone in the femur seems to be relatively smoothly distributed over the whole cross section, the bone regenerate more resembles islands of mineralized tissue. Due to the non-uniform distribution of the bone regenerate, it is not possible to increase the element size in order to accommodate a continuum assumption for a porous structure. Instead the elements must be small enough to capture the heterogeneous character of the bone regenerate. The bone density measure (BV/TV, ρ_{app} and ρ_{min}) is then a measure of the local tissue maturity or degree of mineralization, rather than the amount of bone in a porous structure. As most density-stiffness relationships for bone are given as power relations, it seems reasonable to assume the same for bone regenerate as a starting point. The relationship between the density and Young's modulus of the bone regenerate tissue would probably have to be established through in vivo mechanical testing on patients combined with a FE back-calculation scheme. The material properties would thus be derived by adjusting the Young's modulus of trabecular bone (E_{tissue}) and the exponential A in equation (3.1), until the results of the FE analyses corresponded with the experimental measurements. The Young's modulus of trabecular bone has been measured to be between 5 GPa (Choi et al., 1990) and 15 GPa (Rho et al., 1993).

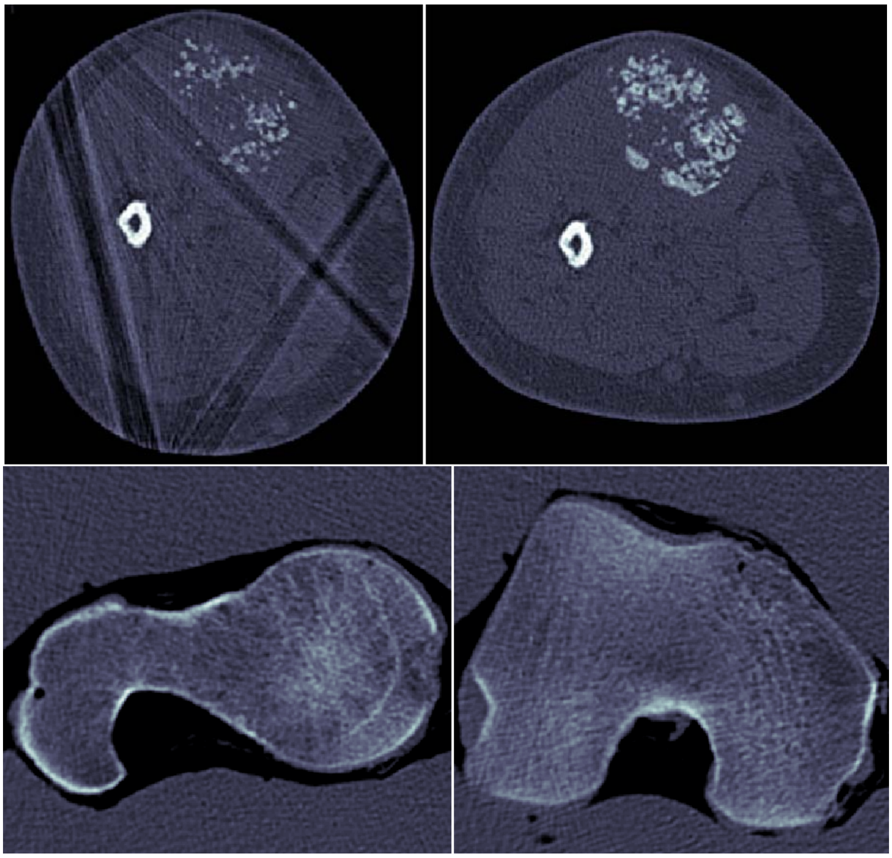

Figure 3.10: Comparison of bone regenerate and mature cancellous bone. The images above show the mid-section of the bone regenerate in a patient at 2 months prior to frame removal (left) and directly after frame removal (right). The images below show the cancellous regions in the proximal femur and femoral condyles of a cadaver bone (Pa01Right). The images are shown with the same gray-scale contrast and reconstruction filter (B50f).

In section 3.5, two different power relationships between density and Young's modulus for bone were tested. Harp et al. (1994) employed the cubic relation of Carter and Hayes (1977) in a previous study of a leg lengthening, but adjusted it by a factor of 0.53. Thus, the relation of Harp et al. (1994) corresponds to a trabecular Young's modulus of 16 GPa when assuming a bone tissue density of 2 g/cm^3. Homminga et al. (Homminga et al., 2001) used an exponential of 1.5 and assumed a trabecular Young's modulus of 5 GPa.

3.5 Subject specific finite element analysis of a callus distraction - a preliminary study[2]

Abstract

Background: Determining the stability of a callus distraction is today largely based on measurement of bone density and qualitative evaluation of bone structure on plain radiographs. In the present study, we demonstrate how computed tomography (CT) and finite element (FE) models can be used together in a simple and effective manner to evaluate the healing of a leg lengthening.

Method of Approach: CT scanning of a callotasis was performed two months before removal of external fixation and directly after removal of fixation. Two sections were modelled at each instance: the callotasis and a reference section below the distraction gap. Two density-stiffness relationships and two mesh refinements were analysed.

Results: The FE analyses showed the estimates of compressive, torsional and bending stiffness to be very sensitive to the power term in the density-stiffness relationship. The stiffness of the callotasis increased from 3% to 19% and 15% to 44% relative to the reference section for a power of 3 and 1.5, respectively. The reference section also showed significant decrease in stiffness; 26% and 15% for a power of 3 and 1.5, respectively. Coarsening the mesh had little effect on the results, but improved computation time considerably.

Conclusions: The study demonstrates the concept of using subject specific FE models to assess the stability of a callotasis. The models are simple to build, requiring only a few manual operations. The method could be used to get a more objective assessment of callotasis healing.

3.5.1 Introduction

The lengthening of bones through callus distraction (callotasis) is a normal procedure to correct the length of limbs (Ilizarov, 1990; Ilizarov and Ledyaev, 1992). The procedure involves first an osteotomy of the bone, and secondly a slow distraction of the callus

---

[2] Pettersen,S.H.,Aamodt,A.,Foss,O.A.,Skallerud,B.(2009) Subject specific finite element analysis of a callus distraction - a preliminary study, in Skallerud,B. and Anderrson,H.(editors) MekIT'09, 26-27th May 2009, Trondheim. Tapir forlag, ISBN:978-82-519-2421-4.

tissue generated in the osteotomy gap. The callus is stretched by means of an external fixation frame approximately 1 mm per day until the right lengthening is achieved - usually 4-5 cm. After the distraction phase, the bone tissue needs time to heal and consolidate. This consolidation phase is the longest phase of the treatment, lasting about two or three times the duration of the distraction (Brutscher, 1994). The frame should not be removed until the callus is strong enough to carry sufficient load. Apart from the general discomfort of the frame, leaving it on for too long may lead to bone loss in the immobilised bone (Eyres et al., 1993b) and increased risk of pin tract infection (Paley, 1990). Determining the correct time to remove the external fixation is therefore critical for the success of the treatment.

Even though plain radiography has shown poor reliability in predicting the healing of bone (Blokhuis et al., 2001; Starr et al., 2004; Anand et al., 2006; Donnan et al., 2002), it remains the most common method of assessing the consolidation process of the callus. When cortical bone can be seen on 3 of 4 sides of the callus distraction in the x-ray images, it is usually regarded as mature and the frame can be removed (Starr et al., 2004). This is a very subjective criterion which leaves a lot to the judgement of the orthopaedic surgeon. Various studies have used mechanical testing to determine callus stiffness in compression (Prat et al., 1994; Aarnes et al., 2005), bending (Richardson et al., 1994; Dwyer et al., 1996; Moorcroft et al., 2001) and torsion (Thorey et al., 2000). However, the external frame makes reliable measurements very difficult, and mechanical measurement of callotases is therefore not very widespread clinically.

Finite element (FE) models based on quantitative computed tomography (CT) are widely used in biomechanics and have been used to assess healing of regular fractures (Shefelbine et al., 2005) and callus distractions (Harp et al., 1994). It has been shown that quantitative CT coupled with FE analysis provides a higher degree of accuracy in predicting the femoral and vertebral strength than DEXA and quantitative CT alone (Cody et al., 1999; Crawford et al., 2003). Various studies have used FE models to explain the mechanobiology of callus distraction (Carter et al., 1998; Boccaccio et al., 2007; Isaksson et al., 2007), however the authors are not aware of any studies using the FE models as a clinical tool to evaluate the consolidation process in patients. Only one study was found using CT scans to create a subject specific FE model of a leg lengthening (Harp et al., 1994).

By converting the pixel data of the CT scans into voxel elements, subject specific FE models can be generated quickly and with a minimum of manual labour (Keyak et al., 1990). CT scans of a lengthened leg were obtained during consolidation and at removal of the external frame, and used to build the FE models. The FE models were analysed under different simplified load cases; axial compression, bending and torsion. A section below the distraction gap was also analysed and used as a reference to assess the consolidation of the callus distraction.

We do not have any mechanical stiffness measurement on the lengthened leg, and therefore cannot provide a full validation of our FE models. Instead, we will look at how the choice of material models and element size will affect results and computation time. Two different material models were investigated; one that has been used earlier in a FE study of a leg lengthening (Harp et al., 1994), and a material model for vertebral cancellous bone used for elements sizes of the same magnitude as the trabecular thickness (Homminga et al., 2001).

3.5.2 Material and Methods

CT scans of one male patient (31 years, 95 kg), who was treated with tibial lengthening, were used in the study. CT scans were obtained during the consolidation phase 4 1/2 months after end of distraction with the Ilizarov frame still in place, and 2 months later directly after removal of the frame. We will denote these two instances as the initial and final state, respectively. A multislice CT scanner (Siemens Somatom Sensation 64, Erlangen, Germany) was used at 140 kV, 0.7 mm slice interval and B50s convolution kernel. The pixel size was 0.445 mm and 0.375 mm for the initial and the final scan series, respectively. The CT scans were calibrated using the method described by Schneider et al. (2000) using phantoms consisting of different mixtures of PMMA and calcium carbonate, and the CT attenuation values (HU) converted into mineral densities[3]. The linear conversion factor between mineral density (g/cm^3) and HU values (ρ_{min}/HU) was found to be $7.15 \cdot 10^{-4}$ and $7.00 \cdot 10^{-4}$ for the initial and final scan series, respectively. The apparent density was calculated from the mineral density by assuming a constant ratio $\rho_{min.}/\rho_{app.}$ of 0.6 (Schileo et al., 2007).

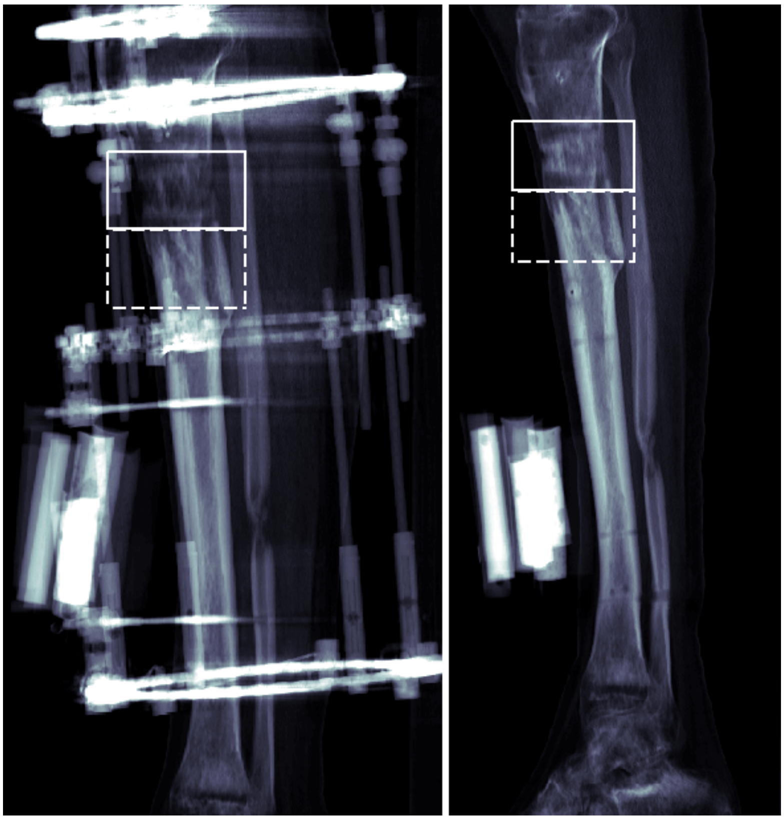

Figure 3.11: The lengthened leg at the initial (left) and final state (right). The boxes show the sections selected for the voxel FE models of the callus distraction (solid lines) and the reference section (dashed lines).

The voxel FE models were generated from the CT images using scripts in MATLAB 7.1 (The Mathworks, Natick, USA) and imported into a commercially available FE program (ABAQUS 6.7, Simulia, Providence, USA). For each of the two time instances, two sections were selected: the callus distraction and a reference section below the distraction gap (figure 3.11). All sections had the same length (L = 40.6 mm).

---

[3] See *Chapter 2: Relating CT gray-scale values to bone density.*

Metal artifacts from the Ilizarov frame and the absence of a clearly defined cortical wall in the distracted section made it difficult to use automated segmentation to define a region of interest (ROI) in the CT images. Instead, a closed spline curve defining the ROI was drawn manually in five CT images: the top, middle, bottom and quartiles in a subset of CT images for each modelled section. Each spline curve was automatically divided into an equal set of points and direction and starting point of the curves adjusted to coincide with the others. In our model the number of points was set to 1000 to get the points densely distributed along the curves. Thus, by interpolating a set of 1000 lines between the 5 manually drawn ROI curves (figure 3.12) can be calculated. These lines are in turn used to automatically generate ROIs for all CT images of the selected subset. In our program a piecewise cubic hermite interpolation procedure was used. Only the pixels inside the ROI in each CT image were used in the FE models.

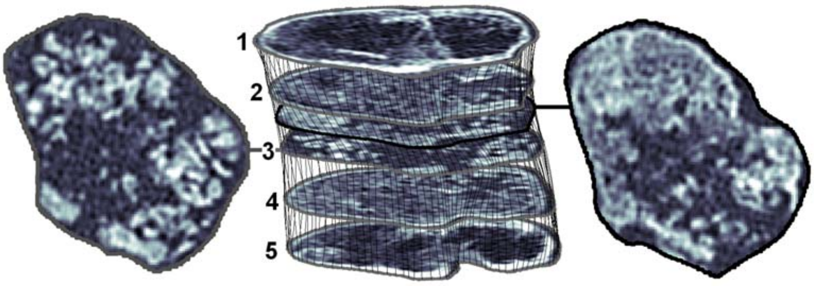

Figure 3.12: The ROIs on the top (1), middle (3), bottom (5) and quartiles (2 and 4) of the modelled section are drawn manually. These ROIs are divided into an equal number of points which are used to automatically generate ROIs for all CT images inbetween. A manually drawn ROI is seen on the left and an automatically generated ROI on the right.

The FE models were comprised of 8-noded linear brick elements (element type *C3D8*). Two mesh refinements were generated: a fine and a coarse (figure 3.13). In the fine mesh, one element was generated for each pixel. To generate the coarse mesh, the resolution of the CT images was reduced from 512x512 to 256x256 pixels and every two images merged together, thus doubling the pixel size and slice distance and reducing the number of elements to an eighth of the fine mesh.

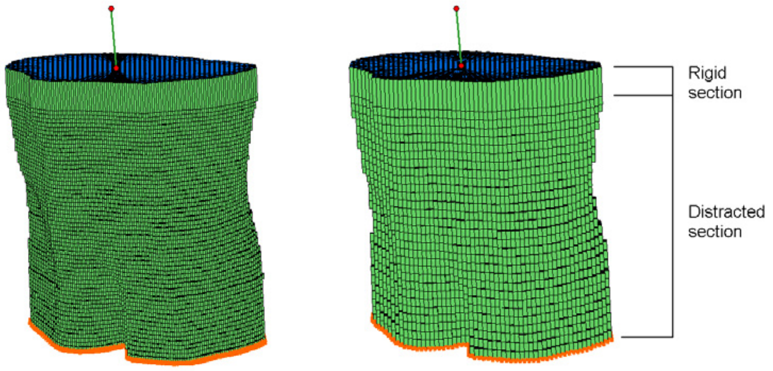

Figure 3.13: Fine (left) and coarse (right) FE model of the callus distraction at the final state. Loads were applied to the top node of the beam element, while the bottom nodes (orange) were fully constrained.

The bottom nodes were modelled as fully constrained. On the top, a 5 mm layer of very stiff elements was generated (E = 900 GPa, ν = 0.3). An axial beam element (element type *B31*) was connected to the top layer by connector elements (element type *CONN3D2, beam*). The axial direction of the beam was calculated from the center of the top and bottom ROIs. The axial beam could thus be used for applying forces and moments to the model while the rigid top layer ensured an even displacement on the top of the voxel mesh.

Four different load cases were simulated: compression, torsion and bending about the medio-lateral and antero-posterior direction. For compression and torsion, only axial translation and rotation was allowed for the axial beam element. The beam was constrained in the medio-lateral direction for bending about the medio-lateral axis and vice versa for bending about the antero-posterior axis.

Each voxel element was assigned a Young's modulus according to its density. As there is no established relationship between the density (or degree of tissue mineralization) and Young's modulus for bone regenerate, two density-stiffness relationships for cancellous bone were considered in the FE models:
Carter and Hayes (1977):

$$E = 3790 \cdot \rho_{app}^{3} \dot{\varepsilon}^{0.06} = 2009 \cdot \rho_{app}^{3} \text{ [MPa]} \tag{3.2}$$

Homminga et al. (2001):

$$E = E_{tissue} \cdot GV^{1.5} = \frac{5000}{1.20^{1.5}} \cdot \rho_{min}^{1.5} \text{ [MPa]} \tag{3.3}$$

Carter and Hayes (1977) assumed the trabecular Young’s modulus to be 22 GPa for a density of 1.8 g/cm^3. When setting the viscoelastic term ($\dot{\varepsilon}^{0.06}$) equal to 0.53 (Harp et al., 1994) and assuming a trabecular density of 2.0 g/cm^3 (Morgan et al., 2003), equation (3.2) corresponds to a trabecular Young’s modulus of 16 GPa. Equation (3.3) assumes the trabecular Young’s modulus to be 5 GPa for a trabecular density of 2.0 g/cm^3 ($\rho_{\min}$=1.20 g/cm^3). Equation (3.2) and (3.3) thus respectively represent the higher and lower estimates of trabecular Young’s modulus; 5 GPa (Choi et al., 1990) and 15 GPa (Rho et al., 1993). Similarly, the power terms of 3 and 1.5 are representative for what is found in literature, when expressing the density-stiffness relationship as a power function. For an idealized porous structure a linear function represents axially aligned columns, a quadratic function an open cell architecture, and a cubic function a closed cell architecture (Gibson, 1985). It is thus likely to believe that the density-stiffness relationship of bone regenerate can be found somewhere between equation (3.2) and (3.3).

A lower threshold of ρ_{min}=0.05 g/cm^3 was chosen for our FE models. Elements below this threshold were considered mechanically inactive and assigned a Young's modulus 1% of the Young's modulus calculated for the threshold density.

The displacements of the beam nodes were used to calculate the axial (kN/mm), bending (Nm/°) and torsional stiffness (Nm/°) of the modelled bone section. Since no material nonlinearity was considered in the FE models, the analyses were run in ABAQUS 6.7 as a linear perturbation step.

3.5.3 Results

The coarse FE models were run on a regular PC. The coarse model with most degrees of freedom (D.O.F.) required less than 1 Gb memory and 7 minutes to complete. The fine FE models were run on a high performance computer using 16 CPU's and required approximately 15 Gb of memory and 50 minutes to complete for the model with the most D.O.F.

Bone mineral content and average mineral densities of the FE models were calculated by excluding the mechanically inactive elements (ρ_{min}<0.05 g/cm^3). Bone mineral content in the callus distraction increased by 44% from initial to final state, with average mineral density increasing from 0.21 g/cm^3 (290HU) to 0.27 g/cm^3 (382HU). In the same time period bone mineral content in the reference section decreased by 10%, with average mineral densities decreasing from 0.47 g/cm^3 (660HU) to 0.44 g/cm^3 (624HU). The distributions of element densities in the different modelled sections are shown in figure 3.14.

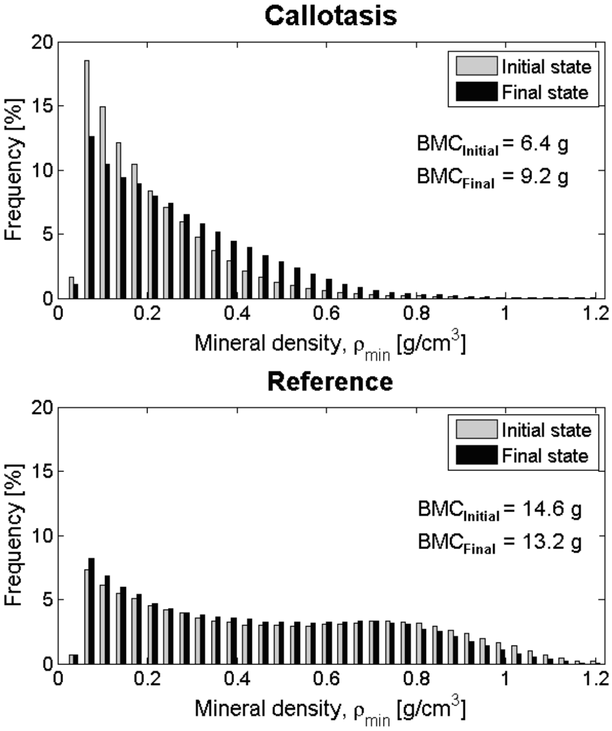

Figure 3.14: Mineral content and distribution of voxel mineral densities (fine mesh) for the callus distraction (callotasis) and reference sections. Voxels below the threshold level (ρ_{min}<0.05 g/cm3) have been excluded.

The stiffness measures calculated using the density-stiffness relationship of equation (3.2) gave an average initial stiffness of 3% for the callus distraction relative to the reference section (table 3.1). At the final state, the stiffness measures had risen to an average of 19%. For equation (3.3) the stiffnesses were approximately 15% at the initial state and increase to 44% at the final state (table 3.2).

The results also show a distinct decrease in calculated stiffness for the reference section between the initial and the final state: 26% and 15% for equation (3.2) and (3.3), respectively. Little difference was seen between the stiffness measures calculated for the coarse and the fine FE models.

Table 3.1: Stiffness measures of the FE model using equation (3.2).

	D.O.F.	Compression [kN/mm]	Bending ML [Nm/°]	Bending AP [Nm/°]	Torsion [Nm/°]
Initial:					
Callotasis, fine	1,076,955	0.82	1.38	1.57	0.45
Callotasis, coarse	147,915	0.81	1.45	1.50	0.50
Reference, fine	967,512	27.79	65.69	46.14	22.95
Reference, coarse	136,371	26.34	61.19	44.05	22.20
Final:					
Callotasis, fine	1,528,068	3.49	7.68	6.79	3.69
Callotasis, coarse	211,608	3.45	7.56	6.77	3.70
Reference, fine	1,338,189	19.97	46.26	35.14	16.59
Reference, coarse	187,479	19.40	44.22	34.19	16.17

Table 3.2: Stiffness measures of the FE model using equation (3.3).

	D.O.F.	Compression [kN/mm]	Bending ML [Nm/°]	Bending AP [Nm/°]	Torsion [Nm/°]
Initial:					
Callotasis, fine	1,076,955	3.55	6.49	5.68	2.38
Callotasis, coarse	147,915	3.75	6.94	5.92	2.82
Reference, fine	967,512	21.78	49.77	35.98	20.64
Reference, coarse	136,371	21.93	49.58	36.24	21.15
Final:					
Callotasis, fine	1,528,068	7.61	15.68	14.63	8.12
Callotasis, coarse	211,608	7.98	16.34	15.28	8.75
Reference, fine	1,338,189	18.30	40.61	32.35	17.41
Reference, coarse	187,479	18.54	40.84	32.64	17.74

3.5.4 Discussion

In the present study, we have demonstrated how subject specific FE models can be used to isolate a callus distraction and assess its consolidation. The cross-sectional distribution of the bone tissue is as important for the mechanical stability of the callus distraction as the mechanical properties of the bone tissue itself. Much of this information is lost when using projected images such as plain radiography and DEXA.

Quantitative CT provides both the degree of tissue mineralization and its spatial distribution, and has shown promising results for evaluating the mechanical stability of leg lengthenings (Reichel et al., 1998; Aronson and Shin, 2003). However, for an orthopaedic surgeon who is used to plain radiography, it can be difficult to assess the mechanical stability from a series of CT images. By combining FE models with quantitative CT, the measurement of mineral density is put in context of its spatial distribution and directly produces an estimate of the mechanical properties of the studied section. Voxel FE models are easy to build and require only a few manual operations. In our case, two subsets of CT images were selected: one for the callus distraction and one for the reference section. Five closed curves had to be drawn manually in five CT images of each section to define the ROIs of the FE models, requiring less than 5 minutes of "manual labour". The reference section was chosen directly below the distraction gap to represent the mineral content and cross sectional tissue distribution of mature bone in the affected tibia. The contralateral tibia will have a higher degree of mineralization and be more rigid than the ipsilateral tibia which suffers bone loss due to immobilization. The mineralization of the callus distraction during the consolidation phase is therefore more likely to converge towards that of the ipsilateral tibia rather than the contralateral.

Animal studies have shown good correlation between the stiffness and the strength of callotases (Windhagen et al., 2000; Floerkemeier et al., 2005). Since a future validation of the method probably would involve biomechanical testing on patients, stiffness was used as an indicator of the healing rather than strength. Four simplified types of loading were simulated: compression, torsion and bending about two axes. This gives an indication about both the mineral density of the bone regenerate and the structure of the callus distraction, i.e. the cross-sectional area, polar and 2. moment of area.

The element size may affect the results if the element size is too big to reflect the structural architecture and too small to satisfy continuum material assumption (Homminga et al., 2001; Verhulp et al., 2006). Homminga et al. (2001) showed that the mechanical behaviour of a porous structure could be described using the gray-value procedure for elements sizes on the order of the trabecular thickness. For element sizes larger than the trabecular thickness, the predictions of apparent Young's modulus remained largely accurate in the axial direction while becoming increasingly inaccurate in the transverse direction. The element sizes in our FE models were approximately two to four times the trabecular thickness. Even though the image resolutions used in the present study are not optimal for FE modelling, they are representative for what is feasible with whole-body CT scanners.

Several methods of determining fracture healing by mechanical measurements have been proposed. Hammer et al. (1984) used bending to measure the *deflection ratio* of tibial fractures. The limit for a healed tibial fracture was set to a deflection ratio of 0.08, which translates into 12.5 Nm/° for a body weight of 75 kg. Similarly, Richardson et al. (1994) proposed a limit of 15 Nm/° for tibial fractures, and this criterion was later used for determining the consolidation of leg lengthenings (Dwyer et al., 1996). Other studies measuring the stiffness and strength for torsion and uniaxial loads, have reported the material properties of the lengthened leg at removal of the frame to be around 27% to 63% percent compared to intact (Walsh et al., 1994; Aronson et al., 1997; Aronson and Shin, 2003). The FE models of the callus distraction gave results that were within the ranges reported in literature (Richardson et al., 1994; Dwyer et al., 1996; Aronson and Shin, 2003; Aarnes et al., 2005; Floerkemeier et al., 2005; Aarnes et al., 2006) and show a considerable increase in stiffness from the initial to the final state. From table 3.1 and table 3.2 we also see that the two material models gave significantly different stiffnesses, with (3.3) estimating the bending stiffness just above the safe level of 15 Nm/^{o} (Dwyer et al., 1996) at the final state, while (3.2) estimates it to be almost half the safe level. The stiffnesses for the callus distraction at the final state in table 3.2 are approximately half the stiffnesses in the reference section. This is similar to the results reported by Aronson (2003) who found the compressive and torsional stiffness of the a callus distraction at removal of the frame to be 47% and 43% compared to the control bone. Coarsening the mesh had little effect on the stiffness properties of the FE models, but reduced the required computation resources and time considerably.

Figure 3.14 shows an increase in mineral density in the callus distraction over time, while a slight decrease is observed in the reference section. Bone loss in an immobilized extremity is a well known effect and may account for some of this reduced mineralization measured in the reference section (Reichel et al., 1998; Eyres et al., 1993b). Another explanation is metal artifacts from the external frame affecting the estimates of bone mineral density. Salmas et al. (1998) found that the metal artifacts from the Ilizarov frame gave a small (≈ 40HU) increase in CT attenuation values. This corresponds very well with our measurements showing the average CT attenuation value in the reference section decrease from 660HU to 624HU. The metal artifacts can be seen as straight lines between the rods. Since the tibia is not coaxial with the center axis of the external frame, the tibia avoids the most pronounced metal artifacts (figure 3.15).

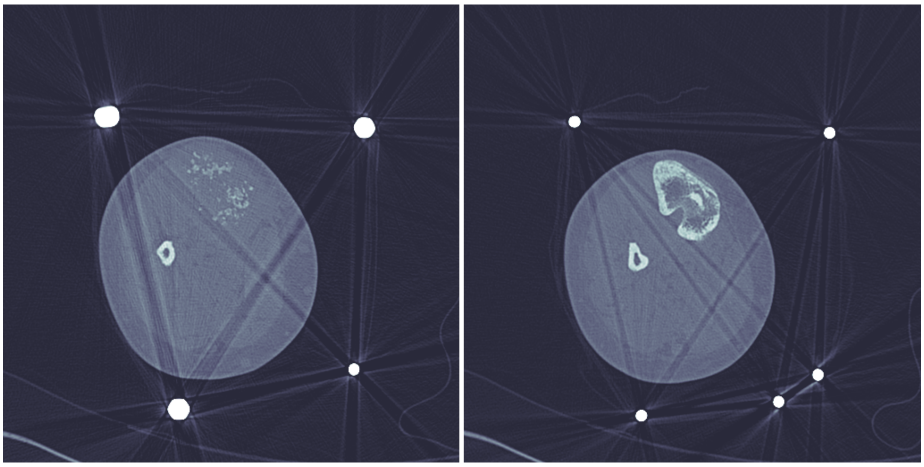

Figure 3.15: Metal artifacts in the CT scans of the callus distraction (left) and the reference section (right).

Equation (3.2) with a cubic density-stiffness relationship, gave a decreased stiffness in the reference section of 26% from the initial to the final state, while equation (3.3) with a power term of 1.5 gave a decrease of 15%. The reference section was chosen directly below the distraction gap and has a similar pattern of streak artifacts. If no major changes are made to the external frame, the metal artifacts will also be the same in CT scans taken at different stages in the consolidation phase. The degree of overestimation of bone mineral density and stiffness measures will thus be consistent throughout the consolidation phase and in both the distracted and reference section, and can therefore still be used to assess the development of mechanical stability of the bone regenerate.

Plain radiography is the most common method for assessing the maturity of a leg lengthening. The orthopaedic surgeon makes a subjective judgement of the stiffness and strength of the callus distraction, and the verdict will vary between different surgeons (Blokhuis et al., 2001; Starr et al., 2004; Donnan et al., 2002; Anand et al., 2006). Starr et al. (2004) characterized the inter- and intra-observer variability in deciding when to remove the external frame as being "moderately better than chance". Combining quantitative CT with FE analysis as presented in this study gives the orthopaedic surgeon an estimate of the mechanical stability of the callus distraction. We did not have any experimental measurements to validate our FE models. Although this represents a shortcoming, it also illustrates the motivation of the study; there is no reliable method for measuring the mechanical stability of a callus distraction with an Ilizarov frame, and we therefore want to use the FE method. A validation of the FE models is planned for future work. The authors believe that despite the obstacles regarding material modelling and metal artifacts in the images, quantitative CT combined with FE analysis can provide valuable information and could be used clinically.

Acknowledgements

The study was financed by the Norwegian Orthopaedic Implant Research Unit at St. Olavs Hospital in Trondheim. The project was granted computational time by the Norwegian University of Science and Technology at the Notur High Performance Computing Consortium. The authors would also like to thank the patient for participating in the study and Liv Nesje for assisting with CT scanning.

References

Aarnes, G. T., Steen, H., Kristiansen, L. P., Festo, E., Ludvigsen, P., (2006). Optimum loading mode for axial stiffness testing in limb lengthening. J.Orthop Res. 24**,** 348-354.

Aarnes, G. T., Steen, H., Ludvigsen, P., Waanders, N. A., Huiskes, R., Goldstein, S. A., (2005). In vivo assessment of regenerate axial stiffness in distraction osteogenesis. J.Orthop.Res. 23**,** 494-498.

Anand, A., Feldman, D. S., Patel, R. J., Lehman, W. B., van Bosse, H. J., Badra, M. I., Sala, D. A., (2006). Interobserver and intraobserver reliability of radiographic evidence of bone healing at osteotomy sites. J.Pediatr.Orthop B 15**,** 271-272.

Aro, H. T., Wipperman, B. W., Hodgson, S. F., Warner, H. W., Lewallen, D. G., Chao, E. Y. S., (1989). Prediction of properties of fracture callus by measurement of mineral density using micro bone densitometry. J.Bone Joint Surg 71A**,** 1020-1030.

Aronson, J., Good, B., Stewart, C., Harrison, B., Harp, J., (1990). Preliminary studies of mineralization during distraction osteogenesis. Clin.Orthop Relat Res. 43-49.

Aronson, J., Harrison, B. H., Stewart, C. L., Harp, J. H., Jr., (1989). The histology of distraction osteogenesis using different external fixators. Clin.Orthop Relat Res. 106-116.

Aronson, J., Shen, X. C., Skinner, R. A., Hogue, W. R., Badger, T. M., Lumpkin, C. K., Jr., (1997). Rat model of distraction osteogenesis. J.Orthop Res. 15**,** 221-226.

Aronson, J., Shin, H. D., (2003). Imaging techniques for bone regenerate analysis during distraction osteogenesis. J.Pediatr.Orthop. 23**,** 550-560.

Augat, P., Merk, J., Genant, H. K., Claes, L., (1997). Quantitative assessment of experimental fracture repair by peripheral computed tomography. Calcif.Tissue Int. 60**,** 194-199.

Bail, H. J., Kolbeck, S., Krummrey, G., Weiler, A., Windhagen, H. J., Hennies, K., Raun, K., Raschke, M. J., (2002). Ultrasound can predict regenerate stiffness in distraction osteogenesis. Clin.Orthop Relat Res. 362-367.

Beaty, J. H., (1992). Congenital Anomialies of Lower Extremity. In: Crenshaw, A. H. (Ed.), Campbell's Operative Ortopaedics. Mosby - Year Book, Inc., pp. 2059-2212.

Blokhuis, T. J., de Bruine, J. H., Bramer, J. A., den Boer, F. C., Bakker, F. C., Patka, P., Haarman, H. J., Manoliu, R. A., (2001). The reliability of plain radiography in experimental fracture healing. Skeletal Radiol. 30**,** 151-156.

Boccaccio, A., Pappalettere, C., Kelly, D. J., (2007). The influence of expansion rates on mandibular distraction osteogenesis: a computational analysis. Ann.Biomed.Eng 35**,** 1940-1960.

Brutscher, R., (1994). Biological principles of callus distraction. Injury 25 Suppl 1**,** A27-A28.

Carter, D. R., Beaupre, G. S., Giori, N. J., Helms, J. A., (1998). Mechanobiology of skeletal regeneration. Clin.Orthop Relat Res. 355 Suppl**,** S41-S55.

Carter, D. R., Hayes, W. C., (1977). The compressive behavior of bone as a two-phase porous structure. J.Bone Joint Surg Am. 59**,** 954-962.

Cauchoix, J., Morel, G., (1978). One stage femoral lengthening. Clin.Orthop Relat Res. 66-73.

Choi, K., Kuhn, J. L., Ciarelli, M. J., Goldstein, S. A., (1990). The elastic moduli of human subchondral, trabecular, and cortical bone tissue and the size-dependency of cortical bone modulus. J.Biomech. 23, 1103-1113.

Chotel, F., Braillon, P., Sailhan, F., Gadeyne, S., Gellon, J. O., Panczer, G., Pedrini, C., Berard, J., (2008a). Bone stiffness in children: part II. Objectives criteria for children to assess healing during leg lengthening. J.Pediatr.Orthop 28, 538-543.

Chotel, F., Braillon, P., Sailhan, F., Gadeyne, S., Panczer, G., Pedrini, C., Berard, J., (2008b). Bone stiffness in children: part I. In vivo assessment of the stiffness of femur and tibia in children. J.Pediatr.Orthop 28, 534-537.

Cody, D. D., Gross, G. J., Hou, F. J., Spencer, H. J., Goldstein, S. A., Fyhrie, D. P., (1999). Femoral strength is better predicted by finite element models than QCT and DXA. J.Biomech. 32, 1013-1020.

Crawford, R. P., Cann, C. E., Keaveny, T. M., (2003). Finite element models predict in vitro vertebral body compressive strength better than quantitative computed tomography. Bone 33, 744-750.

den Boer, F. C., Bramer, J. A., Patka, P., Bakker, F. C., Barentsen, R. H., Feilzer, A. J., de Lange, E. S., Haarman, H. J., (1998). Quantification of fracture healing with three-dimensional computed tomography. Arch Orthop Trauma Surg 117, 345-350.

Donnan, L. T., Saleh, M., Rigby, A. S., McAndrew, A., (2002). Radiographic assessment of bone formation in tibia during distraction osteogenesis. J.Pediatr.Orthop 22, 645-651.

Dwyer, J. S., Owen, P. J., Evans, G. A., Kuiper, J. H., Richardson, J. B., (1996). Stiffness measurements to assess healing during leg lengthening. A preliminary report. J.Bone Joint Surg Br. 78, 286-289.

Eyres, K. S., Bell, M. J., Kanis, J. A., (1993a). Methods of assessing new bone formation during limb lengthening. Ultrasonography, dual energy X-ray absorptiometry and radiography compared. J.Bone Joint Surg Br. 75, 358-364.

Eyres, K. S., Bell, M. J., Kanis, J. A., (1993b). New bone formation during leg lengthening. Evaluated by dual energy X-ray absorptiometry. J.Bone Joint Surg Br. 75, 96-106.

Fischgrund, J., Paley, D., Suter, C., (1994). Variables affecting time to bone healing during limb lengthening. Clin.Orthop Relat Res. 31-37.

Fleming, B., Paley, D., Kristiansen, T., Pope, M., (1989). A biomechanical analysis of the Ilizarov external fixator. Clin.Orthop Relat Res. 95-105.

Floerkemeier, T., Hurschler, C., Witte, F., Wellmann, M., Thorey, F., Vogt, U., Windhagen, H., (2005). Comparison of various types of stiffness as predictors of the load-bearing capacity of callus tissue. J.Bone Joint Surg Br. 87, 1694-1699.

Garcia, F. L., Picado, C. H., Garcia, S. B., (2008). Histology of the regenerate and docking site in bone transport. Arch Orthop Trauma Surg.

Gibson, L. J., (1985). The mechanical behaviour of cancellous bone. J.Biomech. 18, 317-328.

Hamanishi, C., Yasuwaki, Y., Kikuchi, H., Tanaka, S., Tamura, K., (1992). Classification of the callus in limb lengthening. Radiographic study of 35 limbs. Acta Orthop Scand. 63, 430-433.

Hamdy, R. C., Walsh, W., Olmedo, M., Wallach, M., Ehrlich, M. G., (1995). Correlation between ultrasound imaging and mechanical and physical properties of lengthened bone: an experimental study in a canine model. J.Pediatr.Orthop 15, 206-211.

Hammer, R., Edholm, P., Lindholm, B., (1984). Stability of union after tibial shaft fracture. Analysis by a non-invasive technique. J.Bone Joint Surg Br. 66, 529-534.

Harp, J. H., Aronson, J., Hollis, M., (1994). Noninvasive determination of bone stiffness for distraction osteogenesis by quantitative computed tomography scans. Clin.Orthop Relat Res. 301, 42-48.

Harrigan, T. P., Jasty, M., Mann, R. W., Harris, W. H., (1988). Limitations of the continuum assumption in cancellous bone. J.Biomech. 21, 269-275.

Herron, L. D., Amstutz, H. C., Sakai, D. N., (1978). One stage femoral lengthening in the adult. Clin.Orthop Relat Res. 74-82.

Homminga, J., Huiskes, R., Rietbergen, B. v., Ruegsegger, P., Weinans, H., (2001). Introduction and evaluation of a gray-value voxel conversion technique. J.Biomech. 34, 513-517.

Ilizarov, G. A., (1989). The tension-stress effect on the genesis and growth of tissues. Part I. The influence of stability of fixation and soft-tissue preservation. Clin.Orthop Relat Res. 249-281.

Ilizarov, G. A., (1990). Clinical application of the tension-stress effect for limb lengthening. Clin.Orthop Relat Res. 250, 8-26.

Ilizarov, G. A., Ledyaev, V. I., (1992). The replacement of long tubular bone defects by lengthening distraction osteotomy of one of the fragments. 1969. Clin.Orthop Relat Res. 280, 7-10.

Isaksson, H., Comas, O., van Donkelaar, C. C., Mediavilla, J., Wilson, W., Huiskes, R., Ito, K., (2007). Bone regeneration during distraction osteogenesis: Mechano-regulation by shear strain and fluid velocity. J.Biomech. 40, 2002-2011.

Isaksson, H., Wilson, W., van Donkelaar, C. C., Huiskes, R., Ito, K., (2006). Comparison of biophysical stimuli for mechano-regulation of tissue differentiation during fracture healing. J.Biomech. 39, 1507-1516.

Karaharju, E. O., Aalto, K., Kahri, A., Lindberg, L. A., Kallio, T., Karaharju-Suvanto, T., Vauhkonen, M., Peltonen, J., (1993). Distraction bone healing. Clin.Orthop Relat Res. 38-43.

Keyak, J. H., Meagher, J. M., Skinner, H. B., Mote, C. D., Jr., (1990). Automated three-dimensional finite element modelling of bone: a new method. J.Biomed.Eng 12, 389-397.

Kolbeck, S., Bail, H., Weiler, A., Windhagen, H., Haas, N., Raschke, M., (1999). Digital radiography. A predictor of regenerate bone stiffness in distraction osteogenesis. Clin.Orthop.Relat Res. 221-228.

Leong, P. L., Morgan, E. F., (2008). Measurement of fracture callus material properties via nanoindentation. Acta Biomater.

Li, R., Saleh, M., Yang, L., Coulton, L., (2006). Radiographic classification of osteogenesis during bone distraction. J.Orthop Res. 24, 339-347.

Malizos, K. N., Hantes, M. E., Protopappas, V., Papachristos, A., (2006). Low-intensity pulsed ultrasound for bone healing: an overview. Injury 37 Suppl 1, S56-S62.

Markel, M. D., Chao, E. Y., (1993). Noninvasive monitoring techniques for quantitative description of callus mineral content and mechanical properties. Clin.Orthop Relat Res. 37-45.

Markel, M. D., Wikenheiser, M. A., Chao, E. Y., (1990). A study of fracture callus material properties: relationship to the torsional strength of bone. J.Orthop.Res. 8, 843-850.

Moorcroft, C. I., Ogrodnik, P. J., Thomas, P. B., Wade, R. H., (2001). Mechanical properties of callus in human tibial fractures: a preliminary investigation. Clin.Biomech. 16, 776-782.

Morgan, E. F., Bayraktar, H. H., Keaveny, T. M., (2003). Trabecular bone modulus-density relationships depend on anatomic site. J.Biomech. 36, 897-904.

Njeh, C. F., Fuerst, T., Hans, D., Blake, G. M., Genant, H. K., (1999). Radiation exposure in bone mineral density assessment. Appl.Radiat.Isot. 50, 215-236.

Paley, D., (1990). Problems, obstacles, and complications of limb lengthening by the Ilizarov technique. Clin.Orthop Relat Res. 250, 81-104.

Phillips, A. M., (2005). Overview of the fracture healing cascade. Injury 36 Suppl 3, S5-S7.

Prat, J., Juan, J. A., Vera, P., Hoyos, J. V., Dejoz, R., Peris, J. L., Sanchez-Lacuesta, J., Comin, M., (1994). Load transmission through the callus site with external fixation systems: theoretical and experimental analysis. J.Biomech. 27, 469-478.

Reichel, H., Lebek, S., Alter, C., Hein, W., (1998). Biomechanical and densitometric bone properties after callus distraction in sheep. Clin.Orthop Relat Res. 237-246.

Rho, J. Y., Ashman, R. B., Turner, C. H., (1993). Young's modulus of trabecular and cortical bone material: ultrasonic and microtensile measurements. J.Biomech. 26, 111-119.

Richardson, J. B., Cunningham, J. L., Goodship, A. E., O'Connor, B. T., Kenwright, J., (1994). Measuring stiffness can define healing of tibial fractures. J.Bone Joint Surg Br. 76, 389-394.

Salmas, M. G., Nikiforidis, G., Sakellaropoulos, G., Kosti, P., Lambiris, E., (1998). Estimation of artifacts induced by the Ilizarov device in quantitative computed tomographic analysis of tibiae. Injury 29, 711-716.

Schileo, E., Taddei, F., Malandrino, A., Cristofolini, L., Viceconti, M., (2007). Subject-specific finite element models can accurately predict strain levels in long bones. J.Biomech. 40, 2982-2989.

Schneider, W., Bortfeld, T., Schlegel, W., (2000). Correlation between CT numbers and tissue parameters needed for Monte Carlo simulations of clinical dose distributions. Phys.Med.Biol. 45, 459-478.

Shefelbine, S. J., Simon, U., Claes, L., Gold, A., Gabet, Y., Bab, I., Muller, R., Augat, P., (2005). Prediction of fracture callus mechanical properties using micro-CT images and voxel-based finite element analysis. Bone 36, 480-488.

Starr, K. A., Fillman, R., Raney, E. M., (2004). Reliability of radiographic assessment of distraction osteogenesis site. J.Pediatr.Orthop 24, 26-29.

Thorey, F., Windhagen, H., Linnenberg, D., Nolle, O., Maciejewski, O., Spies, C., (2000). [Assessment of bone healing during callus distraction by an automatic torsional stiffness metering system]. Biomed.Tech.(Berl) 45, 343-348.

Tselentakis, G., Owen, P. J., Richardson, J. B., Kuiper, J. H., Haddaway, M. J., Dwyer, J. S., Evans, G. A., (2001). Fracture stiffness in callotasis determined by dual-energy X-ray absorptiometry scanning. J.Pediatr.Orthop B 10, 248-254.

Verhulp, E., Rietbergen, B. v., Huiskes, R., (2006). Comparison of micro-level and continuum-level voxel models of the proximal femur. J.Biomech. 39, 2951-2957.

Walsh, W. R., Hamdy, R. C., Ehrlich, M. G., (1994). Biomechanical and physical properties of lengthened bone in a canine model. Clin.Orthop Relat Res. 306**,** 230-238.

Windhagen, H., Bail, H., Schmeling, A., Kolbeck, S., Weiler, A., Raschke, M., (1999). A new device to quantify regenerate torsional stiffness in distraction osteogenesis. J.Biomech. 32**,** 857-860.

Windhagen, H., Kolbeck, S., Bail, H., Schmeling, A., Raschke, M., (2000). Quantitative assessment of in vivo bone regeneration consolidation in distraction osteogenesis. J.Orthop Res. 18**,** 912-919.

Wraighte, P., Scammell, B., (2006). Principles of fracture healing. Surgery (Oxford) 24**,** 198-207.

Young, J. W., Kostrubiak, I. S., Resnik, C. S., Paley, D., (1990). Sonographic evaluation of bone production at the distraction site in Ilizarov limb-lengthening procedures. AJR Am.J.Roentgenol. 154**,** 125-128.

Chapter 4: Subject specific FE analysis of human femurs with prosthesis

4.1 Background

Total hip replacement (THR) is the surgical procedure of replacing a dysfunctional hip joint with an artificial joint, in order to provide pain relief and restore the function of the hip. Impairment of joint function may have many causes, but osteoarthritis is the most common and accounts for 70-80% of the hip operations. In a healthy joint the articular surfaces are smooth and lubricated by synovial fluid resulting in a joint with very low friction. Osteoarthritis simply means that the articular surfaces of the joints are worn out, and have lost their low-friction properties. The condition makes motion of the joint difficult and painful, and can at worst be disabling. It is especially prevalent in the hip and knee joints, which are exposed to loads two to three times the body weight during normal walking (Bergmann et al., 1993; 2001) and may endure thousands of load cycles daily (Morlock et al., 2001). As of today, there is no method of regenerating and repairing the articular cartilage. Instead, severe osteoarthritis is treated by replacing the old, damaged joint with a new, artificial joint. The procedure of THR was pioneered in the 1960s by Sir John Charnley, and is regarded as one of the most successful procedures in surgery. The procedure involves removing the acetabular socket and replacing it with an artificial cup fixated into the pelvis. The femoral head and neck is resected and the porous bone rasped out of the proximal femur to give room for a femoral stem inside the medullary cavity (figure 4.1). THR usually fully restores the function of the joint, and enables the patient to move around without any pain.

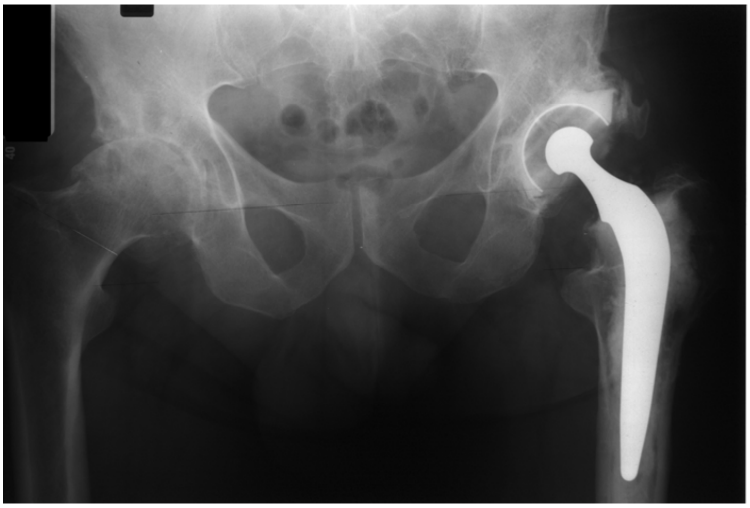

Figure 4.1: THR in a patient. The hip joint on the patients left side has been completely replaced with artificial components: the acetabular socket has been replaced with a polymer cup cemented into the pelvis, and the femoral head and neck with a stem cemented into the femur.

Between 86 and 170 hips are replaced per 100,000 population annually in the industrialised world (Canadian Institute for Health Information, 2008). In Norway, this amounts to 7000-8000 hip operations every year, where 85% are replacements of the original hip (primary surgery) and 15% are replacements of old implants (revision surgery) (The Norwegian Arthroplasty Register, 2008). The survival rate of hip implants is generally quite good for primary implants (~90% after 11 years), but becomes increasingly worse by each revision; respectively 77% and 67% at 11 years for the first and second revision (Danish Hip Arthroplasty Register, 2008). Due to the large volume of operations, implant failure and the need for reoperation will affect an increasing number of patients. A lot of effort is therefore put into developing new implants that will improve the long time performance of THR.

A wide range of prosthetic designs for THR from several manufacturers are available to the orthopaedic surgeon, and new designs are introduced on the market every year. Pre-clinical evaluation is therefore imperative to ensure safe treatment of the patients, and to make sure that inferior prosthetic designs are not put into use. When evaluating a new prosthetic design, two aspects of the prosthesis are usually tested; the implant stability, and the change in bone stress/strain induced by the femoral implant. Initial implant stability is especially important for cementless stems that rely on osseointegration, as excessive implant micromotion inhibits bone ingrowth (Jasty et al., 1997). Inserting a metal stem in the femoral canal reduces stress in the surrounding bone, socalled stress shielding. Since bone adapts according to the load distribution in the tissue, a reduction in the mechanical stimulus to the bone will induce bone loss. This may in turn impair the stability of the prosthesis, increase the risk of bone fracture and complicate revision surgery.

Prosthetic designs are usually evaluated in experimental studies using human cadaver bones. However, there are several drawbacks with using real human femurs: necessary authorizations must be obtained before collecting the femurs, supply is limited, bones can usually only be implanted once, and a large selection of bones is required due to individual variations in bone geometry and material properties. Composite bone replicas were introduced to simplify experimental testing of new implant designs (Stolk et al., 2002a; Viceconti et al., 2001). They are easier to handle and prepare for testing, have a standardized geometry and the mechanical properties are known. This makes composite femurs ideal for comparing different implant designs and testing new design features. However, patients do not come in standardized shapes and sizes. It is therefore important that new implants also are tested in a wide range of femurs with geometries and mechanical properties reflecting the variation seen in patients.

Finite element (FE) models have been used extensively in biomechanics to study the effect of different implants, and also to simulate the adaptive response of the surrounding bone (Rietbergen et al., 1993; Turner et al., 2005; Lengsfeld et al., 2005). Subject specific FE models derived from computed tomography (CT) have been presented in a numerous studies, but have usually been concerned with intact femurs (Taddei et al., 2006; Schileo et al., 2007; Yosibash et al., 2007; Lengsfeld et al., 1998) and predictions of femoral fracture strength (Keyak et al., 1998; Cody et al., 1999; Keyak and Rossi, 2000; Bessho et al., 2006; Schileo et al., 2008). The vast majority of FE studies of bones with prosthetic implants have relied on composite replicas for validation (McNamara et al., 1997; Viceconti et al., 2001; Lennon and Prendergast, 2001; Stolk et al., 2002a). Rohlmann et al. (1983) analysed strains in a femur with prosthesis and validated the result against strain gauge measurement, but did not include results for the intact bone. Analyses of implant micromotion have been presented in a few studies using subject specific FE models (Rubin et al., 1993; Reggiani et al., 2007; Abdul-Kadir et al., 2008), but usually only include very few femurs (one or two).

The present chapter will describe how subject specific FE models can be employed for evaluating the design of femoral implants. With this approach, the designer can test new implants in a wide range of virtual femoral models spanning the variation seen in patients. The FE models are easily modified and can be employed to test different design features. In the present chapter we will first present the procedure of creating the subject specific FE models (section 4.2). The choice of density-stiffness relationship employed in the FE models is addressed in section 4.3. The subject specific FE models are then validated against in vitro measurements of cortical strain and implant stability in sections 4.4 and 4.5.

4.2 Creating the FE model

4.2.1 Retrieving the femoral geometry

The first step of creating the subject specific FE model is to retrieve the geometry of the bone. The femurs were scanned using a multislice CT scanner (Siemens Somatom Sensation 64, Erlangen, Germany). The slice thickness of the CT images was set as thin as possible (0.75 mm) to reduce the effect of partial volume averaging over the image thickness. Additionally, the distance between the image slices was set very low (0.7 mm) to get enough CT pixels to determine bone density of each element. A scan series of one femur might thus consist of more than 700 CT images.

Before starting to extract the contours of the femur, the CT scans that should be used for creating the geometry of the FE model were selected. Figure 4.2 shows four levels selected manually by the user: the proximal levels of the femoral head (caput) and the greater trochanter, and the mid-levels of the lesser trochanter and the condyles. A level 20 mm below the lesser trochanter was used to define the regions of proximal femur and the femoral shaft. The geometry of the proximal femur is fairly complex, while the midshaft region is almost cylindrical. Contours were therefore extracted at 4 mm intervals in the proximal femur, and at 20 mm intervals for the femoral shaft. In the experimental setup, the femurs were potted distally in a steel cylinder at a distance of 25 cm from the greater trochanter (Aamodt et al., 2001). The femoral geometry was therefore retrieved down to the distal level of the femoral shaft as indicated in figure 4.2. Contours at the level of the condyles were also extracted, but only used as a guide to determine femur length and orientation, and not used in the FE model itself.

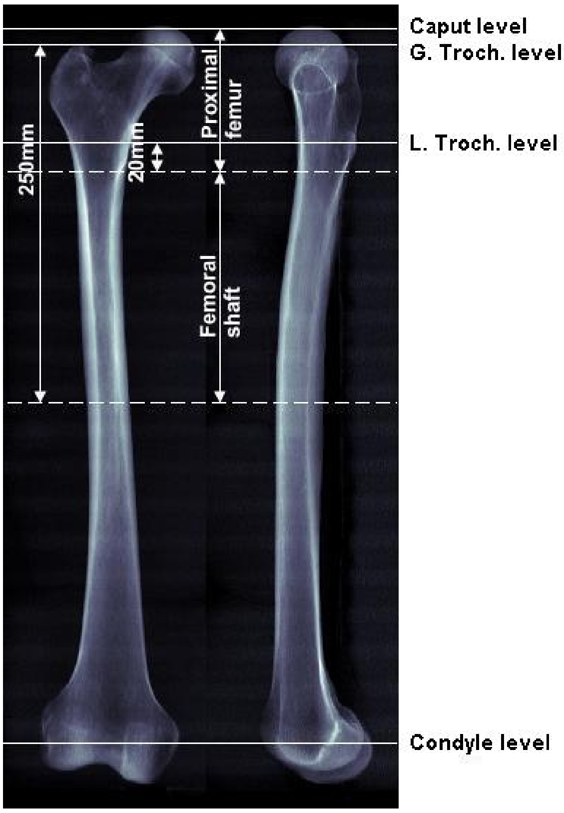

Figure 4.2: Medio-lateral and antero-posterior views of a femur reconstructed from projections of the CT images. The levels of proximal caput, greater trochanter (G.Troch.), lesser trochanter (L.Troch.) and the condyles (solid lines) are picked manually. The levels defining the femoral shaft (slashed lines) are at a fixed distance from trochanter major and minor for all femurs.

Inner and outer contours of the bone are usually extracted by defining a threshold value for cortical bone (Viceconti et al., 1999; Rubin et al., 1993; Aamodt et al., 1999), and then employing a border tracing algorithm (Testi et al., 2001). A border tracing algorithm returns all pixel positions along the selected threshold value in sequential order, and the number of points must therefore be reduced and the contours smoothened to enable reconstruction of the 3D geometry. In the proximal femur the cortical wall is often so thin it appears not to be continuous, but to have several holes in it. The border tracing algorithm will then trace the contour of the cortical wall through the hole, and thus fail in extracting separate inner and outer contours. The crux of implementing the border tracing algorithm therefore lies in programming all the help functions that are needed when the algorithm fails, and to smoothen the contours and reduce the number of points.

In the present thesis an alternative and less elegant approach for segmenting the images was used. It involves some manual work to correct the contours, but creates fewer points along the contour which makes the contours easier to manage. Hangartner and Gilsanz (1996) showed that the interface between two adjacent materials is best determined using a relative threshold for the difference in HU values of the two. A relative threshold of 50% was used to extract the contours of cortical bone, which means that the average HU value of the two adjacent materials determines the interface. A region of interest (ROI) around the bone section in the CT scans was first defined automatically by the program based on a threshold of 400 HU. In cases where the program failed to correctly locate the bone region, the ROI was adjusted manually. Radial profiles from the center of ROI were used to determine the inner and outer cortical contours. The maximum HU value along the radial line was assumed to be the midsection of the cortical wall. Radiographic densities of 200 HU for cancellous bone and 0 HU for soft tissue/water were assumed to define the relative thresholds for inner and outer contours, respectively. Thus, for a maximum density of 1200 HU along the radial line defining the midsection of the cortical wall, the thresholds are 700 and 600 HU for the inner and outer contours, respectively. The angular increment of the radial line was set to 5 degrees giving closed curves of 72 points. The described procedure works well in the region of the femoral shaft where the cortical wall is well defined. In the proximal regions, the cortical wall is very thin and the cross sectional shape is more complex. The automatically generated contours were therefore revised and corrected manually (figure 4.3).

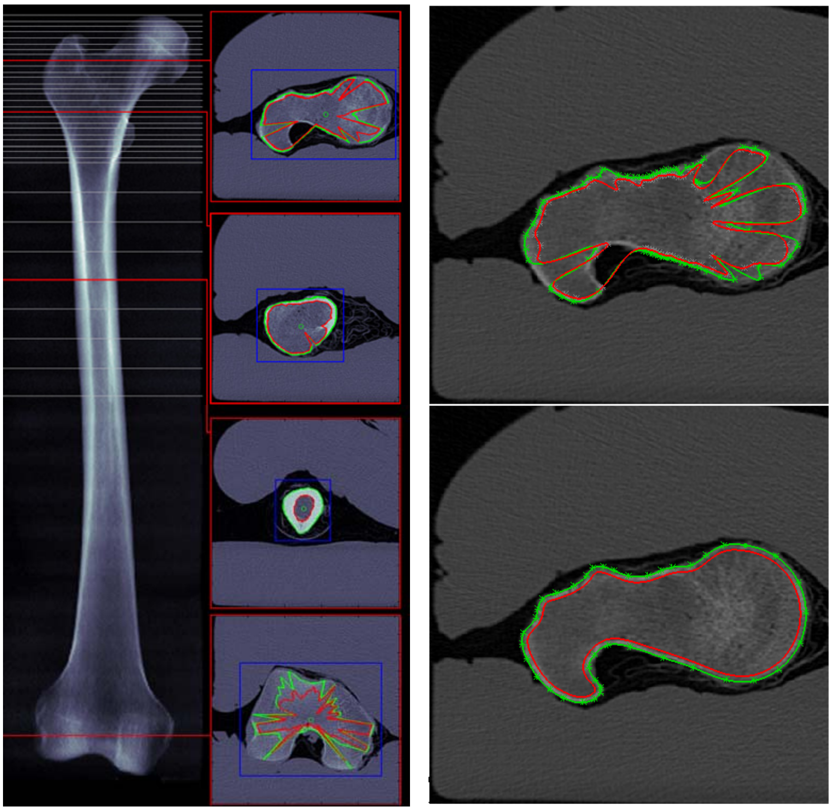

Figure 4.3: Initial contours are generated automatically (left). The program suggests a ROI (blue box) and uses the HU profile of the radial lines from the center of the ROI to create the contours. The automatically generated contours (above right) are subsequently revised and corrected in Solidworks (below right).

After revising the contours, the contours were imported into a CAD program (SolidWorks 2005, Solidworks Corporation, Concord, USA). Figure 4.4 (left) shows the inner and outer contours derived from the CT scans outlining the shape of the femur. Guide curves between the contours are needed to connect the contours and create the 3D model of the femur. Two reference planes were defined by the user. Guide curves were determined by the intersection points between the reference planes and the contours. The finished 3D model of the femur is shown in figure 4.4 (center). The cancellous bone was lofted from the inner contours of the proximal femur, while inner contours of the femoral shaft were used for the medullary canal. The medullary canal was only used for creating the cavity in the cortical bone, and was not used for the FE model itself.

The 3D models were meshed (CosmosWorks 2005, Solidworks Corporation, Concord, USA) using 2nd order tetrahedral elements with a global size of 3 mm (figure 4.4, right).

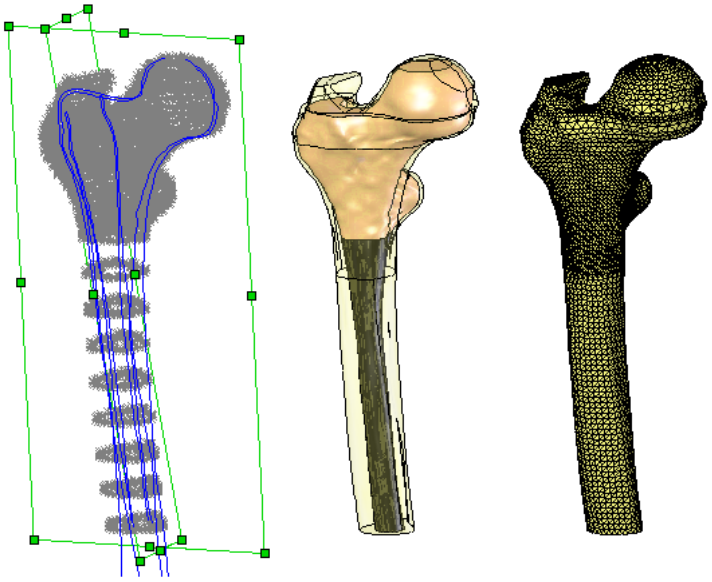

Figure 4.4: By positioning the two reference planes, the path of the guide curves are defined (left). The lofted 3D models of cortical bone, cancellous bone and the medullary canal (center), and the finished meshed model of the intact femur (right).

4.2.2 Determining the HU value at each element location

In order to assign material properties to the elements in our FE models, the CT pixels located inside the element must be identified. The node coordinates of the FE model are converted from cartesian spatial coordinates (xyz) into image pixel indeces (i and j) and image slice number (k). The element spanning the most CT images is then identified in the FE model. The number of CT images spanned by this element (h_{max}) is used to partition the job of identifying CT pixels located inside each element into smaller tasks requiring less memory.

A set of CT images equal to $2 \cdot h_{max}$ is loaded into the program and only elements that are located completely inside this segment are processed (figure 4.5, left). In order to reduce the subset of pixels that will be tested, a box around the element is defined by its minimum and maximum coordinates to reduce the number of pixels that will be considered (figure 4.5, right).

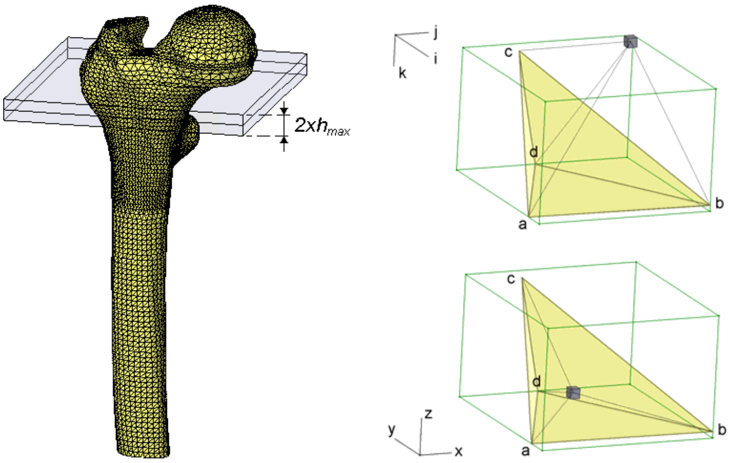

Figure 4.5: The job of identifying average HU value of each element is partitioned into smaller jobs. A segment of CT scans equal to $2\cdot h_{max}$ is handled at a time to reduce the required memory. A box (green) defines the subset of pixels around the tetrahedral element. Each pixel in the subset is tested to determine if it is located inside the tetrahedron.

The process of identifying the pixels located inside the tetrahedral element was described by Zannoni et al. (1998). The volume of a tetrahedron can be determined from the determinant of the matrix:

$$V = \frac{1}{6} \cdot \begin{vmatrix} a_x & a_y & a_z & 1 \\ b_x & b_y & b_z & 1 \\ c_x & c_y & c_z & 1 \\ d_x & d_y & d_z & 1 \end{vmatrix} \tag{4.1}$$

For a tetrahedral element we can define four tetrahedral volumes between the four element faces and any point (CT pixel or voxel) in space. If the sum of these four tetrahedral volumes is greater than the volume of the element, the pixel is located outside the element. If the sum of the volumes is equal to the volume of the element, it is located inside the element. The average HU value of pixels located inside the tetrahedron were calculated for each element. If the element is too small compared to pixel size and slice distance, the average HU value was calculated from the pixels closest to the corner nodes. After all the elements inside the segment $2 \cdot h_{max}$ have been processed, the segment moves up a height equal to h_{max}, thus always overlapping a number of CT scans equal to h_{max} with the former segment. Any elements that were only partially inside one segment will be completely inside the next, and all elements will be processed in due course. The elements were organised in element sets by their HU value and assigned material properties accordingly.

4.2.3 Modelling the implanted femur

Achieving proper positioning of the prosthesis is imperative for the success of a total hip replacement. The prosthesis should be oriented to achieve the desired neck direction and rotational center and the femoral stem must rest against bone that is sufficiently dense to ensure stability of the prosthesis. The femurs used in the experimental measurements were operated by an experienced orthopaedic surgeon. For the FE models it is similarly important that the implant is correctly positioned to produce accurate results. The inner cortical surface in the FE models was used to guide the positioning of the stem inside the femur. Care was taken in the proximal parts that the medial side of the prosthesis was close to the endosteum, letting the prosthesis rest against socalled "stabilising" bone (Aamodt et al., 1999). The gap between the distal end of the femoral stem and the endosteum was very narrow and we assumed that the stem would come in contact with bone in this region during loading. The prosthesis was therefore let to touch the endosteum distally on the lateral side, thereby starting the simulation with initial contact rather than iterating to detect contact during the analyses. Photographs of the femurs were used to reproduce the resection of the femoral neck and the direction of the prosthesis (figure 4.6). The positioning of the prosthesis was then checked against radiographs of the same femurs (figure 4.7).

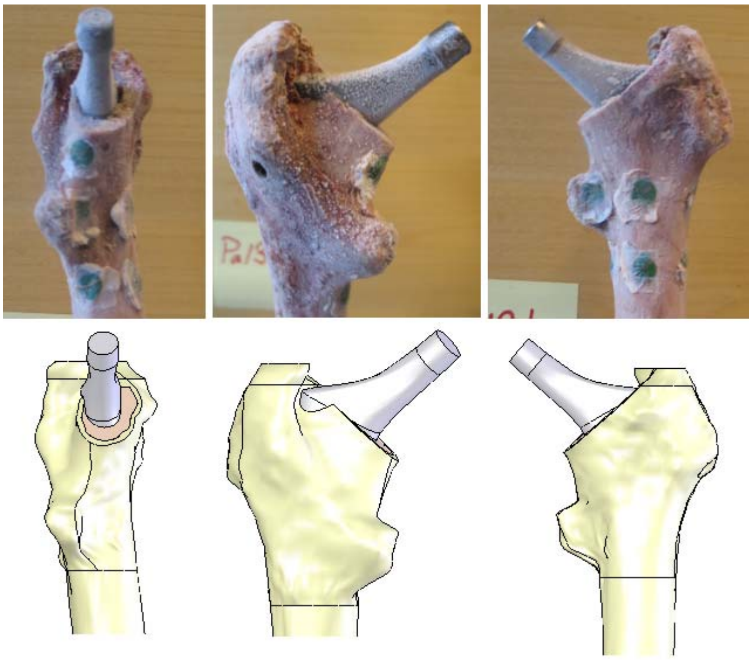

Figure 4.6: Photographs of an implanted femur (13L) from different angles and the 3D model of the same femur.

Modified 10-noded tetrahedral elements (C3D10M) were used for the implanted femurs, since they are known to give better convergence for contact analyses (ABAQUS/Standard version 6.6, 2006). The contact surfaces were defined using finite sliding face-to-face contact elements (Viceconti et al., 2000), with the stem surface as master and bone cavity as slave (figure 4.8).

A wide range of values for the normal contact stiffness are reported in literature, from 600 N/mm (Bernakiewicz and Viceconti, 2002) to 9000 N/mm (Reggiani et al., 2007). In our analyses we found a normal contact stiffness of 1200 N/mm to provide good convergence rates. The coefficient of friction of the interface was set to 0.4. Penalty contact algorithm was used in the analyses of cortical strain (section 4.4). For the analyses of interfacial micromotion, it is important that residual surface penetration is kept low. Augmented Lagrange formulation was therefore used in the micromotion analyses (section 4.5), with a residual penetration tolerance of 0.2%.

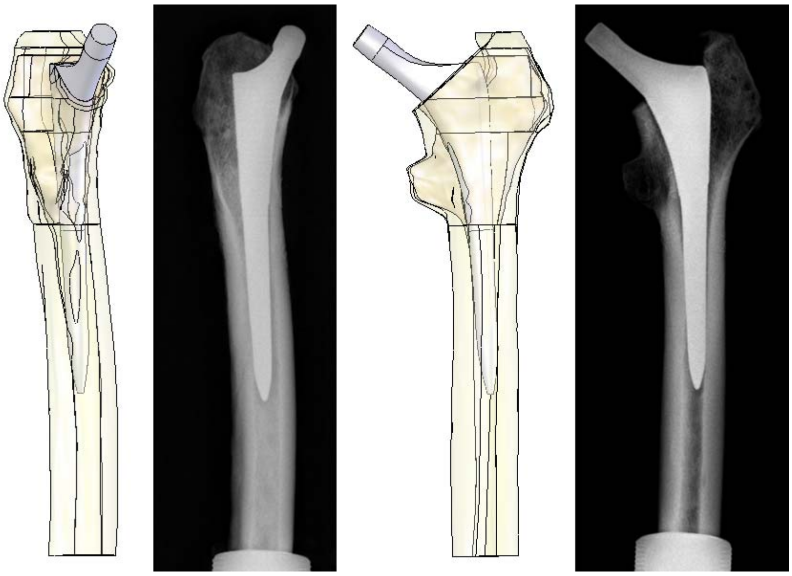

Figure 4.7: The positioning of the stem in femur 13L as used in the FE model compared with the post-operative radiographic images.[1]

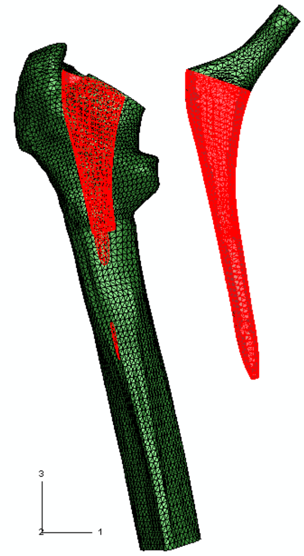

Figure 4.8: The contact surfaces of the prosthesis and bone cavity shown in ABAQUS with face-to-face gap elements.

---

[1] Images showing the positioning of the implants in the other femurs can be found in *Appendix I: Implant positioning – radiographs versus CAD models*.

4.2.4 Modelling the hip simulator

Loading of the hip and femur during gait is a complex combination of muscle and joint contact forces, acting together to provide locomotion and balancing the body. For the purpose of prosthesis evaluation, two simplified load cases are usually considered: single leg stance and stair climbing. Single leg stance is associated with the instance in the gait cycle where all the load is carried by one leg (Martin et al., 1998). Stair climbing has peak contact forces similar to single leg stance (Heller et al., 2001), but produces a higher torsional moment on the implant (Bergmann et al., 2001) and is therefore very important for testing implant stability. When performing mechanical testing on cadaver or composite femurs, the load cases are simplified further to accomodate repeatable test scenarios. The locations of the strain gauges and the principle setup of the hip simulator (Aamodt et al., 2001) used in the present work is shown in figure 4.9. The strain gauge locations on the femur will be used to orient the FE model of the femur and model the complete load setup of the hip simulator.

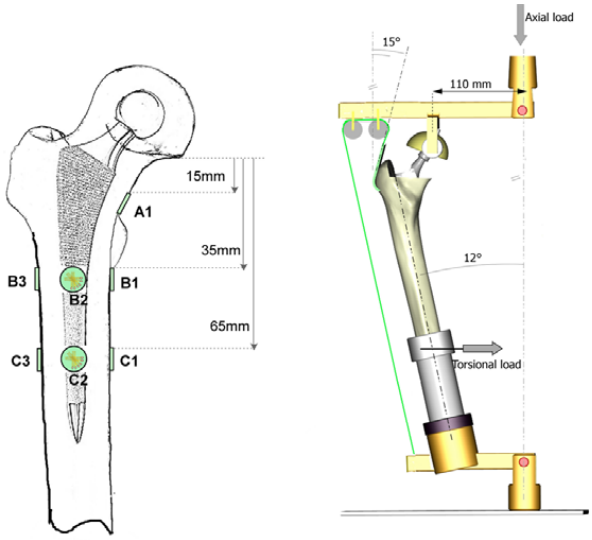

Figure 4.9: The experimental setup used for simulating single leg stance and stairclimbing. Single leg stance is simulated using a vertical load representing the body weight on the load fixture, while stairclmbing is simulated by applying an additional torque distally on the femur.

The horisontal, proximal lever arm in the hip simulator simulates one half of the pelvis, where the applied axial load simulates the body weight along the center axis of the body. The femur was oriented 12° in adduction and the distance between the loading point and the acetabular cup held constant at 110mm. A pulley system was used to simulate the forces in the ilio-tibial band and abductor muscles. The pulleys were adjusted so the abductor angle was 15° and the ilio-tibial band ran along the bone without touching. For practical reasons, the distance between the pulleys was set to 40mm during testing. The distal steel cylinder of the femur was allowed rotate about its own axis. The load fixture allowed vertical displacement and rotation about the y-axis in the load point, and hinged distally, allowing rotation about the y-axis.

The experimental setup of the hip simulator complicates the calculation of the loads and makes it difficult to apply loads and boundary conditions directly on the femur FE model. Instead, the hip simulator was modelled using structural beam and connector elements, thereby allowing a full simulation of the test scenario. The first task is to adjust the orientation of the femur. The node coordinates of the FE model created in COSMOSWorks, are given according to the orientation of the femur during CT scanning. The node coordinates must therefore be transformed, to achieve the correct orientation. The transformation matrix calculated in two steps: first, redefining the origin and aligning the coordinate system according to landmarks on the femur, and secondly, orienting the femur 12° in adduction. For each femur, we have defined the rotational center of the femoral head and different node sets representing contact surface of the femoral head, the distal cut level of the femur, attachment of the trochanter strap and the strain gauges on the femur (figure 4.1).

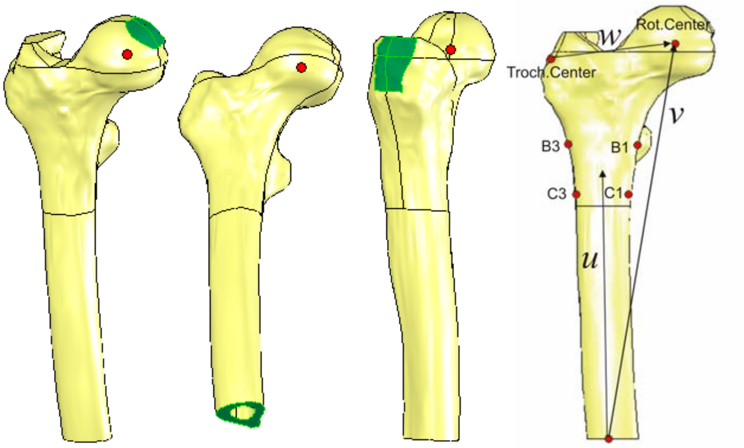

Figure 4.10: The predefined areas where the loads are transferred to the femur are shown in green. The three vectors *u, v* and *w* are used to determine the orientation of the femur. The vectors are calculated from the points shown in red.

The orientation of the femurs was adjusted as follows:

1. Origin: defined at the center of the distal cut-level of the femur.
2. e_z: the direction of the vector, u, from the origin to the midpoint between strain gauges B1, B3, C1 and C3:

$$e_z = \frac{u}{|u|} \tag{4.2}$$

3. e_y: defined by cross the product of the vector u and the vector v, between the origin and the rotational center of the femoral head:

$$e_y = \frac{u \times v}{|u \times v|} \tag{4.3}$$

4. e_x pointing in medial direction:

$$e_x = e_y \times e_z \tag{4.4}$$

$$e_x \bullet w < 0 \Rightarrow e_x = -e_x \text{ and } e_y = -e_y \tag{4.5}$$

These four steps provide the directions of the femur, defining the z-direction along the axis of the femoral shaft, x-direction pointing in the medial direction and the y-direction pointing in the anterior and posterior direction for left and right femurs, respectively. The adduction angle is achieved by additionally rotating the node coordinates by an angle 12° about the y-axis. The new node coordinates can then be calculated:

$$\begin{bmatrix} | \\ Coords_{new} \\ | \end{bmatrix} = \begin{bmatrix} \cos 12^\circ & 0 & -\sin 12^\circ \\ 0 & 1 & 0 \\ \sin 12^\circ & 0 & \cos 12^\circ \end{bmatrix} \begin{bmatrix} - & e_x & - \\ - & e_y & - \\ - & e_z & - \end{bmatrix} \left(\begin{bmatrix} | \\ Coords_{old} \\ | \end{bmatrix} - Origin \right) \quad (4.6)$$

Having adjusted the orientation of the femur, we can start modelling the hip simulator using structural beam (B31) and connector (CONN3D2) elements. The points E, F and G in figure 4.11 are the rotational center of the femoral head, midpoint of the trochanter area and midpoint of the distal femur, respectively. The horisontal bar ABCD is modelled using beam elements along the x-direction 50mm above E. Point B is situated directly above E, and A at a distance 110mm from B. The positions of point C and D were set according to the settings used during the experimental measurements.

Points E, F and G were connected to the caput, trochanter and distal end of the femur using *beam* connector elements. A *join* connector was used between points B and E, thereby allowing the femur to rotate freely in E. The trochanter/ilio-tibial band was modelled with *slipring* connectors which utilize material flow as a degree of freedom, thus simulating the pulley system used in the experimental setup. The distance between G and J was set to 25 cm with point H in the midpoint. A combined *join* and *revolute* connector was used between H and J to allow the femur to rotate about its longitudinal axis. The distal bar IJK was modelled using beam elements in the x-direction. The point K was situated directly underneath the load point A, and point I 10 cm from point K. In point A, only rotation about the y-axis and vertical translation was allowed. In point K, only rotation about the y-axis was allowed. Material flow of the slipring connectors was constrained in points F and I.

We now have a complete FE model of the hip simulator used in the experiments. Thus, single leg stance is simulated by applying a load in point A, and stairclimbing by applying an additional torque about the femoral axis in point H.

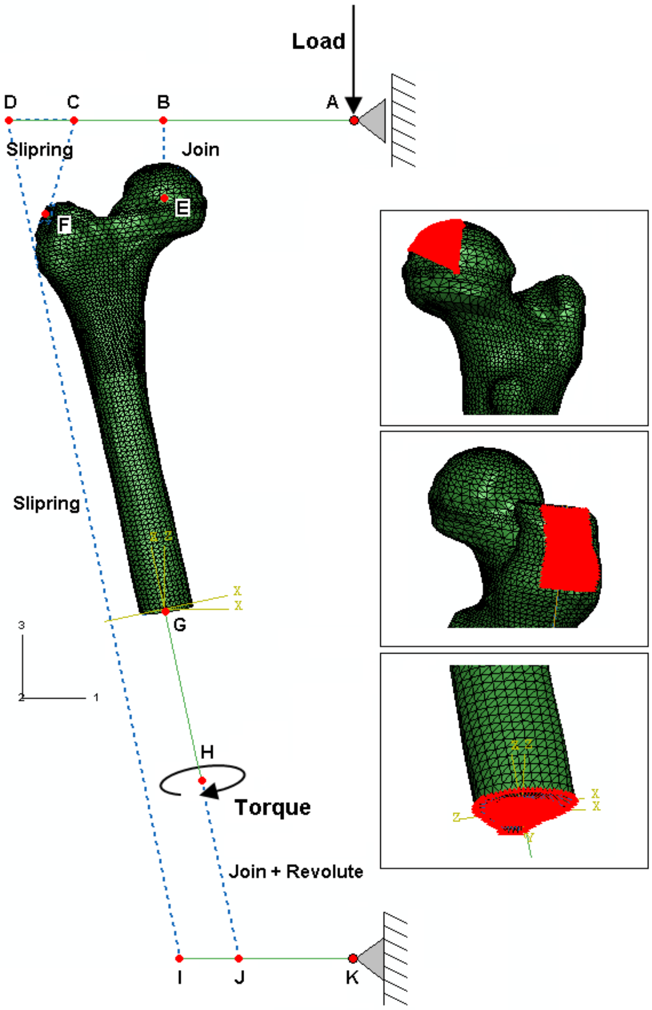

Figure 4.11: The complete FE model of the femur with load jig. Different types connector elements (blue dashed lines) are used to simulate the boundary conditions of the femur; a *join* connector simulates ball joint of the femoral head, *slipring* elements simulate the pulley system and a *join+revolute* element allows the femur to rotate around its axis.

The setup described above was used in the measurements of cortical strain. During measurement of implant micromotion, the ilio-tibial band was omitted as it interfered with the measuring equipment. In the FE analyses of micromotion the *slipring* elements between C, D and I were therefore removed, and material flow constrained in points C and F. Thus, only the trochanter strap simulated abductor forces during micromotion. If the pulleys in point C and D are positioned at distances 163 and 203 mm from A, we can calculate the forces acting on the femur during single leg stance. For the load setup with the ilio-tibial band, the caput and trochanter forces are 251% and 75% relative to the vertical load. With only the trochanter strap, the caput and trochanter forces are 308% and 208% relative to the vertical load. Studies measuring caput loads in implanted hip prostheses, have reported loads of approximately 250% relative to the body weight during slow walking and single leg stance (Bergmann et al., 1993; Bergmann et al., 2001). This means that for the load setup with the ilio-tibial band, a vertical load of 600 N produces a caput load representative of a person weighing 60 kg. With only the trochanter strap, a vertical load of 600 N produces a caput load representative of a person weighing 74 kg.

4.3 Density-stiffness relationship of femoral bone

In the preceding chapter we have described how to link the CT attenuation values to bone mineral density (Chapter 2), how to retrieve the femoral geometry from the CT images and build the subject specific FE models (section 4.2), but we have still not determined which material model to enter into our FE models. It is well known that the Young's modulus of bone depends on its density and the matter has been subject to extensive research (Currey, 1969; Carter and Hayes, 1977; Schaffler and Burr, 1988; Rice et al., 1988; Rho et al., 1995; Wirtz et al., 2000; Keller, 1994; Morgan et al., 2003). Bone tissue is a non-homogenous orthotropic material, where mechanical properties vary at different locations depending on the material density, trabecular architecture and cortical microstructure. It has been found that for FE modelling of whole bones, realistic modelling of the non-homogeneity of bone is very important, while the orthotropic properties play a minor role (Baca et al., 2008). Bone also contain fluids in the form of water, blood and fat (marrow) giving it viscoelastic properties (Carter and Hayes, 1977). Strain rates in bone during walking and running are in the range 0.001-0.01 s^{-1} (Lanyon et al., 1975), but may increase to 0.1 -1 s^{-1} for impact loads (Carter and Hayes, 1977). In experimental in vitro studies using whole bones, loading rates are usually kept low and viscous properties in bone are therefore generally ignored. Despite the vast amount of studies on the subject, there is still no agreement on exactly how the density and stiffness of bone is related (Helgason et al., 2008).

Keller (1994) performed an extensive study on the mechanical properties of bone, and found that the relationship between compressive stiffness and mineral density could be described with one power function for both cancellous and cortical bone. However, FE studies employing this power function have found it to overestimate cortical strain by 50% to 90% (Schileo et al., 2007; Taddei et al., 2007; Helgason et al., 2007; Austman et al., 2008). Keyak et al (1998) introduced a density-stiffness relationship with separate power functions between density and stiffness for cancellous (Keyak et al., 1994) and cortical bone (Keller, 1994). Bessho et al. (2006) found this density-stiffness relationship to produce very accurate predictions of cortical strain.

In the present study, we will test two density-stiffness relationships in subject specific FE models of intact femurs. The first relationship is the one introduced by Keyak et al. (1998). The second relationship is a modified version (Verhulp et al., 2006), where the stiffness of cortical bone has been upscaled. Results from the FE analyses were compared with strain gauge measurements on the femurs.

4.3.1 Material and Methods

Strain gauge measurements on four cadaver femurs collected from three individuals were used in the prestudy. The femurs were tested in a load jig (figure 4.9) simulating the joint and muscle forces during single leg stance and stairclimbing. A vertical load was applied to the load jig to simulate the joint and muscle forces on the femur during single leg stance, followed by an additional torsional load distally to simulate stairclimbing. Two load levels were used: 600N and 900N vertical load, and 10Nm and 15 Nm torque.

The femurs were CT scanned at 140 kV, 150 effective mAs and B50f convolution kernel, with a pixel spacing of approximately 0.35 and 0.7 mm slice distance. The CT scans were calibrated as outlined in Chapter 2, and the pixel values converted into equivalents of bone mineral density. Inner and outer contours were extracted from the CT scans and used to reconstruct the geometry of each femur. Second order tetrahedral elements with a global element size of 3 mm were used in the FE models. Mineral density of each element was calculated from the CT scans and material properties assigned to the elements accordingly (Zannoni et al., 1998). Two material models were examined in the FE models.

The first material model was introduced by Keyak et al (1998) and is based on experimental measurements on cancellous (Keyak et al., 1994) and cortical bone (Keller, 1994):

$$E = 33900 \cdot \rho_{min}^{2.2} \text{ [MPa], for } \rho_{min} \leq 0.27 \text{ [g/cm}^3\text{]} \tag{4.7}$$

$$E = 5307 \cdot \rho_{min} + 469 \text{ [MPa], for } 0.27 < \rho_{min} < 0.60 \text{ [g/cm}^3\text{]} \tag{4.8}$$

$$E = 10200 \cdot \rho_{min}^{2.01} \text{ [MPa], for } \rho_{min} \geq 0.60 \text{ [g/cm}^3\text{]} \tag{4.9}$$

Equation (4.9) gives a Young's modulus of 14.7 GPa for a mineral density of 1.2 g/cm^3 (ρ_{app}=2.0 g/cm^3). This is quite low compared to other studies which generally report the Young's modulus of cortical bone to be 20-25 GPa for apparent densities of 1.7-1.9 g/cm^3 (Schaffler and Burr, 1988; Taylor et al., 2002; Rho et al., 1995; Broz et al., 1995; Kaneko et al., 2003; Hellmich and Ulm, 2002). A modified version of the first material model was therefore included in the present study. In the modified version, the Young's modulus of cortical has been upscaled to correspond with 22.5 GPa (Verhulp et al., 2006):

$$E = 33900 \cdot \rho_{min}^{2.2} \text{ [MPa], for } \rho_{min} \leq 0.27 \text{ [g/cm}^3\text{]} \tag{4.10}$$

$$E = 11164 \cdot \rho_{min} - 1112 \text{ [MPa], for } 0.27 < \rho_{min} < 0.60 \text{ [g/cm}^3\text{]} \tag{4.11}$$

$$E = 15597 \cdot \rho_{min}^{2.01} \text{ [MPa], for } \rho_{min} \geq 0.60 \text{ [g/cm}^3\text{]} \tag{4.12}$$

The two material models are shown in figure 4.12, together with the density-stiffness relationship used by Schileo et al. (2007). The material was considered as isotropic and with a Poisson ratio of 0.3.

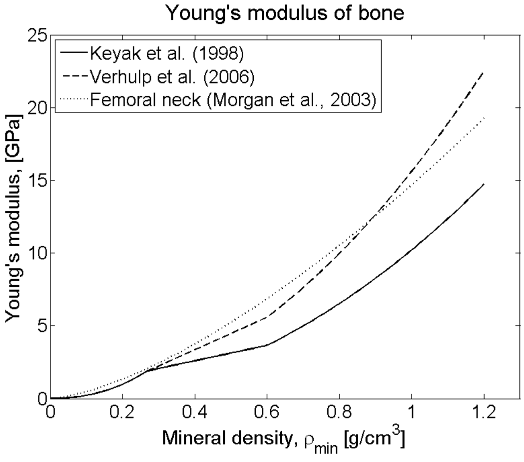

Figure 4.12: Density-stiffness functions for bone used in the present study (Keyak et al., 1998; Verhulp et al., 2006) and the function for cancellous bone in the femoral neck (Morgan et al., 2003) employed by Schileo et al. (2007).

4.3.2 Results

The principal surface strains[2] from the FE analyses are compared with strain gauge measurements in figure 4.13. Summaries of the results for the FE models using the density-stiffness relationship of Keyak et al. (1998) and Verhulp et al. (2006) are given in table 4.1. The root mean square errors (RMSE) and peak errors are given as absolute values ($\mu\varepsilon$) and as percentage of the maximum measured value.

Excellent correlation ($R^2 > 0.90$) was found for all femurs except 16L. Adopting a 95% confidence interval we find the slopes (β_1) for all femurs to be significantly greater than 1 when employing equations (4.7)-(4.9). For the pooled results of all femurs, the y-intercept (β_0) is significantly different from 0. Employing the modified material model of equations (4.10)-(4.12) improved the accuracy of the strain predictions considerably. The slope and y-intercept calculated for the femurs pooled together are still significantly different from 1 and 0, but they are much closer to the ideal values. The error indicators are also reduced. The RMSE is reduced by half from 20% to 10%. Femur 16L stands out with poor results and causes a high peak error for the pooled data of both material

---

[2] See *Appendix II: Post-processing FE and experimental strain*

models. For the three remaining femurs (11R, 13L and 13R) the peak error is nearly halved when adopting the modified material model.

Table 4.1: Correlation between strain gauge measurements and FE models using the two density-stiffness relationsships. $\mu\varepsilon_{FE} = \beta_1 \cdot \mu\varepsilon_{Exp.} + \beta_0$

Material	**β_1 (95%CI)**	**β_0 (95%CI)**	**R^2**	**RMSE**	**Peak Error**
Keyak et al. (1998):					
11R	1.39 *(1.34, 1.45)*	91 *(22,161)*	0.98	561(20%)	1395 (51%)
13L	1.41 *(1.33, 1.48)*	182 *(113, 251)*	0.96	464 (23%)	1096 (55%)
13R	1.49 *(1.40, 1.59)*	163 *(86, 240)*	0.95	499 (29%)	1180 (68%)
16L	1.33 *(1.18, 1.47)*	-11 *(-203, 181)*	0.85	819 (27%)	2596 (87%)
Pooled	1.39 *(1.33, 1.44)*	105 *(48,162)*	0.93	602 (20%)	2596 (87%)
Verhulp et al. (2006):					
11R	0.93 *(0.89, 0.97)*	60 *(13, 107)*	0.98	218 (8%)	545 (20%)
13L	0.97 *(0.91, 1.02)*	131 *(82,180)*	0.96	226 (11%)	723 (36%)
13R	1.02 *(0.96, 1.08)*	120 *(70,170)*	0.95	218 (13%)	461 (27%)
16L	0.86 *(0.77, 0.96)*	-9 *(-134,115)*	0.86	488 (16%)	1608 (54%)
Pooled	0.92 *(0.89, 0.96)*	74 *(36, 112)*	0.93	308 (10%)	1608 (54%)

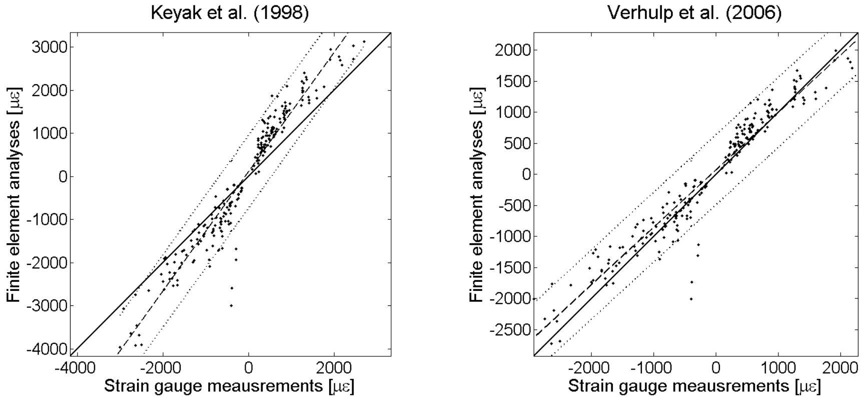

Figure 4.13: The strains predicted using the two density-stiffness relationships. The solid line demarks the one-to-one relationship, the dashed line the regression line and the dotted lines the 95% confidence intervals. The plots show that the density-stiffness relationship of Keyak et al. (1998) overestimates cortical strain (left). The modified relationship (Verhulp et al., 2006) improves the accuracy of the FE models (right).

4.3.3 Discussion

The purpose of the present study was to examine two density-stiffness relationships for use in subject specific FE models; the relationship introduced by Keyak et al. (1998), and a modified version with upscaled stiffness for cortical bone (Verhulp et al., 2006).

The FE models showed good correlation between measured and predicted strain for both density-stiffness relationships. The correlation was considerably poorer for femur

16L (R^2=0.85) than the rest of the femurs (R^2>0.90). In the FE models we found the density-stiffness relationship of equations (4.7)-(4.9) to overestimate cortical strain by approximately 40%. The modified density-stiffness relationship in equations (4.10)-(4.12) improved the accuracy of strain predictions considerably. The pooled FE results of the modified material model produced a regression line with a slope of 0.92 and y-intercept 86.5. Although the slope and y-intercept still are significantly different from 1 and y-intercept different from 0, they show a considerable improvement. All error indicators (RMSE and peak error) were reduced when employing the modified material model.

Early density-stiffness relationships for bone assumed that the tissue of cortical bone and the trabecular tissue in cancellous bone were the same, and that the relationship could be expressed by one function for the whole range of bone densities (Carter and Hayes, 1977; Keller, 1994). However, it has been shown that the mechanical properties of trabecular tissue are significantly different from cortical tissue (Rho et al., 1993; Rice et al., 1988). Keyak et al. (1998) introduced a stiffness-density relationship where bone at the lower end of the density range ($\rho_{min} \leq 0.27$ g/cm^3) was assumed to be cancellous and assigned material properties derived from tibial cancellous bone (Keyak et al., 1994). Similarly, bone in the higher end of the density range ($\rho_{min} \geq 0.6$ g/cm^3) was assumed cortical and assigned properties derived from femoral cortical bone (Keller, 1994). This relationship has been used in FE studies concerning predictions of femoral fractures (Keyak et al., 1998; Keyak and Rossi, 2000; Bessho et al., 2006). Bessho et al. (2006) compared FE analyses with strain gauge measurements, and found equations (4.7)-(4.9) to produce accurate predictions of strain. However, several studies using subject specific FE models of whole bone have generally found the density-stiffness relationships of Keller et al. (1990) to overestimate strain by 50% to 90% (Schileo et al., 2007; Taddei et al., 2007; Helgason et al., 2007; Austman et al., 2008). Our results seem to confirm that the elasticities calculated for cortical bone by equation (4.9) are too low.

Schileo et al. (2007) employed a density-stiffness relationship derived from cancellous bone from the femoral neck (Morgan et al., 2003) and found it to give accurate strain predictions in whole femurs. The material properties of the femoral neck were later used by the same group to predict femoral fractures (Schileo et al., 2008). The neck area was therefore the primary region of interest, and the chosen density-stiffness relationship very relevant. In our study, however, we have analysed cortical strain in intact femurs, with the intention of developing FE models for preclinical evaluation of femoral stems. In that case, the neck is resected and most of the cancellous bone is removed by rasping. Also, we did not find it appropriate to employ a density-stiffness relationship derived for one particular type of cancellous bone on all types of bone tissue, both cancellous and cortical. We therefore did not consider using the density-stiffness relationship of the femoral neck employed by Schileo et al. (2007). However, figure 4.12 shows that the material model used by Schileo et al. (2007) produces stiffnesses quite close to the modified material model used in the present study. The results of the present study and the results of Schileo et al. (2007) therefore seem to mutually confirm each other. In the future work, we will adopt the modified density-stiffness relationship in equations (4.10)-(4.12) for our subject specific FE models.

4.4 Subject specific finite element analysis of stress shielding around a cementless femoral stem[3]

Abstract

Background: Stress shielding around a femoral stem is usually assessed experimentally using composite or human cadaver femurs. In the present study we have explored the feasibility of using subject specific finite element models to determine stress shielding in operated femurs.

Methods: Cortical strain was measured experimentally on seven human cadaver femurs, intact and implanted with a straight cementless prosthesis. Two load configurations were considered: single leg stance and stair climbing. Subject specific finite element models derived from computed tomography of the same femurs were analysed intact and with an implant. Principal cortical strain was used to validate the finite element models. Stress shielding was defined as the change in equivalent (von Mises) strain between pre- and postoperative femurs.

Findings: Cortical strain predicted by the finite element analyses showed to be close to unity with the experimental observations for both intact (R^2=0.94, slope=0.99), operated femurs (R^2=0.86, slope=0.86) and stress shielding (R^2=0.70, slope=0.90). In the proximal calcar area, the region most prone to periprosthetic remodelling, the finite element models were found to successfully reproduce the stress shielding observed experimentally.

Interpretation: The study shows that subject specific finite element models manage to describe the stress shielding pattern measured in vitro in the different femurs. Finite element models based on actual human femurs (cadaver and/or patient) could thus be a useful tool in the pre-clinical evaluation of new implants.

4.4.1 Introduction

Bone resorption in the proximal femur due to stress shielding is a known effect of femoral implants. The implants are much stiffer than the bone, and thus reduce the mechanical stimulus to the surrounding bone causing bone resorption. For femoral

---

[3] Pettersen, S. H., Wik, T. S., Skallerud, B., (2009). Subject specific finite element analysis of stress shielding around a cementless femoral stem. Clin.Biomech.(Bristol., Avon.) 24, 196-202.

stems severe bone loss is especially prevalent in the proximal calcar region (Engh et al., 1992; Kroger et al., 1998). It has been difficult to prove any direct adverse clinical effects of stress shielding on the revision rate of the implants (Harris, 1992; Bugbee et al., 1997; Engh, Jr. et al., 2003). Severe bone loss is therefore mainly a problem for revision surgery, as it makes it difficult to safely remove the old prosthesis and provide proximal stability for the new prosthesis (Kerner et al., 1999; Glassman et al., 2006). It is therefore desirable that the implant maintains the physiological loading of the bone in order to limit the degree of bone resorption.

The stress shielding effect of a prosthetic design is usually evaluated by in vitro testing using human cadaver bones. However, the availability of cadaver bones is limited and the preparation of the bones is cumbersome. Other methods of testing have therefore been proposed, like using bone replicas and finite element (FE) analysis. Composite femur replicas are made to represent average adult femurs with mechanical properties close to human bone (Cristofolini et al., 1996). This eliminates the problem of geometric and mechanical variability between femurs. In this also lies one of the problems with using composite femurs, as the prosthetic design may become optimized for a particular femoral geometry.

FE modelling allows implants to be tested in a wide range of femoral geometries and has been used in several biomechanical studies investigating both intact bones (Keyak et al., 1998; Lengsfeld et al., 1998; Helgason et al., 2007; Schileo et al., 2007; Taddei et al., 2007) and with orthopaedic implants (Rohlmann et al., 1983; Rubin et al., 1993; McNamara et al., 1997; Viceconti et al., 2001; Stolk et al., 2002a; Completo et al., 2007). FE models can also be used to simulate adaptive remodelling to show how the prosthesis will perform on a longer term (Rietbergen et al., 1993; Kerner et al., 1999).

Subject specific FE models with geometry and material properties derived from computed tomography (CT) have been described in several studies (Keyak et al., 1998; Lengsfeld et al., 1998; Helgason et al., 2007; Schileo et al., 2007; Taddei et al., 2007). To the best knowledge of the authors, there has not been published any studies validating the use of human subject specific FE models for evaluating the stress shielding around a femoral stem. In the present study we will use subject specific FE models of human cadaver femurs to predict the cortical strain before and after implantation of cementless femoral stem. The results will be validated by experimental strain gauge measurements on the same cadaver femurs.

4.4.2 Material and Methods

Seven human femurs were collected from 3 males and 4 females aged 49-74 years (average 63 years). The study was approved by the regional medical research ethics committee. The femurs were examined by DEXA and plain radiography and excluded if signs of osteoporosis or other skeletal pathologies were found. The femurs were CT scanned (Siemens Somatom Sensation 64, Erlangen, Germany) at 140 kV, 300 mAs and B50f reconstruction kernel with a pixel spacing of approximately 0.35 mm, 0.75 mm slice thickness and 0.7 mm slice distance. Bags of water were placed around the femurs during CT scanning to reduce beam hardening. A calibration phantom consisting of different mixtures of calcium carbonate and polymer (PMMA) was used to convert the CT pixel values to equivalents of bone mineral density[4].

The femurs were stored at -20°C, thawed at room temperature and prepared for testing as decribed by Aamodt et al. (2001). The condyles were resected and the femur cemented into a steel cylinder 25 cm distally of the upper tip of the greater trochanter.
Triaxial strain rosettes were glued to the femurs on the medial, lateral and anterior sides of the femur as shown in figure 4.14 (left).

---

[4] See *Chapter 2: Relating CT gray-scale values to bone density.*

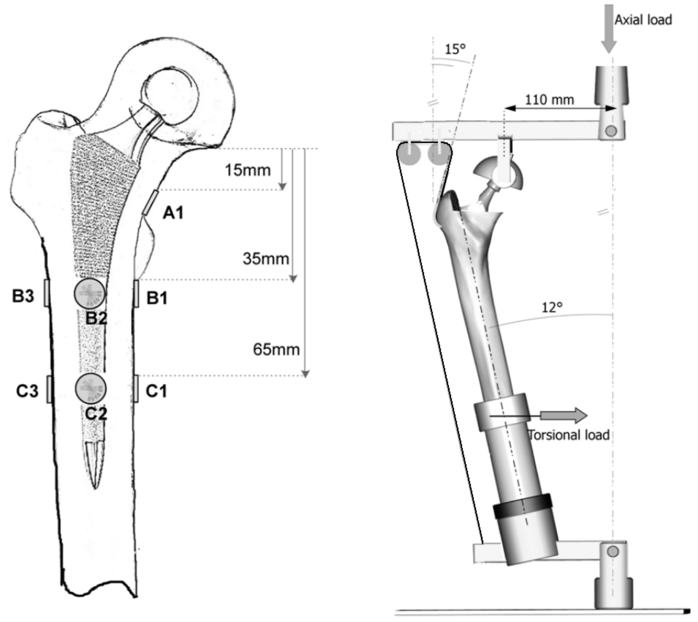

Figure 4.14: Placement of the strain gauges on the femur (left) and the experimental setup used to simulate the forces acting on the femur under single leg stance and stair climbing (right).

In vitro testing of the femurs was performed using a load jig shown in figure 4.14 (right) simulating the joint and muscle forces acting on the femur. The femur was tilted 12° in valgus and the distal steel cylinder constrained, allowing it only to rotate around its own axis. The load jig consisted of a lever arm acting as the pelvis with an acetabular cup transferring load to the femoral head, and a pulley system distributing the load between the ilio-tibial band and the abductor muscles on the greater trochanter. The importance of the ilio-tibial band and how its forces should be applied in a FE model is an issue of debate (Stolk et al., 2001). In our load jig, the ilio-tibial band does not act on the femur itself, but was included as it contributes together with abductor muscles in balancing the pelvis. The pulleys were positioned at a distance of 40 mm from each other and adjusted so that the trochanter band acted at an angle of 15° with the vertical axis. Two distinct load configurations were simulated in the load jig: single leg stance and stair climbing. A vertical load was applied to the end of the lever arm using a material testing machine (MTS 858 Minibionix II, Eden Prairie, USA) simulating the force of the body weight during single leg stance. An additional torque was applied to the femur distally to simulate the load conditions during stair climbing. This loading setup gives resultant joint and ilio-tibial/trochanter loads of approximately 250% and 75% relative to the vertical load both for single leg stance and stair climbing. This corresponds with telemetric measurements of femoral joint forces in patients (Bergmann et al., 1993; Bergmann et al., 2001). Two load levels were used: with a 600 N vertical load and 10 Nm torque, and a maximum at 900 N vertical load and 15 Nm torque. For two of the female femurs (18R and 19R) the maximum load level was set to 800 N and 13.5 Nm.

The femurs were tested intact and implanted with a straight cementless prosthesis (DePuy Summit™, Leeds, UK). The prostheses were implanted into the femurs by an experienced orthopaedic surgeon.

FE models

Inner and outer contours of cortical bone were extracted from the CT scans based on gray-scale transition values using in-house written code (MATLAB 7.1, The Mathworks, Natick, USA), and revised manually. The contours were lofted together to create a 3D model of the femur using SolidWorks 2005 (Solidworks Corporation, Concord, USA). Cortical and cancellous bone was modelled as two separate sections, and the medullary canal below the lesser trochanter modelled as empty. The endosteal surface of the cortical bone could this way be used to position the prosthesis in the femur. The 3D models were meshed using 10-noded tetrahedral elements with a global size of 3 mm (CosmosWorks 2005, Solidworks Corporation, Concord, USA). Material properties at the location of each elements were derived from the CT scans and mapped to the FE model (Zannoni et al., 1998). The material properties of bone were assumed linear elastic and isotropic (Baca et al., 2008). In our study we have used the density-stiffness relationship introduced by Verhulp et al. (2006):

$$E = 33900 \cdot \rho_{min}^{2.2} \text{ [MPa], for } \rho_{min} \leq 0.27 \text{ [g/cm}^3\text{]} \tag{4.13}$$

$$E = 11164 \cdot \rho_{min} - 1112 \text{ [MPa], for } 0.27 < \rho_{min} < 0.60 \text{ [g/cm}^3\text{]} \tag{4.14}$$

$$E = 15597 \cdot \rho_{min}^{2.01} \text{ [MPa], for } \rho_{min} \geq 0.60 \text{ [g/cm}^3\text{]} \tag{4.15}$$

The same density-stiffness relationship was used on both the cancellous and cortical section. Material assignment and preparation of the mesh was performed using scripts written in MATLAB 7.1. The FE models were exported to ABAQUS/Standard 6.7 (Simulia, Providence, USA).

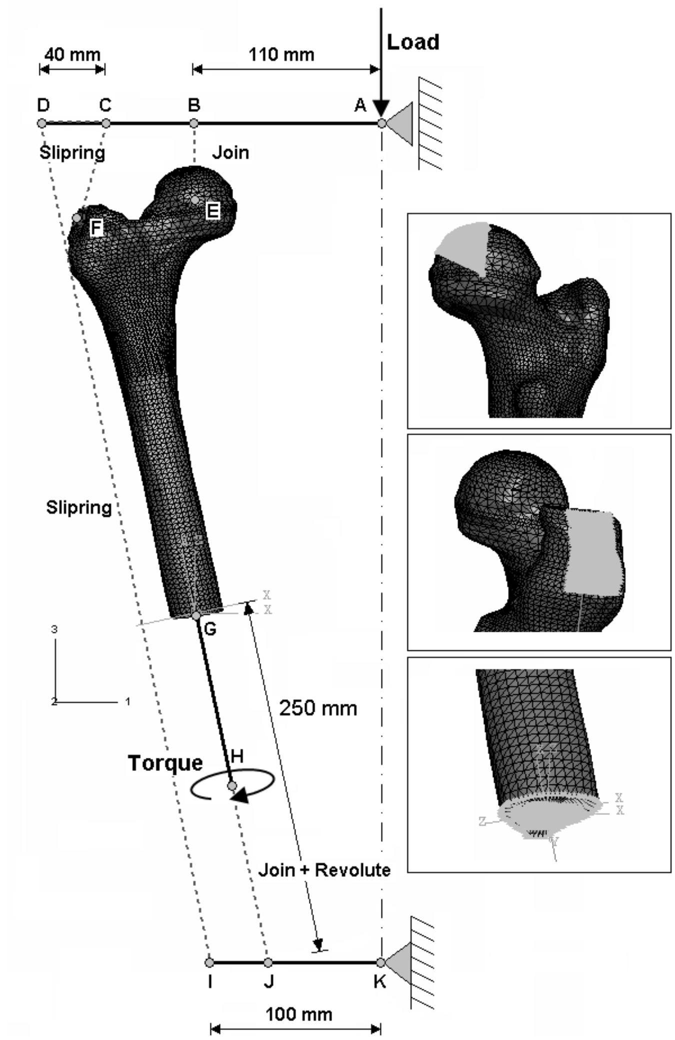

Figure 4.15: The load jig as simulated in the FE analyses. The beam elements are shown as solid lines and connector elements (join, slipring and join+revolute) as dashed lines. On the right, the beam connector elements (light gray) connecting points E, F and G to the surface nodes of the femoral head, greater trochanter and the distal end, respectively.

The node coordinates of the FE model were transformed to achieve the orientation of the femur used in the in vitro testing - with the x-direction pointing medially, the z-direction pointing upwards and the femoral shaft tilted 12° in valgus. In order to replicate the forces acting on the femur during the in vitro testing, the load jig was modelled using structural elements as shown in figure 4.15. The upper and lower lever arms were modelled using beam elements along the x-direction (ABCD and IJK). The three points E, F and G, were defined by the rotational center of the femoral head, the midpoint on the greater trochanter and the midpoint of the distal end of the femur, respectively. The boundary conditions of the femur were simulated using connector elements available in the ABAQUS software. The *join* connector simulates the ball joint of the load jig, and the *join+revolute* connector the distal cylinder. *Slipring* elements utilize material flow through the nodes as a degree of freedom, and were used between F, C, D and I to simulate the pulley system. Material flow of the *slipring* connectors was constrained in points F and I. In point K only rotation about the y-direction was allowed, and in point A only displacement in the z-direction and rotation about the y-direction were allowed. The complete setup with structural and connector elements thus mimicked the boundary conditions of the load jig. Single leg stance was simulated by applying a vertical load in point A, and stair climbing by applying an additional torque in point H.

All analyses were run using the nonlinear solver in ABAQUS/Standard 6.7 due to nonlinearities from the boundary conditions of the load jig and the implant-bone interface.

FE strain results from the elements were extrapolated to the surface nodes representing the strain gauge positions. The surface normal was determined at each strain gauge, and used to transform the FE strain tensors expressed in the global coordinate system to the local coordinate systems of the strain gauges. The predicted surface strains from the FE analyses could thus be compared directly with the experimental strain measurements[5].

---

[5] See *Appendix II: Post-processing FE and experimental strain*

Prosthesis and interfacial surface conditions

The geometry of the Summit prosthesis was provided by the manufacturer (DePuy, Leeds, UK). The prosthesis is porous coated with a slightly ribbed surface to promote fixation through osseointegration. This surface was smoothened in our FE models to simplify contact analysis. The endosteal surface in the 3D model was used to position the stem in the medullary canal so that penetration into cortical bone was minimal. The neck resection, anteversion angle and positioning of the visible part of the prosthesis was copied in the FE model based on postoperative photographs of the femur. Radiographs were used to check the stem positioning inside the femurs. The intersecting bone was then removed from the model. Contact between bone and stem was considered in the proximal coating area of the prosthesis, and between the distal tip of the stem and the lateral side of the endosteal surface in the medullary canal. No initial press-fit of the stem was considered in the FE models. Operated femurs were modelled using modified 10-noded tetrahedral element (C3D10M) as they are more suitable for contact analyses than the regular elements (C3D10) which were used for the intact femurs. The contact surface was modelled using finite sliding face-to-face contact elements with the prosthetic contact surface defined as the master surface and the cavity surface as the slave surface. The frictional coefficient was set to 0.4 and a normal contact stiffness of 1200 N/mm was employed. A penalty formulation was used for solving the contact interactions. The Young's modulus of the prostheses was set to 200 GPa (cobalt chrome).

Data analysis

The FE models of intact and operated femurs were validated using linear regression for the first and second principal strains. To assess stress shielding at the different locations, the equivalent strain ($\bar{\varepsilon}$) (von Mises strain) was used to sum up the strain conditions in one scalar value, and the strain values of operated femurs were expressed relative to the intact values ($\bar{\varepsilon}_R$).

$$\bar{\varepsilon} = \frac{2}{3} \cdot \sqrt{\varepsilon_1^2 + \varepsilon_2^2 - \varepsilon_1 \cdot \varepsilon_2} \qquad (4.16)$$

$$\bar{\varepsilon}_R = \frac{\bar{\varepsilon}_{operated}}{\bar{\varepsilon}_{intact}} \cdot 100\% \qquad (4.17)$$

The relative change in strain is referred to as stress shielding. A $\bar{\varepsilon}_R$-value of 0% thus represents that the bone is fully stress shielded, while 100% represents that the physiological strains have been maintained.

The data was analysed by linear regression to evaluate the agreement between the predicted FE results and the experimental strain gauge measurements. The agreement between FE results and experimental results could be regarded as perfect if the coefficients of correlation were found to be $R^2=1$, slope $\beta_1=1$ and y-intercept $\beta_0=0$. Principal strains were analysed before and after implantation separately for each femur, and all femurs pooled together. The same was done for the stress shielding effect ($\bar{\varepsilon}_R$). 95% confidence intervals were calculated for the determined values of β_1 and β_0. If the 95% confidence interval of β_1 spanned the value 1, it was regarded as not significantly different from 1, and likewise for β_0 and the value 0.

4.4.3 Results

Principal strains from the FE analyses and the strain gauge measurements for both intact and operated femurs are shown in figure 4.16. Intact femurs yielded a correlation of $R^2=0.94$, slope $\beta_1=0.99$ and y-intercept $\beta_0=108$ microstrain. Operated femurs yielded a correlation of $R^2=0.86$, slope $\beta_1=0.86$ and y-intercept $\beta_0=65$ microstrain. The slope of the intact femurs was not significantly different from 1, but the y-intercept was significantly greater than 0. For the operated femurs, both slope and y-intercept was significantly different from 1 and 0. The stress shielding effect expressed by the relative equivalent strain ($\bar{\varepsilon}_R$) yielded a correlation of $R^2=0.70$ between FE results and experimental data (figure 4.17). The slope was slightly less than 1 and the y-intercept not significantly different from 0. The complete correlation results together with the root mean square errors (RMSE) are given in table 4.2.

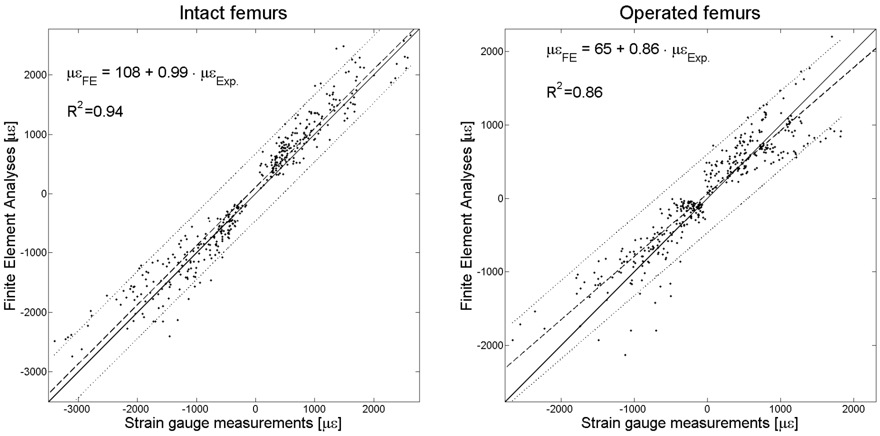

Figure 4.16: Comparison of principal strains for intact (left) and operated (right) femur. The solid line shows the one-to-one line, dashed line the regression line and the dotted lines the 95% confidence interval.

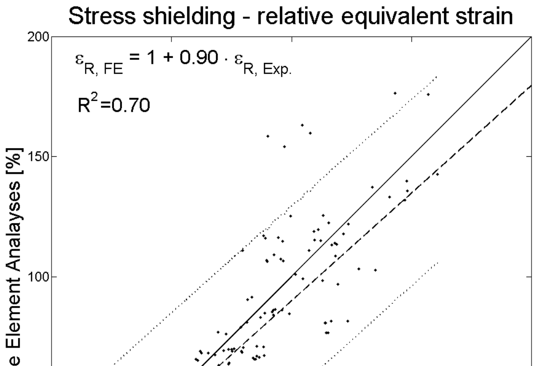

Figure 4.17: Correlation of the relative equivalent strain in the femurs after insertion of the femoral stem. The solid line shows the one-to-one line, dashed line the regression line and the dotted lines the 95% confidence interval.

Table 4.2: Coefficients of correlation for the individual femurs: $\mu\varepsilon_{FE} = \beta_1 \cdot \mu\varepsilon_{Exp.} + \beta_0$. The sex and age of each donor together with the size of the prosthesis are given in the parentheses. L=left, R=right, number identifies specimen.

	n	β_1 *(95%CI)*	β_0 *(95%CI)*	R^2	RMSE
01R (M\60\8)					
Intact [με]	56	1.07 *(1.02-1.12)*	29 *(-13-72)*	0.97	169
operated [με]	56	0.86 *(0.76-0.96)*	70 *(18-121)*	0.84	212
Stress shielding [%]	28	0.73 *(0.53-0.93)*	13 *(-1-27)*	0.69	20
02L (F\74\6)					
intact [με]	56	0.93 *(0.88-0.97)*	93 *(20-166)*	0.97	308
operated [με]	56	0.91 *(0.81-1.02)*	10 *(-101-120)*	0.84	413
Stress shielding [%]	28	1.29 *(0.96-1.62)*	-19 *(-44-6)*	0.71	28
03L (F\61\5)					
intact [με]	56	0.82 *(0.78-0.85)*	96 *(45-147)*	0.98	347
operated [με]	56	0.68 *(0.61-0.75)*	67 *(0-135)*	0.88	404
Stress shielding [%]	28	0.73 *(0.48-0.99)*	14 *(-4-33)*	0.57	21
08L (M\49\4)					
intact [με]	56	0.97 *(0.91-1.02)*	160 *(86-235)*	0.93	319
operated [με]	56	0.94 *(0.87-1.01)*	87 *(33-141)*	0.93	220
Stress shielding [%]	28	0.86 *(0.75-0.97)*	-4 *(-13-6)*	0.91	19
13L (M\74\4)					
intact [με]	56	0.97 *(0.91-1.02)*	131 *(82-180)*	0.96	226
operated [με]	56	0.87 (0.80-0.93)	66 *(19-112)*	0.93	208
Stress shielding [%]	28	0.97 *(0.83-1.11)*	-3 *(-16-11)*	0.89	15
18R (F\59\6)					
intact [με]	56	1.20 *(1.13-1.26)*	98 *(29-167)*	0.97	343
operated [με]	56	0.86 *(0.77-0.94)*	82 *(24-141)*	0.89	251
Stress shielding [%]	28	0.60 *(0.38-0.82)*	14 *(-1-28)*	0.55	20
19R (F\65\5)					
intact [με]	56	1.32 *(1.25-1.38)*	160 *(98-222)*	0.97	388
operated [με]	56	0.98 *(0.86-1.11)*	65 *(-20-150)*	0.82	319
Stress shielding [%]	28	1.04 *(0.65-1.42)*	-14 *(-44-17)*	0.54	25
Summary all femurs					
intact [με]	392	0.99 *(0.97-1.02)*	108 *(79-137)*	0.94	308
operated [με]	392	0.86 *(0.82-0.89)*	65 *(38-92)*	0.86	301
Stress shielding [%]	196	0.90 *(0.81-0.98)*	1 *(-6-7)*	0.70	21

The second principal strain dominates on the medial side ($|\varepsilon_2| > \varepsilon_1$) of the femur and first principal strain on the lateral side ($\varepsilon_1 > |\varepsilon_2|$), indicating compression and tension, respectively. A considerable drop in cortical strain from intact to operated femurs was observed experimentally in strain gauges A1 and B1, while strain gauges B2 and C2 exhibited a slight increase. The additional torque during stair climbing produced slightly higher cortical strains. The difference was more pronounced in the operated femurs, due the bone being twisted around the femoral stem. Thus, the relative equivalent strains were slightly higher for stair climbing than single leg stance, but the general stress shielding patterns in the different femurs were largely the same for the two load cases. Figure 4.18 compares the stress shielding pattern at stair climbing in the different femurs as predicted by FE analyses and observed experimentally. The FE analyses tended to underestimate the degree of stress shielding in strain gauge A1, but generally showed the same stress shielding pattern on the medial and anterior side of the femurs. The FE models significantly overestimated the degree of stress shielding on the lateral side (B3 and C3).

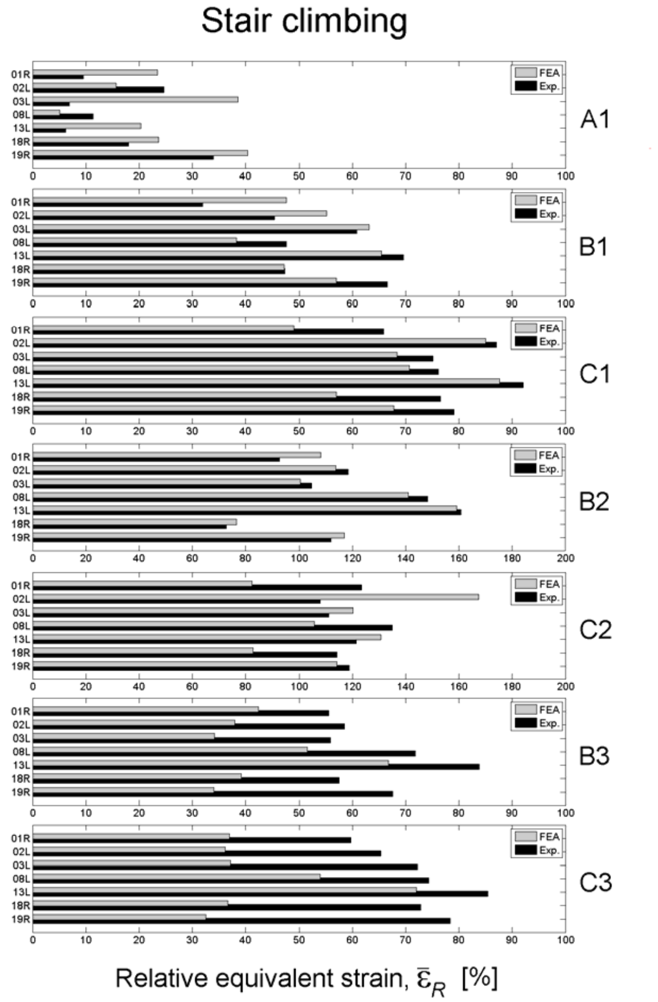

Figure 4.18: Bar diagram comparing the stress shielding effect of the prosthesis at stair climbing (800/900N, 13.5/15Nm) as predicted by the FE analyses and observed experimentally. The x-axis is set to 200% for strain gauges B2 and C2 and to 100% for the rest. L=left, R=right, number identifies specimen.[6]

---

[6] Bar diagram showing stress shielding during single leg stance can be found in *Appendix III: Stress shielding during single leg stance.*

4.4.4 Discussion

The primary aim of this study was to investigate the feasibility of using subject specific FE models to determine stress shielding around cementless femoral stems. FE simulations have been employed in several studies to predict the adaptive remodelling due to stress shielding observed *in vivo* (Rietbergen et al., 1993; Kerner et al., 1999). In the present study we have tried to simulate the experimental test procedure used for *in vitro* pre-clinical evaluation of implants.

The FE results of intact femurs gave very good agreement with the experimental strain measurements, and are close to the results reported by Schileo et al (2007). The operated femurs also produced results in good agreement with the experimental data, but the correlation was somewhat weaker. FE studies of composite femurs with an implant have shown a correlation with experimental measurements (R^2>0.90) superior to our results (McNamara et al., 1997; Viceconti et al., 2001; Stolk et al., 2002a; Completo et al., 2007). However, these studies employed a standardized and simplified femoral geometry with known material properties, while our femurs covered a variation of femoral geometries and had unknown material properties. Regression analyses of the individual femurs gave slopes varying from 0.82 to 1.32 for intact and 0.68 to 0.98 for operated, showing that the FE models overestimated the stiffness of some femurs and underestimated it for others. The three FE models with poorest agreement with the strain gauge measurements, showed both overestimation (18R and 19R) and underestimation (03L) of cortical strain of intact bones. This implies that there was no systematic error in the estimates of bone elasticity. FE analyses of intact and implanted femurs yielded very good results for the three male donors (01R, 08L and 13L) which also were the three largest femurs in the study. Femurs 08L and 13L were implanted with the smallest implant (size 4). These two femurs generally had better results than 01R, where the biggest implant size was used (size 8). It thus seems that both intact and operated subject specific FE models of femurs with a thick cortical wall gave better agreement with the experimental data.

Insertion of a femoral stem changes not only the magnitude of the principal strains, but might also change the principal strain directions. Thus, principal strains before and after operation are not necessarily comparable. Equivalent strain was therefore used instead to express the strain conditions at the strain gauge as one scalar parameter. Similar approaches of simplifying the strain conditions into equivalent strain or octahedral shear strain have been used in earlier biomechanical studies (Mikic and Carter, 1995; Kessler et al., 2006). The relative equivalent strain yielded a correlation of R^2=0.70 between the FE models and the experimental measurements. Table 4.2 shows a varying degree of correlation between the predicted and measured stress shielding for the individual femurs, with values of R^2 ranging between 0.54 and 0.91 and slopes varying between 0.60 and 1.29. However, the bar diagram in figure 5 show that the FE models manage to describe the same stress shielding pattern on the medial and anterior sides of the femurs as observed experimentally. The FE models also manage to reflect some of the variation between the femurs in stress shielding at the different strain gauge locations. Proximally on the medial side (strain gauges A1 and B1), where bone loss due to adaptive remodelling is usually observed (Engh et al., 1992; Kroger et al., 1998), a considerable decrease in cortical strain after operation was seen experimentally and in the FE models. The anterior side of the femur lies in the transition between tension and compression and therefore exhibits little strain. The slight rise in cortical strain observed in B2 and C2 after operation can therefore be ascribed to the wedging of the prosthesis giving an increase in the hoop strain. Only for strain gauges B3 and C3 the FE analyses seem to miss the target and overestimate the degree of stress shielding significantly for all femurs.

A modified version of the material model used by Keyak et al. (1998) was employed in our FE models. In the original version, a density-stiffness relationship found for cortical bone (Keller, 1994) was used for mineral densities greater than 0.6 g/cm^3. This material model for cortical bone has been used in a series of biomechanical studies but, has largely shown to overestimate strain by 50% to 100% (Helgason et al., 2007; Schileo et al., 2007; Taddei et al., 2007). Schileo et al. (2007) extrapolated a density-stiffness relationship for trabecular bone (Morgan et al., 2003) to include densities of cortical bone and found it to better predict femoral strain when used in subject specific FE models. The choice of appropriate material properties for bone tissue is a matter of constant debate. The density-stiffness relationship for bone has been shown to vary at different locations (Morgan et al., 2003) and depends on its microstructural architecture (Stauber et al., 2006). The modified material model (Verhulp et al., 2006) given in equations (4.13)-(4.15), distinguishes between lower density cancellous bone and higher density cortical bone and uses different density-stiffness relationships for these. It differs from the original version (Keyak et al., 1998) in that the Young's modulus of cortical bone (ρ_{min}>0.6 g/cm^3) is upscaled to give 22.5 GPa for fully mineralized bone (ρ_{min}=1.2 g/cm^3). This corresponds with other studies showing the Young's modulus of fully mineralized cortical bone to be around 20-24 GPa (Taylor et al., 2002; Bayraktar et al., 2004). Even though bone is known to be orthotropic (Wirtz et al., 2000; Taylor et al., 2002), it is usually assumed isotropic in subject specific FE models (Keyak et al., 1998; Bessho et al., 2006; Taddei et al., 2007; Helgason et al., 2007; Schileo et al., 2007). Baca et al. (2008) found that material anisotropy only had a minor effect on results in FE models of intact femurs, as long as inhomogenous material properties were included in the model. For simplicity, the same assumption was used in our FE models, both intact and post-operative. In operated femurs, the implant is wedged into the femur during loading, thus increasing the hoop strain in the bone. Assuming material isotropy for a femur with an implant might therefore produce an underestimation of strains in the circumferential direction.

In the 3D models of the femurs, the endosteal surface was defined by the inner cortical contours derived from the CT images. The 3D model of the prosthesis was then placed inside the cancellous bone and medullary canal. From the femur-prosthesis assembly we observed that there was a tight fit between the stem and endosteal surface. The antero-posterior and varus-valgus orientation of the prosthesis in the FE models was therefore well defined by the endosteal surface of the cortical bone. Postoperative radiographs of the femurs were used to check the stem position in the FE models and confirmed the tight fit between stem and endosteal surface. The main challenge was to recreate the neck resection and anteversion of the prosthesis. It has been shown that errors in medial offset can induce errors when assessing the stress shielding effect of a femoral stem

(Cristofolini and Viceconti, 1999). We did not have any method of accurately verifying the positioning of the femoral stem in the FE models, and this represents a major limitation of the present study. A more accurate procedure for replicating the implant position in the FE models would probably improve the results considerably.

The choice of surface parameters is often based on pragmatic considerations to get stable simulations with good convergence. A wide range of normal stiffnesses and frictional factors used to describe the contact surfaces can therefore be found in literature (Bernakiewicz and Viceconti, 2002). Viceconti et al. (2000) found a frictional factor of 0.3 to produce the best results when initial contact pressure due to press fitting of the stem was included in the FE model. Initial contact pressure plays an important role for the interfacial micromotion between bone and implant, and it may also affect stress shielding if the contact pressure alters load transfer to the bone (Jasty et al., 1994). However, the degree of contact pressure and interference penetration achieved during implantation is difficult to determine as it will vary considerably with the size of the implant, size and quality of the femur, and the force used during implantation. The level of pre-stress achieved through press-fitting is also known to decrease with time due to viscoelastic relaxation (Norman et al., 2006). In our models this contact pressure was therefore ignored and a frictional factor of 0.4 used for the interface (Viceconti et al., 2000).

Various biomechanical studies have used FE models to study the stress- and strain-pattern in femurs implanted with a prosthesis (Rohlmann et al., 1983; Rubin et al., 1993; McNamara et al., 1997; Stolk et al., 2002a; Viceconti et al., 2001). Validation has largely been limited to subject specific FE models of intact femurs or implant-bone assemblies using composite femur replicas (McNamara et al., 1997; Viceconti et al., 2001; Stolk et al., 2002a; Completo et al., 2007). This study has shown that subject specific FE models successfully describe the overall stress shielding effect of the prosthesis, and manage to predict the differences in stress shielding pattern measured in vitro in the various femurs. The predictions of stress shielding were poor for some of the smallest femurs, but the results are still quite encouraging. Resolving the uncertainties regarding stem positioning and employing a proper anisotropic material model for bone would probably improve the predictive strength of the FE models considerably. Subject specific FE models may be used in the development of new prostheses; either for customized implants, allowing preclinical evaluation of the prosthesis using the femoral geometry of the patient, or for standard implants, allowing preclinical evaluation in a wide range of femoral geometries. FE models will not replace in vitro testing of prosthetic design altogether, but may help eliminate unfortunate design features at an earlier stage and thus prove to be a valuable supplement.

Acknowledgement

CT scanning was performed by Liv Nesje at the department of Radiology (St.Olavs Hospital), and implantation of the prostheses by dr. Arild Aamodt at the department of orthopaedic surgery (St.Olavs Hospital). Jomar Klaksvik (Norwegian Orthopaedic Implant Research Unit) assisted with the experimental measurements. We would like to thank DePuy for supplying the CAD models of the prostheses. The study was funded by the Norwegian Orthopaedic Implant Research Unit.

4.5 Subject specific finite element analysis of implant stability for a cementless femoral stem[7]

Abstract

Background: The primary stability of a cementless implant is crucial to ensure long term stability through osseointegration. In the present study we have examined how subject specific finite element models can be used to evaluate the stability of a cementless femoral stem.

Methods: Micromotion on the bone-implant interface of a cementless stem was measured experimentally in six human cadaver femurs. Subject specific finite element models were built from computed tomography of the same femurs, and used to simulate the same load scenario used experimentally.

Findings: Both experimental measurements and numerical analyses showed a tendency of increased rotational stability for bigger implants. Good correlation was found between measurements and calculated values of axial rotation ($R^2=0.74$, $p<0.001$). The finite element models produced interface micromotion of the same magnitude as measured experimentally, with micromotion generally below 40 μm. Bigger femoral stems were found to decrease the micromotion in the experimental measurements. This tendency could not be recognised in the interface micromotion from the finite element models.

Interpretation: The finite element models showed limited success in predicting interfacial micromotion, but reproduced a similar pattern of rotational stability for the implants as seen experimentally. Since rotation in retroversion is often the main concern when studying implant stability, subject specific finite element models could be employed for pre-clinical evaluation of implants.

4.5.1 Introduction

The modern procedure of total hip replacement (THR) was pioneered in the 1960s by orthopaedic surgeon Sir John Charnley. Charnley introduced the low friction hip

---

[7] Pettersen, S. H., Wik, T. S., Skallerud, B., (2009). Subject specific finite element analysis of implant stability for a cementless femoral stem. accepted in Clin.Biomech.

implant with a femoral stem cemented into the medullary canal. The survival rate of cemented THR is around 90% after a 15 year period, and bone cement still remains the most common form of fixating the femoral and acetabular components (The Norwegian Arthroplasty Register, 2008). Bone cement does however show a tendency of gradual debonding over the years (Jasty et al., 1991), which may result in cement debris in the joint and loosening of the implant. The debris causes increased wear between the femoral head and acetabular component and induces osteolysis around the prosthesis (Jacobs et al., 2001). Cementless implants were introduced to eliminate these problems. Instead of using bone cement, they are fixated by bone growing into porous coated areas on the implant, socalled osseointegration.

The primary stability of a cementless implant is vital for osseointegration to occur. Interface micromotion around 40 μm has been shown to give partial ingrowth, while micromotion exceeding 150 μm inhibits bone ingrowth completely (Pilliar et al., 1986; Jasty et al., 1997). The primary stability of the stem is therefore one of the crucial features to study in a preclinical evaluation of a new prosthetic design. Although human cadaver femurs are regularly used for preclinical evaluations of implants, the use of human test specimen raises both ethical and practical concerns. Composite femur replicas have been used in numerous studies evaluating prosthetic designs and implantation techniques (McNamara et al., 1997; Viceconti et al., 2001; Sangiorgio et al., 2004; Park et al., 2008). The replicas simplify mechanical testing, but the interindividual variation seen in patients is lost. Finite element (FE) models have been employed in studies of the contact surface of both cemented (Verdonschot and Huiskes, 1996; Ramaniraka et al., 2000; Stolk et al., 2002a) and uncemented prosthesis (Rubin et al., 1993; Viceconti et al., 2000; Bernakiewicz and Viceconti, 2002; Sakai et al., 2006; 2008; Abdul-Kadir et al., 2008; Reggiani et al., 2007; 2008). These computational models enable us to study regions not accessible for experimental measurements and to easily isolate parameters and study their influence. Various FE studies have found different parameters to affect implant stability; varying joint and muscle forces (Pancanti et al., 2003), bone quality (Wong et al., 2005) and bone size (Viceconti et al., 2006). These studies have relied solely on FE analyses, modifying a FE model to simulate different material properties, load and boundary conditions. By combining computed tomography (CT) with the FE method, it is possible to build numerical models that incorporate both the geometry and material properties of individual femurs. These socalled subject specific FE models can be used to compare different implant geometries in one particular femoral geometry, and also analyse one particular implant geometry in a wider range of femoral geometries.

The purpose of the present study is to validate subject specific FE models simulating the stability of a cementless femoral stem. The results from FE analyses will be compared with experimental measurements on the same femurs.

4.5.2 Material and Methods

Human femurs were collected from six individuals, 3 males and 3 females aged 49-74 years (average 61 years). They are identified herein by lab code numbers and L for left and R for right. The study was approved by the regional medical research ethics committee. The femurs were examined by dual energy x-ray absorptiometry (DEXA) and plain radiography and excluded if signs of osteoporosis or other skeletal pathologies were found. Results from DEXA measurements of the individual femurs are shown table 4.3. The femurs were CT scanned (Siemens Somatom Sensation 64, Erlangen, Germany) at 140 kV, 300 mAs and B50f reconstruction kernel with a pixel spacing of approximately 0.35 mm, 0.75 mm slice thickness and 0.7 mm slice distance. Bags of water were placed around the femurs during CT scanning to reduce beam hardening. A calibration phantom consisting of different mixtures of calcium carbonate and PMMA was used to convert the Hounsfield Units (HU) of the CT scans to equivalents of bone mineral density[8].

Table 4.3: Physical characteristics of the femurs used in the study.

Femur	Age	Gender	DEXA Intertrochanteric region		Implant size
			BMD [g/cm^2]	Area [cm^2]	
01R	60	M	1.034	28.86	8
03L	61	F	1.020	20.78	5
08L	49	M	0.991	29.40	4
13L	74	M	1.254	31.13	4
18R	59	F	1.078	24.42	6
19R	65	F	0.967	23.79	5

---

[8] See *Chapter 2: Relating CT gray-scale values to bone density.*

The femurs were stored at -20°C, thawed at room temperature and prepared for testing as decribed by Aamodt et al. (2001). The condyles were resected and the femur cemented into a steel cylinder 25 cm distally of the upper tip of the greater trochanter. The femurs were implanted with a straight cementless prosthesis (DePuy Summit™, Leeds, UK) by an experienced orthopaedic surgeon.

A load jig was used to simulate joint loads and muscle forces in the experimental measurement (Aamodt et al., 2002). The femurs were tilted 12° in valgus and constrained distally, allowing rotation about the proximal-distal axis. The load jig consisted of a lever arm acting as the pelvis with an acetabular cup transferring load to the femoral head, and a strap attached to the greater trochanter acting as abductor muscles. The position of the trochanter strap was adjusted so that it acted at an angle of 15° with the vertical axis.

Loads were applied in three steps using a material testing machine (MTS 858 Minibionix II, Eden Prairie, USA). A vertical load of 600N was applied to the end of the lever arm simulating single leg stance. This was followed by an additional torque of 13.5 Nm applied to the femur distally to simulate stair climbing. Finally, the femur was unloaded to 0 Nm torque and 20 N vertical load. This load setup gives a joint contact force of 308% relative to vertical load. Telemetric load measurements from hip prosthesis have reported joint loads of approximately 250% relative to the body weight (BW) during slow walking and single leg stance (Bergmann et al., 1993; 2001), and a peak implant torsional moment of 2.24 % BW·m during stairclimbing (Bergmann et al., 2001). A vertical load of 600 N in our load jig thus represents a BW of 74 kg, and the torsional moment 1.82% BW·m.

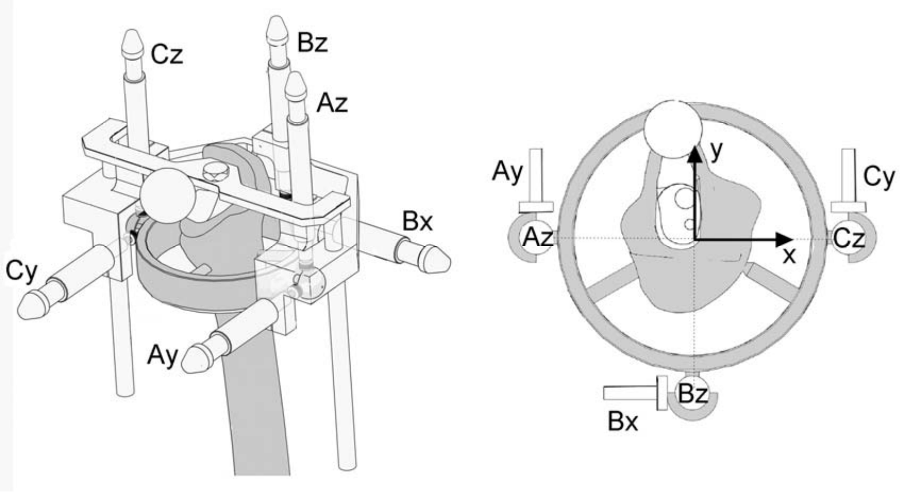

Figure 4.19: The fixture used to capture the motion of the implant. The yoke with LVDTs is attached to the shoulder of the implant (white) and measures the motion of the ring attached to the femur (gray). The ring and LVDTs can be repositioned to measure the relative movement between implant and bone at different levels of the stem.

Micromotion measurements

The measurements were performed using a specially designed fixture to capture the micromotion of the femoral stem relative to the bone (figure 4.19). A yoke with displacement transducers (LVDT) (WA10 and W1T3, accuracy < 1 μm, HBM GmbH, Darmstadt, Germany) was attached to a threaded hole on the shoulder of the prosthesis, and a slot in the hole restricted any twisting between the prosthesis and yoke (figure 4.20, right). A ring with three hemispherical ceramic ball probes was attached to the outside of the femur using a positioning guide to ensure that the ring and yoke were coaxial. The yoke was adjustable to enable measurement at any level along the stem. Measurements were performed at two levels; 15 mm below the proximal coating boundary and 5 mm above the distal coating boundary (figure 4.20, left).

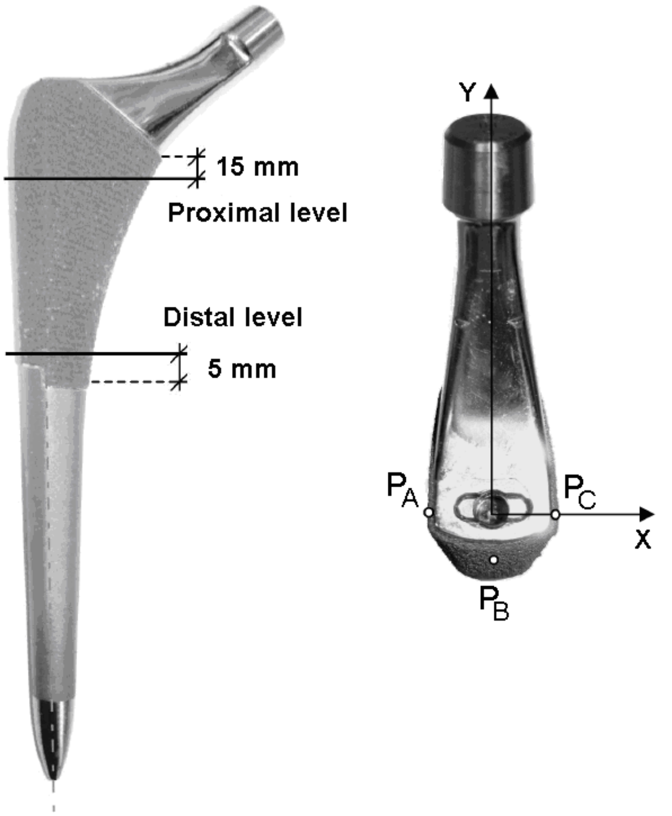

Figure 4.20: The Summit cementless prosthesis. Measurements were performed at two levels in the coating area; 15 mm below the upper coating boundary, and 5 mm above the lower coating boundary. Micromotion was calculated for three points on the implant surface for each level; anterior side (P_A), lateral side (P_B) and posterior side (P_C).

The measuring method presumes that the implant can be considered as a rigid body compared to the bone. In a prestudy the deformation between the shoulder and the distal tip of a femoral stem was measured by drilling holes through the cortical wall and attaching the ring directly on the distal tip. The stem deformation was measured to be 0.7 μm over the whole length of the stem, which supports the assumption of the prosthesis being rigid in comparison to the surrounding bone. The ring follows the deformation of the femur, and the complete femur is not considered rigid. However, the cross section of bone at the level where micromotion is measured is assumed to move like a rigid body. The movement of the ring relative to the implant-yoke assembly was measured with LVDTs in two directions on each ball probe (fig.1, right), which gives a total of six measured displacements. Since a rigid body has six degrees of freedom, the spatial displacement vector of each ball probe can be calculated. The distance from the axis of the yoke and out to the points P_A, P_B and P_C (figure 4.20, right) on the implant surface was measured with a slide calliper at the proximal and distal level. Using the distance between the ball probes and their spatial displacement vectors, we can determine the relative movement between the bone and implant at P_A, P_B and P_C by interpolation. Calculation of interface micromotion, relative translation and rotation from the experimental measurements is given in the supplementary material[9].

The operated femurs used in the present study had undergone approximately 50 load cycles as part of a separate study (Pettersen et al., 2009) prior to the micromotion measurement. The implants were therefore assumed to have settled firmly into the femurs. Five load cycles were run at each measurement level in our study: one preconditioning cycle, followed by four data collection cycles. The average values from the four data collection cycles were used in the study.

Finite Element Models

FE models of each femur were created from inner and outer contours of cortical bone extracted from CT scans. The 3D models were constructed and meshed using regular CAD software (SolidWorks 2005, CosmosWorks 2005). Cortical and cancellous bone was modelled as separate sections, and the medullary canal below the lesser trochanter as empty. The FE models were prepared for analysis and exported to ABAQUS/Standard 6.7 (Simulia, Providence, USA) using scripts written in MATLAB 7.1 (The Mathworks, Natick, USA). Second order tetrahedral elements (C3D10M) with a global element size of 3 mm were used for the FE models. Material properties were mapped to the FE model using the CT attenuation values of the pixels inside each element (Zannoni et al., 1998) and the density-stiffness relationship of Verhulp et al. (2006).

$$E = 33900 \cdot \rho_{min}^{2.2} \text{ [MPa], for } \rho_{min} \leq 0.27 \text{ [g/cm}^3\text{]} \qquad (4.18)$$

---

[9] See *Appendix IV: Calculating experimental micromotion, translation and rotation.*

$$E = 11164 \cdot \rho_{min} - 1112 \text{ [MPa], for } 0.27 < \rho_{min} < 0.60 \text{ [g/cm}^3\text{]} \tag{4.19}$$

$$E = 15597 \cdot \rho_{min}^{2.01} \text{ [MPa], for } \rho_{min} \geq 0.60 \text{ [g/cm}^3\text{]} \tag{4.20}$$

The density-stiffness relationship was found to give good predictions of cortical strain in a previous study (Pettersen et al., 2009). Beam and connector elements were used to simulate the load jig and the boundary conditions of the femur (figure 4.21, left). A *slipring* element was used between points C and F and material flow constrained in both points. The *slipring* element thus behaved like a truss element and simulated the behaviour of the trochanter-band. A *join* connector was used between B and E, allowing the model to rotate freely in point E. By combining a *join* and *revolute* element between G and H, the distal femur was allowed to rotate about the femoral axis. The vertical load was applied in point A and torque in point H.

3D models of the cementless Summit prostheses were supplied by the manufacturer (dePuy, Leeds, UK). The ribbed surface of the coating area was modelled as smooth in the FE models to simplify contact analysis. The stem was positioned in the cancellous bone and medullary canal so that penetration into cortical bone was minimal. The neck resection and orientation of the visible parts of the implant were reconstructed from post-operative photographs of the femurs. The distal tip of the stem was expected to come in contact with the endosteum laterally during loading, and was positioned with initial contact in this region. Implant positioning in the FE models was checked against radiographs of the operated femurs. The interface was modelled using the augmented Lagrange contact algorithm with finite sliding face-to-face contact elements, with the prosthesis as master surface and the femoral cavity as slave. The coefficient of friction was set to 0.4 and normal stiffness to 1200 N/mm. The relative penetration tolerance of the surfaces was set to 0.2%, except for 08L where the tolerance was set to 0.3% due to convergence problems. The FE models had an average interface element length of 2 mm, giving a maximum residual penetration of 4 µm (6 µm for 08L). The finished FE models had 419,897 (03L) to 597,934 (01R) degrees of freedom (54,126 and 83,058 elements).

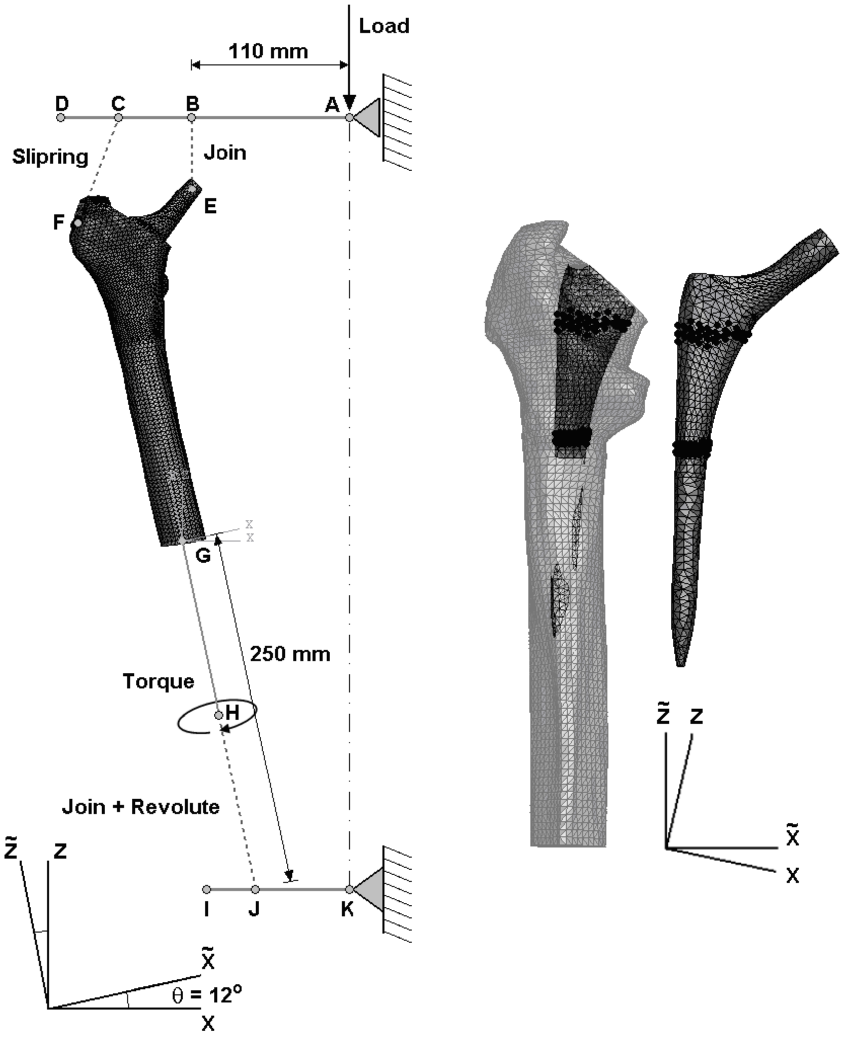

Figure 4.21: The complete FE model with femur and load jig (left). The beam elements are shown as gray, solid lines and the connector elements as dashed lines. The node sets of the proximal and distal interface levels are shown right. The displacement results of the node sets were transformed from the global coordinate system of the load jig (X, Z) to the coordinate system of the femur ($\tilde{X}$, $\tilde{Z}$).

Interface micromotion was calculated between the nodes on the implant and the corresponding nodes on the femoral cavity (figure 4.21, right). The FE results were compared with experimental measurements of micromotion on the anterior, lateral and posterior side of the implant both proximally and distally. In addition, the movement of the implant relative to the bone interface was decomposed into translations and rotations. In our study we have focused on the rotation (retroversion) and translation (proximal-distal) along the longitudinal axis of the implant ($\tilde{Z}$-axis). Calculation of translations and rotations from the FE analyses is explained in the supplementary material[10].

Two load cycles were simulated for the remaining femurs; one load cycle to pre-stress the bone, and a second load cycle for data collection. Interface micromotion and axial translation (ΔT_Z) was calculated from the unloaded step (step 3) to stairclimbing (step 5). Axial rotation ($\Delta\theta_Z$) during torsional loading was calculated from single leg stance (step 4) to stairclimbing (step 5). Five load cycles (15 load steps) were simulated for femur 19R to investigate the movement of the prosthesis over several load cycles.

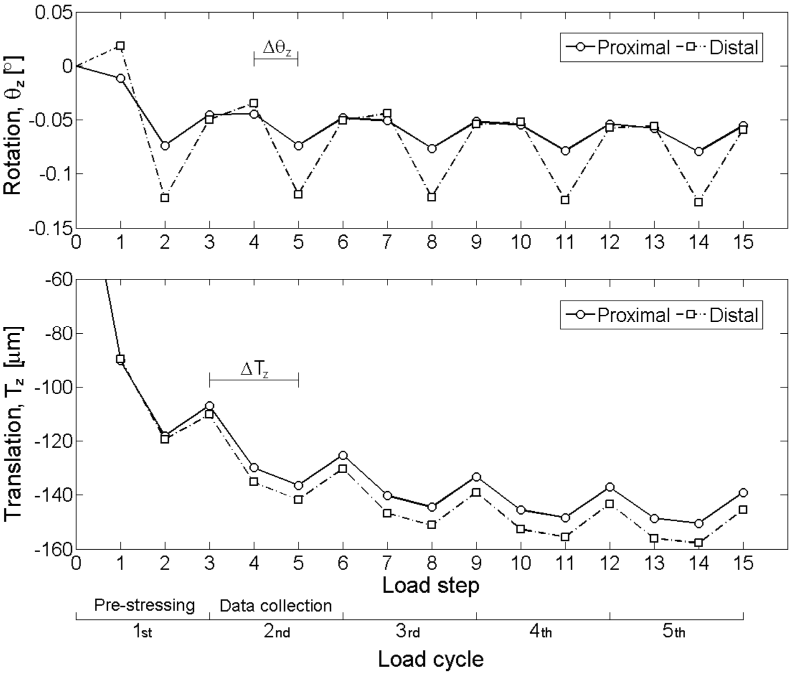

Figure 4.22: FE results showing the relative axial rotation and translation for 19R through 15 load steps (5 cycles). A large irreversible translation of the implant can be seen in the first load cycle.

---

[10] See *Appendix V: Decomposition of FE node displacements into translation and rotation.*

4.5.3 Results

In the FE analyses a considerable degree of axial implant migration was observed in the first load cycle (figure 4.22). The axial translation for the different FE models was 45-120 μm in the first load cycle (initial to step 2), but was reduced to 14-32 μm in the second load cycle (step 3 to step 5). Even though the prosthesis in femur 19R continued to migrate downwards for several cycles, the migration was most severe in the pre-stressing cycle. The axial rotation during torsional load is also larger in the pre-stressing cycle, but is largely stable in the cycles afterwards.

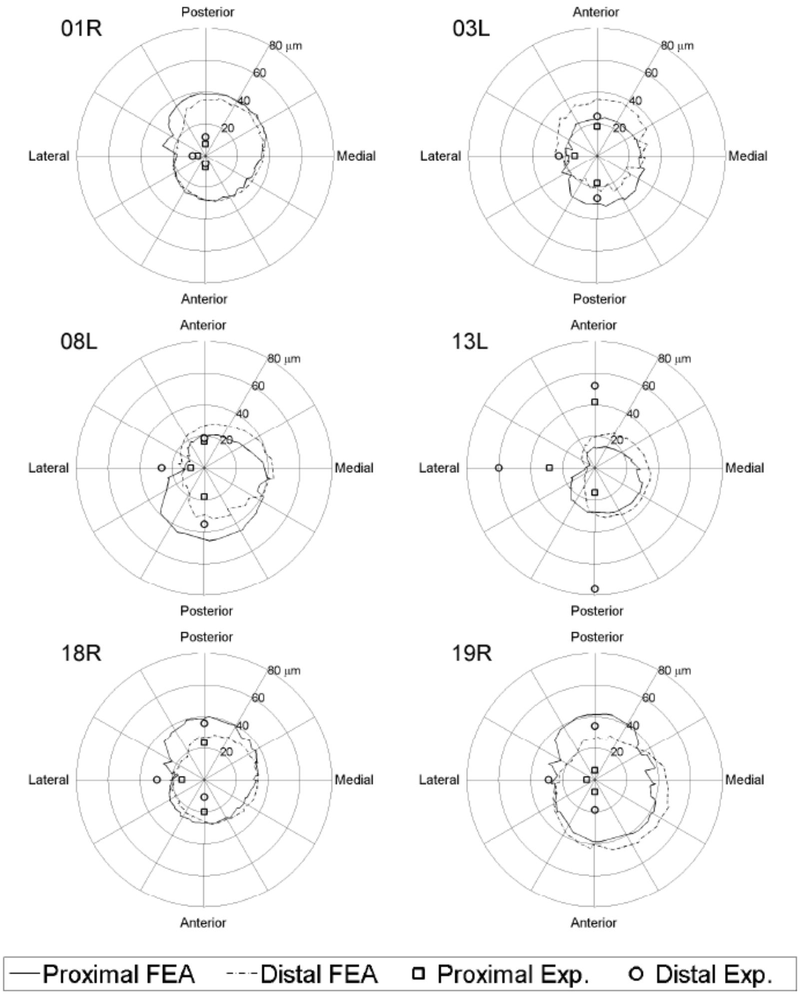

Figure 4.23: Interface micromotion around the proximal and distal levels of the implants. Micromotion was calculated from unloaded state (20N) to stairclimbing. Experimental values are the mean values from the four datacollection cycles. FE values were calculated from the load step 3 to 5.

Experimental and FE interface micromotion of the implants is shown in figure 4.23. The FE analyses produced results of the same magnitude as those measured experimentally, with micromotion between 20 and 40 µm on both the proximal and distal level. However, the micromotion pattern predicted by the FE analyses in the individual femurs differed considerably from the pattern observed experimentally. The experimental measurements gave the largest magnitude of micromotion for femur 13L; with a maximum proximally of 42 μm on the anterior side, and a maximum distally of 76 μm on the posterior side. However, in the FE analyses this femur showed the smallest degree of micromotion; with micromotion below 20 μm for large portions of the proximal and distal levels. The smallest measurements of micromotion were found for femur 01R; with a maximum distally of 12 μm on the posterior side and the rest of the measurements below 10 μm. In the FE analyses, this femur had micromotion between 20 and 40 μm both proximally and distally. The FE analyses gave the highest magnitude of micromotion for femur 19R; with micromotion largely around 40 μm on both the proximal and distal level.

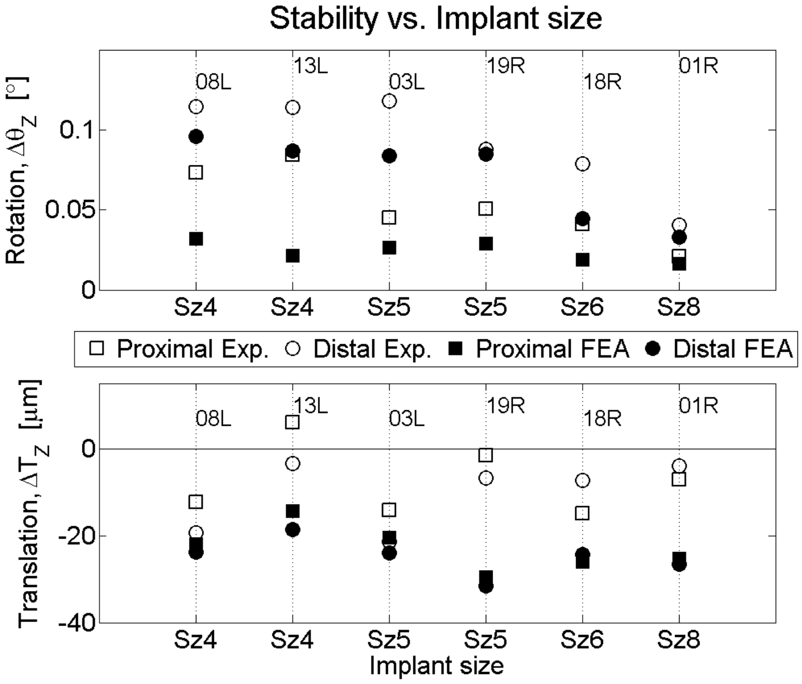

Figure 4.24: Stability of the implants versus implant size. Big femoral stems improve rotational stability between implant and bone. Stem size has no apparent effect on the axial translation.

The correlation between experimental and FE results was good for axial rotation (R^2=0.74, p<0.001). Figure 4.24 shows a higher degree of rotational stability for bigger implants. The axial rotation is also considerably lower on the proximal level. These two tendencies are reflected in both the experimental measurements and the FE results. For axial translation the correlation between experimental and FE results was poor

(R^2=0.05, p=0.51). The FE analyses generally predicted higher axial translation than found experimentally. The measurements on femur 13L show that the implant is moving slightly upwards at the proximal level. In the FE analyses, all axial translations of the implants were directed downwards.

4.5.4 Discussion

Initial implant stability has been shown to be critical for the long term stability of cementless prostheses (Pilliar et al., 1986; Jasty et al., 1997). The purpose of the present study was to validate subject specific FE models used for simulating the relative movement between a cementless femoral stem and bone. The results from the FE analyses were compared with experimental measurements on the same femurs.

Verdonschot and Huiskes (1996) found that when including friction on the bone-cement interface, relative interface motion was considerably larger in the first load cycle than in the cycles following afterwards. The same was observed in our FE analyses (figure 4.22). When the implant is unloaded after the first load cycle, only a part of the axial translation is recovered, and the implant remains wedged into the bone cavity. The wedging of the implant generates a pre-stress in the bone holding the implant in place. The same method of including bone pre-stress in the FE models has been used in previous studies (Viceconti et al., 2000; Goetzen et al., 2005). The results from the first load cycle were therefore excluded from the study, and only the results from the second cycle compared to the experimental measurements. Only one femur was simulated for five cycles due to the considerable computation time demanded by the analyses.

The FE analyses predicted interfacial micromotion of the same magnitudes as measured experimentally, but failed to show the same patterns. The experimental measurements gave micromotion below 40 μm for all femurs except 13L. In the FE analyses micromotion generally varied between 20 and 40 μm. Both the predicted and measured micromotion are in the area were a prosthesis would be assumed sufficiently stable. Westphal et al. (2006) reported a cyclic total translation around 400 μm for the Summit prosthesis in vitro. However, their experimental setup differs considerably from ours and the results are therefore not directly comparable. Femur 13L showed the highest degree of micromotion in the measurements, with micromotion exceeding 40 μm, but had the lowest degree of micromotion in the FE analyses. Conversely, femur 01R which had the lowest micromotion in the measurements, showed a fairly high degree of micromotion in the FE analyses. The total interface micromotion is the resultant of relative movement in all three spatial directions on the contact surface. In order to better analyse the results, movement was decomposed into translations and rotations. The rotational stability is usually the main concern when testing the primary stability of implants (Sugiyama et al., 1992; Baleani et al., 2000; Viceconti et al., 2001; Ries et al., 2003; Meneghini et al., 2006; Reggiani et al., 2007; Sakai et al., 2008). In our study we have concentrated on two main implant movements: translation and rotation along the stem axis. Good correlation was found between FE analysis and experimental measurements for the axial rotation, but not for axial translation. The measurements showed that the implant seemed to be moving upwards for femur 13L on the proximal level despite being subjected to a load downwards. Similar behaviour was reported for some of the measurements of Kassi et al. (2005), who suspected it to be caused by the implant tilting on the calcar. Even though the axial rotation for femur 13L is relatively high in the FE analysis, it still has the lowest magnitude of interface micromotion. This is due to the short radial distance from stem axis to the contact surface, which gives smaller interface micromotion for small stems even though axial rotation is large. The opposite applies to femur 01R with the biggest stem size, which produces fairly large interface micromotion in the FE analysis despite low axial rotation.

In order to calculate the spatial micromotion of the three points P_A, P_B and P_C, we assume the cross-section of bone at the measuring level moves like a rigid body. This implies that any deformation across the cortical wall is disregarded and that the movement of the measuring points are mutually dependent, i.e. that the y-translations measured of ball probes A and C to can be used to determine the y-translation of B. Monti et al. (1999) found the shear deformation across the wall to give an overestimation of micromotion of 2-4 μm. Usually, micromotion is measured directly with extensometers and LVDTs (Baleani et al., 2000; Kassi et al., 2005; Britton et al., 2004) or optoelectronic measuring devices (Buhler et al., 1997a; 1997b; Speirs et al., 2000; Nogler et al., 2004) through holes drilled through the cortical wall. As the holes introduce a mechanical weakening of the bone, measurements can only be obtained at a few points along the stem (Buhler et al., 1997a). The measuring method used in the present study does not give a direct measurement of the interface micromotion, but instead uses the movement of the ceramic ball probes A, B and C to make an assessment of the micromotion. The main advantage is that it leaves the cortical wall intact, enabling repeated measurements at several levels along the stem. Also, since micromotion is assessed at three points at each measuring level, we can analyse the relative motion between stem and bone by decomposing it into translations and rotations.

To our knowledge, only three articles have reported micromotion predictions with subject specific FE models of human cadaver femora and validation against in vitro measurements; Reggiani et al. (2007; 2008) simulating the stability of an implant under torsional load, and Abdul-Kadir et al. (2008) under axial compression. In our study, we have used loads that resemble the joint and muscle forces during single leg stance and stairclimbing and increased the number of femurs in the study. Two parametric studies have reported on different variables affecting implant micromotion using FE models (Wong et al., 2005; Viceconti et al., 2006). Wong et al. (2005) found good bone quality to improve implant stability. Femur 13L had the highest intertrochanteric BMD of 1.25 g/cm^2 (table 4.3), but was still the least stable in the experimental measurements. Intertrochanteric BMD was generally around 1.0 g/cm^2 for the remaining femurs. Due to the small range in BMD and small sample size of femurs, it was not possible to conclude on the effect of bone quality on implant stability in the present study. Viceconti et al. (2006) identified femoral size as the most important parameter followed by body weight and bone quality. Viceconti et al. (2006) scaled the size of the FE model and found smaller bones with a consequently smaller prosthesis to produce higher implant micromotion. This seems reasonable since smaller sized stems also have a smaller contact surface. Our results showed a tendency of reduced rotational stability for smaller stems. However, contrary to the assumptions of Viceconti et al. (2006), the smallest stems in our study were found in the two biggest femurs (08L and 13L) with the largest intertrochanteric area (table 4.3) and were both from male donors. CT scans showed female femurs to have relatively wide medullary canals compared to male femurs despite their smaller external size. These geometrical differences between male and female femurs are quite typical (Dorr et al., 1993).

The proximal part of the Summit stem is porous coated on a ribbed substrate (radial ZTT™ structure) which is intended to provide better stability. The femoral cavity reamed through the cancellous bone is also quite rough and does not always match the shape of the prosthesis, creating interface gaps at some locations. Additionally, the implant is hammered in place until the orthopaedic surgeon finds it sufficiently stable, thus building up an initial surface pressure on the interface. All these factors affect the properties of the bone-implant interface. The normal displacement of the contact surfaces achieved during insertion of the implant is usually referred to as press fit or interference fit. Even though the interference fit can be quite considerable, its effect on bone pre-stress is known to reduce over time due to viscoelastic relaxation (Norman et al., 2006). Abdul-Kadir et al. (2008) estimated an interference fit of 50-100 μm to be realistic for press-fitted stems in a clinical situation, but found a simulated interference fit of 1-2 μm in the FE analyses to better reproduce the micromotion measured experimentally. Another complicating factor is nonlinearity of the interface friction coefficient (Shirazi-Adl et al., 1993). Thus, the stability of the femoral stem in the clinical and experimental scenario is affected by several factors that are difficult, if not impossible, to quantify. In our analyses, these factors were simplified to achieve convergence and reduce the computation time: the coating area was modelled as smooth, the coefficient of friction kept constant, and the same surface conditions used for the whole contact area. Thus, our FE models do not consider the contribution of the surface texture in providing stability for the implant, but only the geometrical shape of the stem. Interference fit from the implantation was ignored in the FE analyses. However, bone pre-stressing from the implant being wedged into the femur during loading was included in the FE simulations by using the first load cycle for pre-stressing. Reggiani et al. (2008) found the difference in micromotion between FE analyses of "planned" and "actual" stem position to be 13%. The error due to inaccurate stem positioning in our FE models is probably of similar magnitude. All these factors affect the micromotion results of the FE models. Given the complexity of the contact problems and the simplifications made to the FE models, it seems unreasonable to expect an accurate match between micromotion measured experimentally and numerical FE models. However, we found that the subject specific FE models manage to reproduce the pattern of axial rotation observed between the different stems in vitro.

Stairclimbing is associated with torsional loads forcing the femoral head in retroversion, and has been found to be the most critical load case for the stability of femoral stems (Stolk et al., 2002b; Kassi et al., 2005). In the present study we have demonstrated that subject specific FE models could be used to assess rotational stability of a cementless femoral stem. Osseointegration depends on the magnitude of interface micromotion, and not rotations or translations. However, when evaluating different stem geometries it is useful to know if excessive micromotion is due to poor stability with respect to axial translation or to rotations in retroversion and varus-valgus. The designer can then adjust the stem geometry accordingly and improve its micromotion properties. The subject specific FE models used in the present study have also shown to be able to predict the changes in cortical strain after implantation (Pettersen et al., 2009). FE models as described in the present study could thus be used for a full evaluation of both the stress shielding effect and rotational stability of a femoral stem, and be a useful tool in the preclinical testing of new prosthetic designs.

Acknowledgements

CT scanning was performed by Liv Nesje at the department of Radiology (St.Olavs Hospital), and implantation of the prostheses by dr. Arild Aamodt at the department of orthopaedic surgery (St.Olavs Hospital). Jomar Klaksvik (Norwegian Orthopaedic Implant Research Unit) assisted at the experimental measurements. We would like to thank DePuy for supplying the CAD models of the prostheses. The study was funded by the Norwegian Orthopaedic Implant Research Unit, and was granted computational time by the Norwegian University of Science and Technology at the Notur High Performance Computing Consortium.

References

Aamodt, A., Kvistad, K. A., Andersen, E., Lund-Larsen, J., Eine, J., Benum, P., Husby, O. S., (1999). Determination of Hounsfield value for CT-based design of custom femoral stems. J.Bone Joint Surg Br. 81, 143-147.

Aamodt, A., Lund-Larsen, J., Eine, J., Andersen, E., Benum, P., Husby, O. S., (2001). Changes in proximal femoral strain after insertion of uncemented standard and customised femoral stems. An experimental study in human femora. J.Bone Joint Surg Br. 83, 921-929.

Aamodt, A., Lund-Larsen, J., Eine, J., Andersen, E., Benum, P., Husby, O. S., (2002). Mechanical stability of custom and anatomical femoral stems: an experimental study in human femora. Hip International 12, 263-273.

ABAQUS/Standard version 6.6, (2006). Continuum Elements. ABAQUS Analysis User's Manual vol. 4.

Abdul-Kadir, M. R., Hansen, U., Klabunde, R., Lucas, D., Amis, A., (2008). Finite element modelling of primary hip stem stability: The effect of interference fit. J.Biomech. 41, 587-594.

Austman, R. L., Quenneville, C. E., Beaton, B. J., King, G. J., Gordon, K. D., Dunning, C. E., (2008). Development of a testing methodology to quantify bone load transfer patterns for multiple stemmed implants in a single bone with an application in the distal ulna. J.Biomech.Eng 130, 024502.

Baca, V., Horak, Z., Mikulenka, P., Dzupa, V., (2008). Comparison of an inhomogeneous orthotropic and isotropic material models used for FE analyses. Med.Eng Phys.

Baleani, M., Cristofolini, L., Toni, A., (2000). Initial stability of a new hybrid fixation hip stem: experimental measurement of implant-bone micromotion under torsional load in comparison with cemented and cementless stems. J.Biomed.Mater.Res. 50, 605-615.

Bayraktar, H. H., Morgan, E. F., Niebur, G. L., Morris, G. E., Wong, E. K., Keaveny, T. M., (2004). Comparison of the elastic and yield properties of human femoral trabecular and cortical bone tissue. J.Biomech. 37, 27-35.

Bergmann, G., Deuretzbacher, G., Heller, M., Graichen, F., Rohlmann, A., Strauss, J., Duda, G. N., (2001). Hip contact forces and gait patterns from routine activities. J.Biomech. 34, 859-871.

Bergmann, G., Graichen, F., Rohlmann, A., (1993). Hip joint loading during walking and running, measured in two patients. J.Biomech. 26, 969-990.

Bernakiewicz, M., Viceconti, M., (2002). The role of parameter identification in finite element contact analyses with reference to orthopaedic biomechanics applications. J.Biomech. 35, 61-67.

Bessho, M., Ohnishi, I., Matsuyama, J., Matsumoto, T., Imai, K., Nakamura, K., (2006). Prediction of strength and strain of the proximal femur by a CT-based finite element method. J.Biomech.

Britton, J. R., Lyons, C. G., Prendergast, P. J., (2004). Measurement of the Relative Motion Between an Implant and Bone under Cyclic Loading. Strain 40, 193-202.

Broz, J. J., Simske, S. J., Greenberg, A. R., (1995). Material and compositional properties of selectively demineralized cortical bone. Journal of Biomechanics 28, 1357-1368.

Bugbee, W. D., Culpepper, W. J., Engh, C. A., Jr., Engh, C. A., Sr., (1997). Long-term clinical consequences of stress-shielding after total hip arthroplasty without cement. J.Bone Joint Surg Am. 79, 1007-1012.

Buhler, D. W., Berlemann, U., Lippuner, K., Jaeger, P., Nolte, L. P., (1997a). Three-dimensional primary stability of cementless femoral stems. Clin.Biomech.(Bristol., Avon.) 12, 75-86.

Buhler, D. W., Oxland, T. R., Nolte, L. P., (1997b). Design and evaluation of a device for measuring three-dimensional micromotions of press-fit femoral stem prostheses. Med.Eng Phys. 19, 187-199.

Canadian Institute for Health Information, (2008). 2007 Annual Report - Hip and Knee Replacements in Canada.

Carter, D. R., Hayes, W. C., (1977). The compressive behavior of bone as a two-phase porous structure. J.Bone Joint Surg Am. 59, 954-962.

Cody, D. D., Gross, G. J., Hou, F. J., Spencer, H. J., Goldstein, S. A., Fyhrie, D. P., (1999). Femoral strength is better predicted by finite element models than QCT and DXA. J.Biomech. 32, 1013-1020.

Completo, A., Fonseca, F., Simoes, J. A., (2007). Experimental validation of intact and implanted distal femur finite element models. J.Biomech. 40, 2467-2476.

Cristofolini, L., Viceconti, M., (1999). In vitro stress shielding measurements can be affected by large errors. J.Arthroplasty 14, 215-219.

Cristofolini, L., Viceconti, M., Cappello, A., Toni, A., (1996). Mechanical validation of whole bone composite femur models. J.Biomech. 29, 525-535.

Currey, J. D., (1969). The relationship between the stiffness and the mineral content of bone. J.Biomech. 2, 477-480.

Danish Hip Arthroplasty Register, (2008). Annual report 2007.

Dorr, L. D., Faugere, M. C., Mackel, A. M., Gruen, T. A., Bognar, B., Malluche, H. H., (1993). Structural and cellular assessment of bone quality of proximal femur. Bone 14, 231-242.

Engh, C. A., McGovern, T. F., Bobyn, J. D., Harris, W. H., (1992). A quantitative evaluation of periprosthetic bone-remodeling after cementless total hip arthroplasty. J.Bone Joint Surg Am. 74, 1009-1020.

Engh, C. A., Jr., Young, A. M., Engh, C. A., Sr., Hopper, R. H., Jr., (2003). Clinical consequences of stress shielding after porous-coated total hip arthroplasty. Clin.Orthop Relat Res. 157-163.

Glassman, A. H., Bobyn, J. D., Tanzer, M., (2006). New femoral designs: do they influence stress shielding? Clin.Orthop Relat Res. 453, 64-74.

Goetzen, N., Lampe, F., Nassut, R., Morlock, M. M., (2005). Load-shift--numerical evaluation of a new design philosophy for uncemented hip prostheses. J.Biomech. 38, 595-604.

Hangartner, T. N., Gilsanz, V., (1996). Evaluation of cortical bone by computed tomography. J.Bone Miner.Res. 11, 1518-1525.

Harris, W. H., (1992). Will stress shielding limit the longevity of cemented femoral components of total hip replacement? Clin.Orthop Relat Res. 274, 120-123.

Helgason, B., Perilli, E., Schileo, E., Taddei, F., Brynjolfsson, S., Viceconti, M., (2008). Mathematical relationships between bone density and mechanical properties: A literature review. Clin.Biomech.(Bristol., Avon.) 23, 135-146.

Helgason, B., Taddei, F., Palsson, H., Schileo, E., Cristofolini, L., Viceconti, M., Brynjolfsson, S., (2007). A modified method for assigning material properties to FE models of bones. Med.Eng Phys. (online).

Heller, M. O., Bergmann, G., Deuretzbacher, G., Durselen, L., Pohl, M., Claes, L., Haas, N. P., Duda, G. N., (2001). Musculo-skeletal loading conditions at the hip during walking and stair climbing. J.Biomech. 34, 883-893.

Hellmich, C., Ulm, F. J., (2002). Are mineralized tissues open crystal foams reinforced by crosslinked collagen? Some energy arguments. J.Biomech. 35, 1199-1212.

Jacobs, J. J., Roebuck, K. A., Archibeck, M., Hallab, N. J., Glant, T. T., (2001). Osteolysis: basic science. Clin.Orthop Relat Res. 71-77.

Jasty, M., Bragdon, C., Burke, D., O'Connor, D., Lowenstein, J., Harris, W. H., (1997). In vivo skeletal responses to porous-surfaced implants subjected to small induced motions. J.Bone Joint Surg Am. 79, 707-714.

Jasty, M., Maloney, W. J., Bragdon, C. R., O'Connor, D. O., Haire, T., Harris, W. H., (1991). The initiation of failure in cemented femoral components of hip arthroplasties. J.Bone Joint Surg Br. 73, 551-558.

Jasty, M., O'Connor, D. O., Henshaw, R. M., Harrigan, T. P., Harris, W. H., (1994). Fit of the uncemented femoral component and the use of cement influence the strain transfer the femoral cortex. J.Orthop Res. 12, 648-656.

Kaneko, T. S., Pejcic, M. R., Tehranzadeh, J., Keyak, J. H., (2003). Relationships between material properties and CT scan data of cortical bone with and without metastatic lesions. Med.Eng Phys. 25, 445-454.

Kassi, J. P., Heller, M. O., Stoeckle, U., Perka, C., Duda, G. N., (2005). Stair climbing is more critical than walking in pre-clinical assessment of primary stability in cementless THA in vitro. J.Biomech. 38, 1143-1154.

Keller, T. S., (1994). Predicting the Compressive Mechanical-Behavior of Bone. Journal of Biomechanics 27, 1159-1168.

Keller, T. S., Mao, Z., Spengler, D. M., (1990). Young's modulus, bending strength, and tissue physical properties of human compact bone. J.Orthop Res. 8, 592-603.

Kerner, J., Huiskes, R., van Lenthe, G. H., Weinans, H., Van, R. B., Engh, C. A., Amis, A. A., (1999). Correlation between pre-operative periprosthetic bone density and post-operative bone loss in THA can be explained by strain-adaptive remodelling. J.Biomech. 32, 695-703.

Kessler, O., Lacatusu, E., Sommers, M. B., Mayr, E., Bottlang, M., (2006). Malrotation in total knee arthroplasty: effect on tibial cortex strain captured by laser-based strain acquisition. Clin.Biomech.(Bristol., Avon.) 21, 603-609.

Keyak, J. H., Lee, I. Y., Skinner, H. B., (1994). Correlations between orthogonal mechanical properties and density of trabecular bone: use of different densitometric measures. J.Biomed.Mater.Res. 28, 1329-1336.

Keyak, J. H., Rossi, S. A., (2000). Prediction of femoral fracture load using finite element models: an examination of stress- and strain-based failure theories. J.Biomech. 33, 209-214.

Keyak, J. H., Rossi, S. A., Jones, K. A., Skinner, H. B., (1998). Prediction of femoral fracture load using automated finite element modeling. J.Biomech. 31**,** 125-133.

Kroger, H., Venesmaa, P., Jurvelin, J., Miettinen, H., Suomalainen, O., Alhava, E., (1998). Bone density at the proximal femur after total hip arthroplasty. Clin.Orthop Relat Res. 66-74.

Lanyon, L. E., Hampson, W. G., Goodship, A. E., Shah, J. S., (1975). Bone deformation recorded in vivo from strain gauges attached to the human tibial shaft. Acta Orthop Scand. 46**,** 256-268.

Lengsfeld, M., Burchard, R., Gunther, D., Pressel, T., Schmitt, J., Leppek, R., Griss, P., (2005). Femoral strain changes after total hip arthroplasty--patient-specific finite element analyses 12 years after operation. Med.Eng Phys. 27**,** 649-654.

Lengsfeld, M., Schmitt, J., Alter, P., Kaminsky, J., Leppek, R., (1998). Comparison of geometry-based and CT voxel-based finite element modelling and experimental validation. Med.Eng Phys. 20**,** 515-522.

Lennon, A. B., Prendergast, P. J., (2001). Evaluation of cement stresses in finite element analyses of cemented orthopaedic implants. J.Biomech.Eng 123**,** 623-628.

Martin, R. B., Sharkey, N. A., Burr, D. B., (1998). Forces in Joints. Skeletal Tissue Mechanics. Springer-Verlag, pp. 1-24.

McNamara, B. P., Cristofolini, L., Toni, A., Taylor, D., (1997). Relationship between bone-prosthesis bonding and load transfer in total hip reconstruction. J.Biomech. 30**,** 621-630.

Meneghini, R. M., Hallab, N. J., Berger, R. A., Jacobs, J. J., Paprosky, W. G., Rosenberg, A. G., (2006). Stem diameter and rotational stability in revision total hip arthroplasty: a biomechanical analysis. J.Orthop Surg 1**,** 5.

Mikic, B., Carter, D. R., (1995). Bone strain gage data and theoretical models of functional adaptation. J.Biomech. 28**,** 465-469.

Monti, L., Cristofolini, L., Viceconti, M., (1999). Methods for quantitative analysis of the primary stability in uncemented hip prostheses. Artif.Organs 23**,** 851-859.

Morgan, E. F., Bayraktar, H. H., Keaveny, T. M., (2003). Trabecular bone modulus-density relationships depend on anatomic site. J.Biomech. 36**,** 897-904.

Morlock, M., Schneider, E., Bluhm, A., Vollmer, M., Bergmann, G., Muller, V., Honl, M., (2001). Duration and frequency of every day activities in total hip patients. J.Biomech. 34**,** 873-881.

Nogler, M., Polikeit, A., Wimmer, C., Bruckner, A., Ferguson, S. J., Krismer, M., (2004). Primary stability of a robodoc implanted anatomical stem versus manual implantation. Clin.Biomech.(Bristol., Avon.) 19**,** 123-129.

Norman, T. L., Ackerman, E. S., Smith, T. S., Gruen, T. A., Yates, A. J., Blaha, J. D., Kish, V. L., (2006). Cortical bone viscoelasticity and fixation strength of press-fit femoral stems: an in-vitro model. J.Biomech.Eng 128**,** 13-17.

Pancanti, A., Bernakiewicz, M., Viceconti, M., (2003). The primary stability of a cementless stem varies between subjects as much as between activities. J.Biomech. 36**,** 777-785.

Park, Y., Shin, H., Choi, D., Albert, C., Yoon, Y. S., (2008). Primary stability of cementless stem in THA improved with reduced interfacial gaps. J.Biomech.Eng 130**,** 021008.

Pettersen, S. H., Wik, T. S., Skallerud, B., (2009). Subject specific finite element analysis of stress shielding around a cementless femoral stem. Clin.Biomech.(Bristol., Avon.) 24, 196-202.

Pilliar, R. M., Lee, J. M., Maniatopoulos, C., (1986). Observations on the effect of movement on bone ingrowth into porous-surfaced implants. Clin.Orthop Relat Res. 208, 108-113.

Ramaniraka, N. A., Rakotomanana, L. R., Leyvraz, P. F., (2000). The fixation of the cemented femoral component. Effects of stem stiffness, cement thickness and roughness of the cement-bone surface. J.Bone Joint Surg Br. 82, 297-303.

Reggiani, B., Cristofolini, L., Taddei, F., Viceconti, M., (2008). Sensitivity of the primary stability of a cementless hip stem to its position and orientation. Artif.Organs 32, 555-560.

Reggiani, B., Cristofolini, L., Varini, E., Viceconti, M., (2007). Predicting the subject-specific primary stability of cementless implants during pre-operative planning: Preliminary validation of subject-specific finite-element models. J.Biomech. 40, 2252-2258.

Rho, J. Y., Ashman, R. B., Turner, C. H., (1993). Young's modulus of trabecular and cortical bone material: ultrasonic and microtensile measurements. J.Biomech. 26, 111-119.

Rho, J. Y., Hobatho, M. C., Ashman, R. B., (1995). Relations of mechanical properties to density and CT numbers in human bone. Med.Eng Phys. 17, 347-355.

Rice, J. C., Cowin, S. C., Bowman, J. A., (1988). On the dependence of the elasticity and strength of cancellous bone on apparent density. J.Biomech. 21, 155-168.

Ries, M. D., Suzuki, Y., Renowitzky, G., Lotz, J. C., Barrack, R. L., Bourne, R. B., Rorabeck, C. H., (2003). Effect of cementless bowed stem distal surface contour and coronal slot on femoral bone strains and torsional stability. J.Arthroplasty 18, 494-498.

Rietbergen, B. v., Huiskes, R., Weinans, H., Sumner, D. R., Turner, T. M., Galante, J. O., (1993). ESB Research Award 1992. The mechanism of bone remodeling and resorption around press-fitted THA stems. J.Biomech. 26, 369-382.

Rohlmann, A., Mossner, U., Bergmann, G., Kolbel, R., (1983). Finite-element-analysis and experimental investigation in a femur with hip endoprosthesis. J.Biomech. 16, 727-742.

Rubin, P. J., Rakotomanana, R. L., Leyvraz, P. F., Zysset, P. K., Curnier, A., Heegaard, J. H., (1993). Frictional interface micromotions and anisotropic stress distribution in a femoral total hip component. J.Biomech. 26, 725-739.

Sakai, R., Iwama, A., Itoman, M., Mabuchi, K., (2008). Rotational stability based on displacements obtained by simulation and measurement when torsion loading is applied to hip stems. J.Orthop Sci. 13, 248-254.

Sakai, R., Kanai, N., Itoman, M., Mabuchi, K., (2006). Assessment of the fixation stiffness of some femoral stems of different designs. Clin.Biomech.(Bristol., Avon.) 21, 370-378.

Sangiorgio, S. N., Ebramzadeh, E., Longjohn, D. B., Dorr, L. D., (2004). Effects of dorsal flanges on fixation of a cemented total hip replacement femoral stem. J.Bone Joint Surg Am. 86-A, 813-820.

Schaffler, M. B., Burr, D. B., (1988). Stiffness of Compact-Bone - Effects of Porosity and Density. Journal of Biomechanics 21, 13-16.

Schileo, E., Taddei, F., Cristofolini, L., Viceconti, M., (2008). Subject-specific finite element models implementing a maximum principal strain criterion are able to estimate failure risk and fracture location on human femurs tested in vitro. J.Biomech. 41, 356-367.

Schileo, E., Taddei, F., Malandrino, A., Cristofolini, L., Viceconti, M., (2007). Subject-specific finite element models can accurately predict strain levels in long bones. J.Biomech. 40, 2982-2989.

Shirazi-Adl, A., Dammak, M., Paiement, G., (1993). Experimental determination of friction characteristics at the trabecular bone/porous-coated metal interface in cementless implants. J.Biomed.Mater.Res. 27, 167-175.

Speirs, A. D., Slomczykowski, M. A., Orr, T. E., Siebenrock, K., Nolte, L. P., (2000). Three-dimensional measurement of cemented femoral stem stability: an in vitro cadaver study. Clin.Biomech.(Bristol., Avon.) 15, 248-255.

Stauber, M., Rapillard, L., van Lenthe, G. H., Zysset, P., Muller, R., (2006). Importance of individual rods and plates in the assessment of bone quality and their contribution to bone stiffness. J.Bone Miner.Res. 21, 586-595.

Stolk, J., Verdonschot, N., Cristofolini, L., Toni, A., Huiskes, R., (2002a). Finite element and experimental models of cemented hip joint reconstructions can produce similar bone and cement strains in pre-clinical tests. J.Biomech. 35, 499-510.

Stolk, J., Verdonschot, N., Huiskes, R., (2001). Hip-joint and abductor-muscle forces adequately represent in vivo loading of a cemented total hip reconstruction. J.Biomech. 34, 917-926.

Stolk, J., Verdonschot, N., Huiskes, R., (2002b). Stair climbing is more detrimental to the cement in hip replacement than walking. Clin.Orthop Relat Res. 294-305.

Sugiyama, H., Whiteside, L. A., Engh, C. A., (1992). Torsional fixation of the femoral component in total hip arthroplasty. The effect of surgical press-fit technique. Clin.Orthop Relat Res. 187-193.

Taddei, F., Cristofolini, L., Martelli, S., Gill, H. S., Viceconti, M., (2006). Subject-specific finite element models of long bones: An in vitro evaluation of the overall accuracy. J.Biomech. 39, 2457-2467.

Taddei, F., Schileo, E., Helgason, B., Cristofolini, L., Viceconti, M., (2007). The material mapping strategy influences the accuracy of CT-based finite element models of bones: An evaluation against experimental measurements. Med.Eng Phys. 29, 973-979.

Taylor, W. R., Roland, E., Ploeg, H., Hertig, D., Klabunde, R., Warner, M. D., Hobatho, M. C., Rakotomanana, L., Clift, S. E., (2002). Determination of orthotropic bone elastic constants using FEA and modal analysis. J.Biomech. 35, 767-773.

Testi, D., Zannoni, C., Cappello, A., Viceconti, M., (2001). Border-tracing algorithm implementation for the femoral geometry reconstruction. Comput.Methods Programs Biomed. 65, 175-182.

The Norwegian Arthroplasty Register, (2008). Annual Report 2008.

Turner, A. W., Gillies, R. M., Sekel, R., Morris, P., Bruce, W., Walsh, W. R., (2005). Computational bone remodelling simulations and comparisons with DEXA results. J.Orthop Res. 23, 705-712.

Verdonschot, N., Huiskes, R., (1996). Mechanical effects of stem cement interface characteristics in total hip replacement. Clin.Orthop Relat Res. 326-336.

Verhulp, E., Rietbergen, B. v., Huiskes, R., (2006). Comparison of micro-level and continuum-level voxel models of the proximal femur. J.Biomech. 39, 2951-2957.

Viceconti, M., Brusi, G., Pancanti, A., Cristofolini, L., (2006). Primary stability of an anatomical cementless hip stem: a statistical analysis. J.Biomech. 39, 1169-1179.

Viceconti, M., Cristofolini, L., Baleani, M., Toni, A., (2001). Pre-clinical validation of a new partially cemented femoral prosthesis by synergetic use of numerical and experimental methods. J.Biomech. 34, 723-731.

Viceconti, M., Muccini, R., Bernakiewicz, M., Baleani, M., Cristofolini, L., (2000). Large-sliding contact elements accurately predict levels of bone-implant micromotion relevant to osseointegration. J.Biomech. 33, 1611-1618.

Viceconti, M., Zannoni, C., Testi, D., Cappello, A., (1999). CT data sets surface extraction for biomechanical modeling of long bones. Comput.Methods Programs Biomed. 59, 159-166.

Westphal, F. M., Bishop, N., Honl, M., Hille, E., Puschel, K., Morlock, M. M., (2006). Migration and cyclic motion of a new short-stemmed hip prosthesis--a biomechanical in vitro study. Clin.Biomech.(Bristol., Avon.) 21, 834-840.

Wirtz, D. C., Schiffers, N., Pandorf, T., Radermacher, K., Weichert, D., Forst, R., (2000). Critical evaluation of known bone material properties to realize anisotropic FE-simulation of the proximal femur. J.Biomech. 33, 1325-1330.

Wong, A. S., New, A. M., Isaacs, G., Taylor, M., (2005). Effect of bone material properties on the initial stability of a cementless hip stem: a finite element study. Proc.Inst.Mech.Eng [H.] 219, 265-275.

Yosibash, Z., Padan, R., Joskowicz, L., Milgrom, C., (2007). A CT-based high-order finite element analysis of the human proximal femur compared to in-vitro experiments. J.Biomech.Eng 129, 297-309.

Zannoni, C., Mantovani, R., Viceconti, M., (1998). Material properties assignment to finite element models of bone structures: a new method. Med.Eng Phys. 20, 735-740.

Appendix I: Implant positioning – radiographs versus CAD models

Femur 01R:

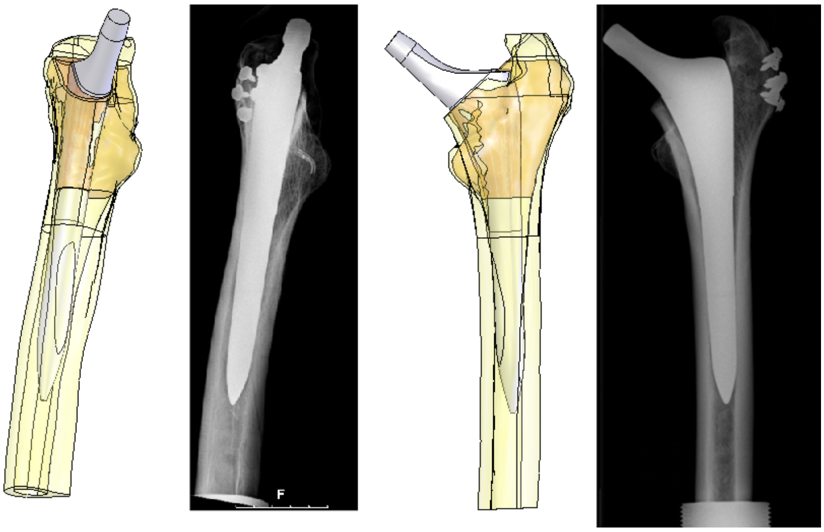

Femur 02L:

The greater trochanter on femur 02L fractured before micromotion measurement. The femur is therefore not included in the study of implant stability, but only in the study of femoral stress shielding.

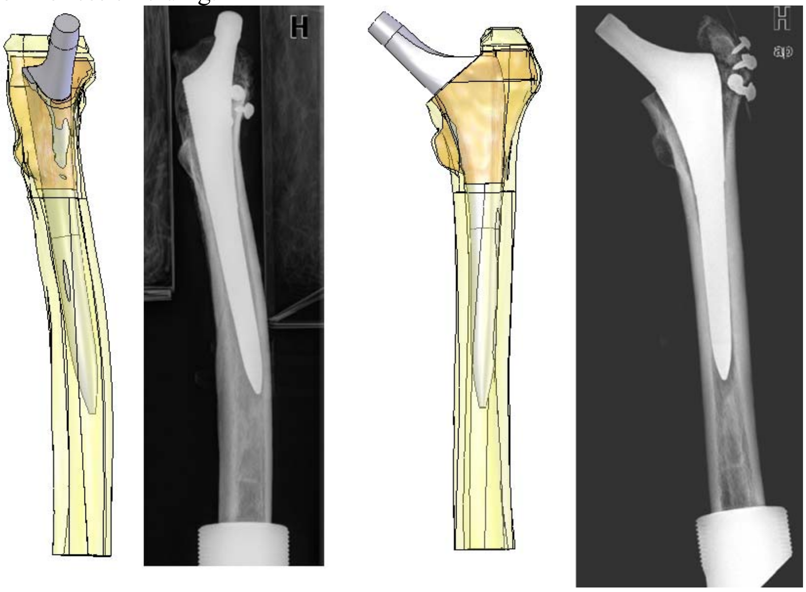

Femur 03L:

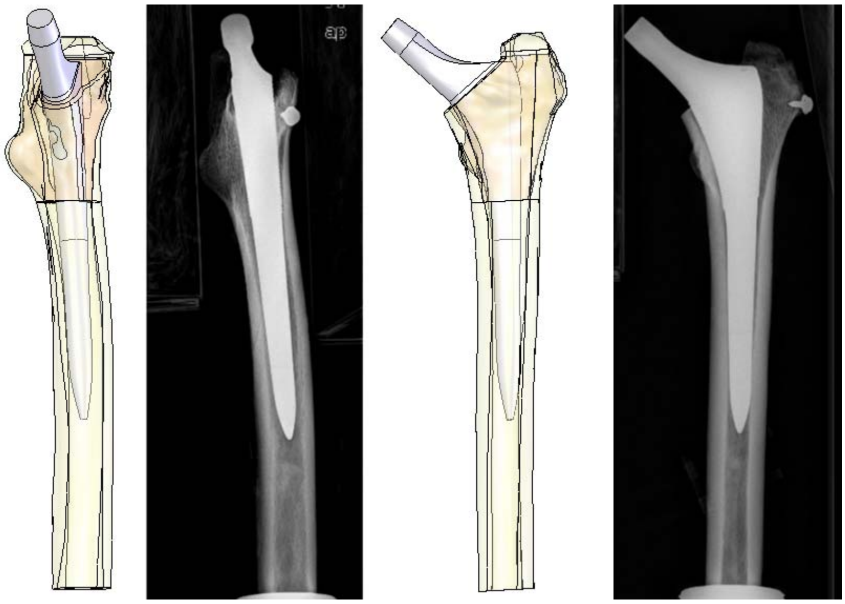

Femur 08L:

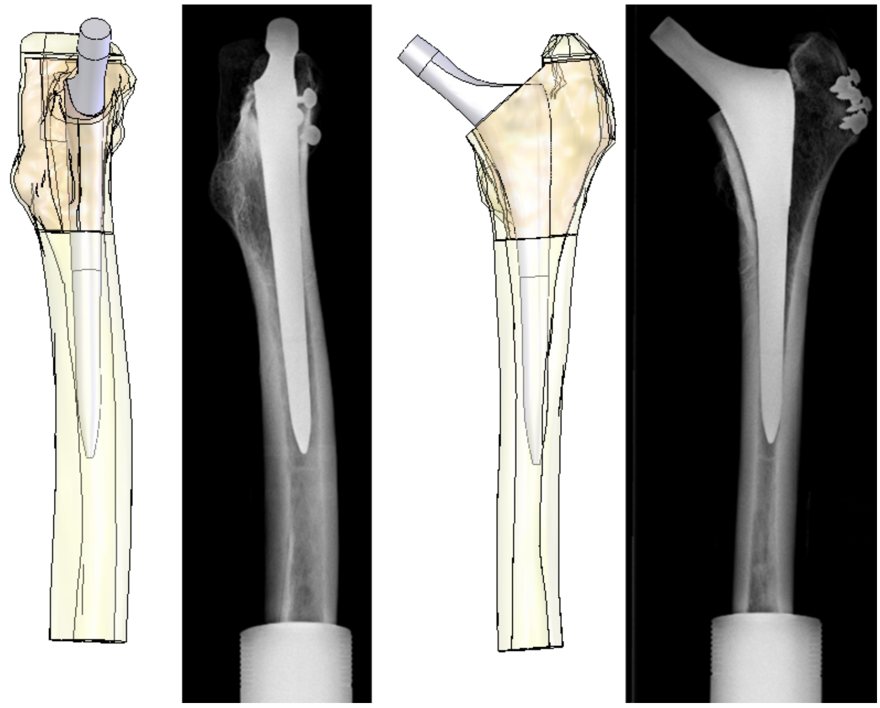

Femur 18R:

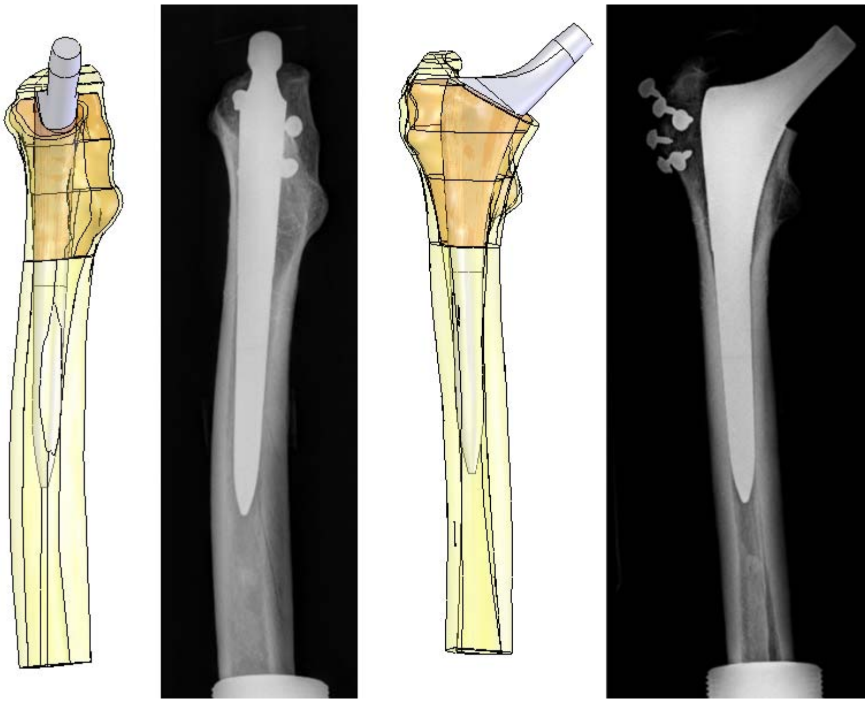

Femur 19R:

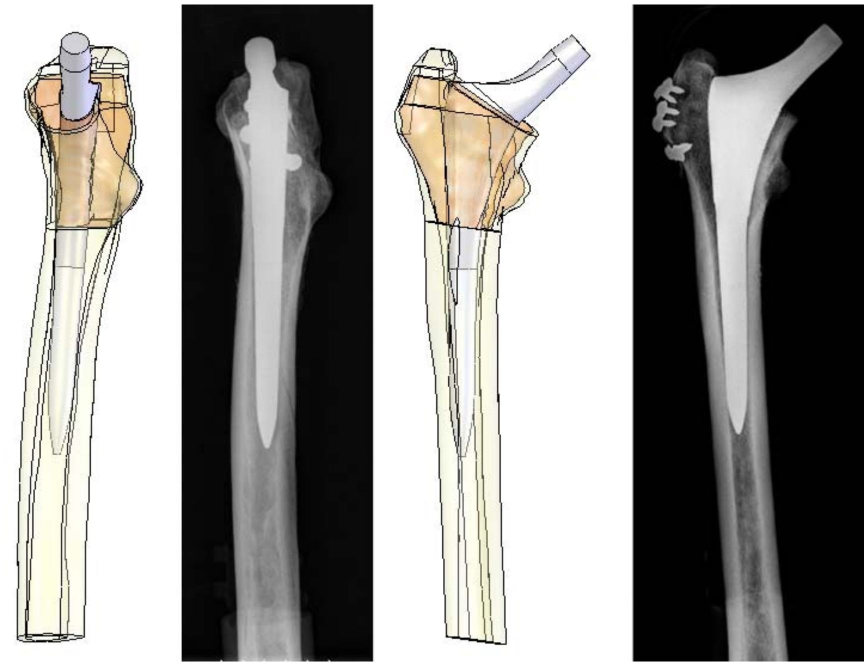

Appendix II: Post-processing FE and experimental strain

In the FE analyses, strain results of the elements associated with the strain gauges were extrapolated from the integration points to the nodes on the outer cortical surface. Strain from FE analyses is expressed according to the specified coordinate system of the elements, and does not necessarily coincide with the surface orientation of the strain gauges. In our case, the strain from the FE analyses was given according to the global coordinate system and had to be post-processed to coincide with the local coordinate system of each strain gauge.

The surface normal at each strain gauge location in the FE model was estimated from the coordinates of the strain gauge nodes. A right-hand coordinate system was defined; with the z-direction along the normal vector, y-direction in the axial and x-direction in the transverse direction of the femur (see figure A.1). By transforming the strain tensor expressed from the global to the local coordinate systems of the strain gauges it was possible to eliminate all strain components normal to the outer surface. Thus, the remaining 2x2 strain tensor expresses the surface strain of the strain gauge.

$$E_{FE,localCS} = \begin{bmatrix} - & e_x & - \\ - & e_y & - \\ - & e_z & - \end{bmatrix}_{LocalCS} \cdot E_{FE,Global} \cdot \begin{bmatrix} | & | & | \\ e_x & e_y & e_z \\ | & | & | \end{bmatrix}_{LocalCS} = \begin{bmatrix} \varepsilon_x & \frac{1}{2}\gamma_{xy} & \frac{1}{2}\gamma_{xz} \\ \frac{1}{2}\gamma_{xy} & \varepsilon_y & \frac{1}{2}\gamma_{yz} \\ \frac{1}{2}\gamma_{xz} & \frac{1}{2}\gamma_{yz} & \varepsilon_z \end{bmatrix} \quad (A.1)$$

$$\Rightarrow E_{FE,surfaceSG} = \begin{bmatrix} \varepsilon_x & \frac{1}{2}\gamma_{xy} \\ \frac{1}{2}\gamma_{xy} & \varepsilon_y \end{bmatrix} \quad (A.2)$$

Having transformed the strain of the FE analyses to the local coordinate system of the strain gauges, one can calculate the principal surface strains of the FE analyses.

$$\begin{matrix} \varepsilon_1 \\ \varepsilon_2 \end{matrix} = \frac{\varepsilon_x + \varepsilon_y}{2} \pm \sqrt{\left(\frac{\varepsilon_x + \varepsilon_y}{2}\right)^2 + \left(\frac{\gamma_{xy}}{2}\right)^2} \quad (A.3)$$

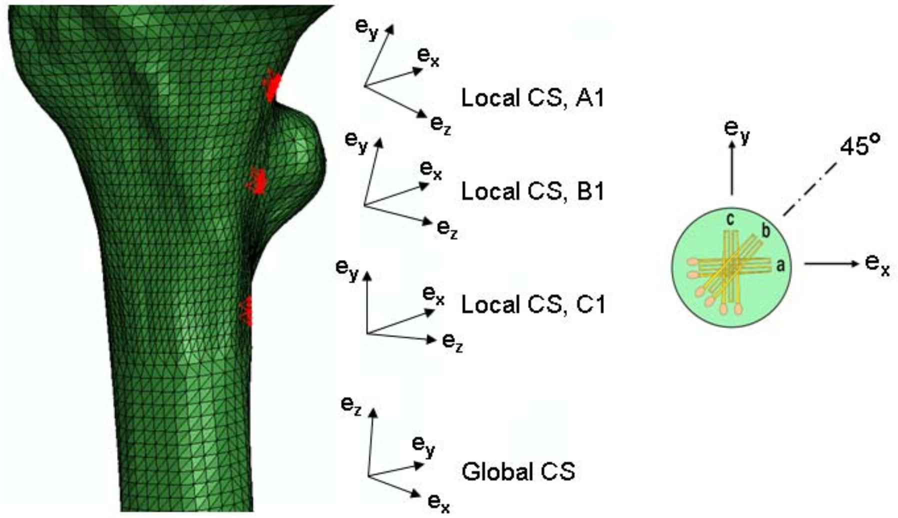

Figure A.1: The local coordinate systems (CS) of the strain gauges A1, B1 and C1 shown together with the global coordinate system of the model.

The experimental measurements of femoral strain were performed using 45°-90° strain rosettes. Thus, the principal surface strains of the strain rosettes can be calculated directly from the measurements:

$$\begin{matrix}\varepsilon_1\\ \varepsilon_2\end{matrix} = \frac{\varepsilon_a + \varepsilon_c}{2} \pm \sqrt{\frac{1}{2}\left(\varepsilon_a^{\,2} + \varepsilon_c^{\,2}\right) + \varepsilon_b \cdot \left(\varepsilon_b - \varepsilon_a - \varepsilon_c\right)} \tag{A.4}$$

It is now possible to compare the strain results of the FE analyses with the experimental strain gauge measurements.

Appendix III: Stress shielding during single leg stance

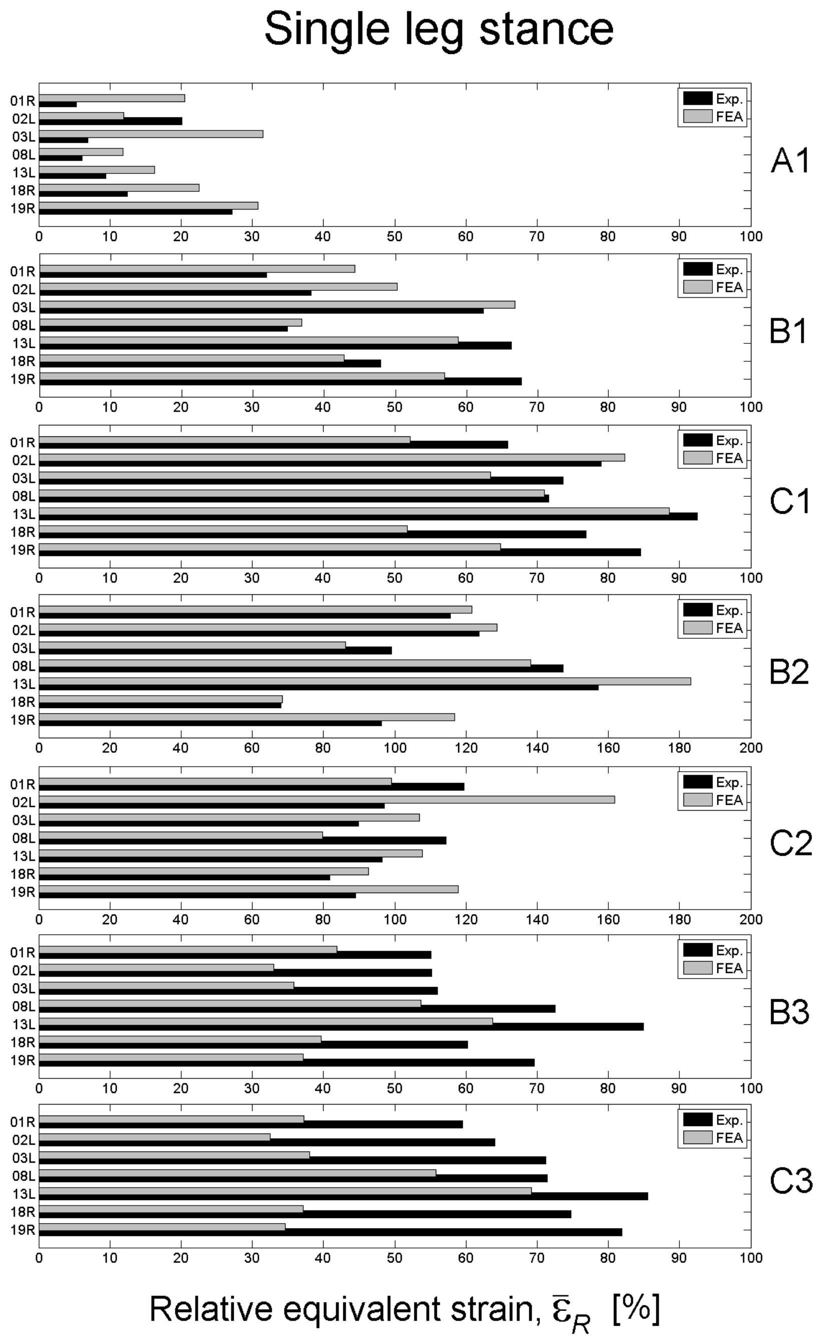

Appendix IV: Calculating experimental micromotion, translation and rotation

The fixture used to assess the stability of the stem relative to the bone, measures the displacement of ball probes A and C in the y- and z-direction, and of ball probe B in the x- and z-direction. The displacement vectors of the ball probes will be denoted as d**A**, d**B** and d**C**. The distance between the ring center and the ball probes is L/2. The coordinate system of the measuring equipment (figure 4.19) is defined differently from the coordinate system of the FE models (figure 4.21). We will therefore denote the translation derived from the experimental measurements by a superscript bar ($\bar{\mathbf{T}}$) to distinguish it from the translation according to the coordinate system of the FE models (**T**):

$$\bar{\mathbf{T}} = \begin{bmatrix} \bar{T}_x \\ \bar{T}_y \\ \bar{T}_z \end{bmatrix} = \begin{bmatrix} dB_x - \frac{1}{2}\left(dC_y - dA_y\right) \\ \frac{1}{2}\left(dA_y + dC_y\right) \\ \frac{1}{2}\left(dA_z + dC_z\right) \end{bmatrix} \tag{A.5}$$

The missing displacement components (dA_x, dB_y and dC_x) must be calculated in order to calculate the micromotion on the implant surface and the rotational angles of the implant:

$$dA_x = \bar{T}_x + \frac{1}{2}\left[L - \sqrt{L^2 - \left(dC_y - dA_y\right)^2 - \left(dC_z - dA_z\right)^2}\right] \tag{A.6}$$

$$dC_x = \bar{T}_x - \frac{1}{2}\left[L - \sqrt{L^2 - \left(dC_y - dA_y\right)^2 - \left(dC_z - dA_z\right)^2}\right] \tag{A.7}$$

$$dB_y = \bar{T}_y + \frac{1}{2}\left[L - \sqrt{L^2 - \left(dC_y - dA_y\right)^2 - \left(dC_z - dA_z\right)^2}\right] \tag{A.8}$$

The distances from the stem axis and out to the points P_A, P_B and P_C on the stem surface (figure 4.20) are measured at the distal and proximal measuring levels with a slide calliper. The setup used in the present study, measures the relative motion between the ring attached to outer cortical bone and yoke attached to the shoulder of the implant. The micromotion vector ($\mathbf{m}_A$, $\mathbf{m}_B$ and $\mathbf{m}_C$) on the implant surface can be determined by interpolation using the translation **T** at the center of the ring, the spatial displacements (d**A**, d**B** and d**C**) at the ball probes, and the distances P_A, P_B and P_C:

$$\mathbf{m}_A = \overline{\mathbf{T}} \cdot \left(\frac{L - 2 \cdot P_A}{L} \right) + d\mathbf{A} \cdot \left(\frac{2 \cdot P_A}{L} \right) \tag{A.9}$$

$$\mathbf{m}_B = \overline{\mathbf{T}} \cdot \left(\frac{L - 2 \cdot P_B}{L} \right) + d\mathbf{B} \cdot \left(\frac{2 \cdot P_B}{L} \right) \tag{A.10}$$

$$\mathbf{m}_C = \overline{\mathbf{T}} \cdot \left(\frac{L - 2 \cdot P_C}{L} \right) + d\mathbf{C} \cdot \left(\frac{2 \cdot P_C}{L} \right) \tag{A.11}$$

The magnitude of micromotion, as shown in figure 4.23, is the length of the spatial micromotion vectors (Δm) between unloaded state (*step* = 3, 6, 9 and 12) and stairclimbing (*step* = 5, 8, 11, 14):

$$\Delta m_A = \frac{1}{4} \cdot \sum_{step=i} \sqrt{\left(m_{Ax,step=i} - m_{Ax,step=i-2} \right)^2 + \left(m_{Ay,step=i} - m_{Ay,step=i-2} \right)^2 + \left(m_{Az,step=i} - m_{Az,step=i-2} \right)^2}$$

for i = 5, 8, 11 and 14

(A.12)

Equation (A.12) shows the calculation of micromotion (Δm_A) between implant and bone in P_A. The same calculation was performed for Δm_B and Δm_C.

Small rotational angles are assumed in order to simplify the calculation of the relative rotations between stem and bone:

$$\alpha = \frac{180^\circ}{\pi} \cdot \left[\frac{1}{L} \cdot \left(dA_Z + dC_Z - 2 \cdot dB_Z \right) \right] \tag{A.13}$$

$$\beta = \frac{180^\circ}{\pi} \cdot \left[\frac{1}{L} \cdot \left(dA_Z - dC_Z \right) \right] \tag{A.14}$$

$$\gamma = \frac{180^\circ}{\pi} \cdot \left[\frac{1}{L} \cdot \left(dC_Y - dA_Y \right) \right] \tag{A.15}$$

The angles α, β and γ are the rotational angles about the x-, y- and z-axis as defined by the coordinate system of the measuring equipment. The translations and rotational angles are then sorted according to the coordinate system of the FE model.

$$\mathbf{T} = \begin{bmatrix} T_x \\ T_y \\ T_z \end{bmatrix} = \begin{bmatrix} \overline{T}_y \\ \overline{T}_x \\ \overline{T}_z \end{bmatrix} \tag{A.16}$$

$$\boldsymbol{\theta} = \begin{bmatrix} \theta_x \\ \theta_y \\ \theta_z \end{bmatrix} = \begin{bmatrix} \beta \\ \alpha \\ \gamma \end{bmatrix} \qquad \text{(A.17)}$$

Axial translation (ΔT_z) as was calculated between unloaded state (*step* = 3, 6, 9 and 12) and stairclimbing (*step* = 5, 8, 11 and 14), while axial rotation ($\Delta\theta_z$) during torsional load was calculated between single leg stance (*step* = 4, 7, 10 and 13) and stairclimbing (*step* = 5, 8, 11 and 14):

$$\Delta T_z = \frac{1}{4} \cdot \sum_{step=i} T_{z,i} - T_{z,i-2} \text{ , for } i = 5, 8, 11, \text{ and } 14 \qquad \text{(A.18)}$$

$$\Delta \theta_z = \frac{1}{4} \cdot \sum_{step=i} \theta_{z,i} - \theta_{z,i-1} \text{ , for } i = 5, 8, 11, \text{ and } 14 \qquad \text{(A.19)}$$

Appendix V: Decomposition of FE node displacements into translation and rotation

The coordinates (**X**) and displacements (**u**) of the node sets on the implant-bone interface are used to decompose the relative movement between the two into translation (**T**) and rotation (**Q**). The procedure requires that the coordinate centers of the node sets coincide at each level. In the FE models used in the present study, the mesh on the cavity surface matched the mesh on the implant. The coordinate center of the cavity nodes was therefore perfectly coincident with the center of the implant nodes. **X** and **u** are 3 by *m* matrices, where *m* is the number of nodes in the particular node set. Since the femur is tilted 12° in valgus in the FE model, the coordinate system must be rotated 12° about the y-axis to upright position so that z-axis aligns with the axial direction of the implant (figure 4.21):

$$\tilde{\mathbf{X}}^{NS}_{step=0} = \begin{bmatrix} \cos(12°) & 0 & \sin(12°) \\ 0 & 1 & 0 \\ -\sin(12°) & 0 & \cos(12°) \end{bmatrix} \cdot \mathbf{X}^{NS}_{step=0} \qquad \text{(A.20)}$$

$$\tilde{\mathbf{u}}^{NS}_{step=i} = \begin{bmatrix} \cos(12°) & 0 & \sin(12°) \\ 0 & 1 & 0 \\ -\sin(12°) & 0 & \cos(12°) \end{bmatrix} \cdot \mathbf{u}^{NS}_{step=i} \qquad \text{(A.21)}$$

The superscript *NS* refers to the label of the node sets (for example cavity nodes on the proximal level, or implant nodes on the distal level), and the subscript *step* refers to the load step of the analysis (*step* = 0 refers to the initial node coordinates of the FE model). The relative translation between the implant and cavity can be calculated directly from their displacements:

$$\mathbf{T}_{step=i} = \begin{bmatrix} T_x \\ T_y \\ T_z \end{bmatrix}_{step=i} = mean(\tilde{\mathbf{u}}^{Implant}_{step=i}) - mean(\tilde{\mathbf{u}}^{Cavity}_{step=i}) \qquad \text{(A.22)}$$

The axial translation (T_z), as plotted in figure 4.22, is the z-component of **T** in equation (A.22). The axial translation (ΔT_z), as plotted in figure 4.24, is calculated from the unloaded step to stairclimbing (step 3 and step 5):

$$\Delta\mathbf{T} = \mathbf{T}_{step=5} - \mathbf{T}_{step=3} = \begin{bmatrix} \Delta T_x \\ \Delta T_y \\ \Delta T_z \end{bmatrix} \tag{A.23}$$

In order to calculate the rotational angles of the implant relative to the cavity surface, the rotational matrix (**Q**) of each node set must be determined for every load step. First, the displaced node coordinates at each load step are calculated:

$$\tilde{\mathbf{X}}^{NS}_{step=i} = \tilde{\mathbf{X}}^{NS}_{step=0} + \tilde{\mathbf{u}}^{NS}_{step=i} \tag{A.24}$$

The displaced node coordinates are then expressed relative to their midpoint:

$$\overline{\mathbf{X}}^{NS}_{step=i} = \tilde{\mathbf{X}}^{NS}_{step=i} - mean(\tilde{\mathbf{X}}^{NS}_{step=i}) \tag{A.25}$$

The rotational matrix between the initial and displaced node coordinates is determined using the *mrdivide* function in MATLAB 7.1:

$$\mathbf{Q}^{NS}_{step=i} = mrdivide(\overline{\mathbf{X}}^{NS}_{step=i}, \overline{\mathbf{X}}^{NS}_{step=0}) \tag{A.26}$$

Since the *mrdivide* function gives a numerical approximation of the rotational matrix (**Q**), the matrix will not be perfectly orthogonal. The matrix is therefore adjusted to make it orthogonal and with a determinant equal to one.

$$\mathbf{Q}(1,:)^{NS}_{step=i} = \mathbf{Q}(2,:)^{NS}_{step=i} \times \mathbf{Q}(3,:)^{NS}_{step=i} \tag{A.27}$$

$$\mathbf{Q}(2,:)^{NS}_{step=i} = \mathbf{Q}(3,:)^{NS}_{step=i} \times \mathbf{Q}(1,:)^{NS}_{step=i} \tag{A.28}$$

$$\mathbf{Q}(3,:)^{NS}_{step=i} = \mathbf{Q}(1,:)^{NS}_{step=i} \times \mathbf{Q}(2,:)^{NS}_{step=i} \tag{A.29}$$

```
for $j$ = 1:3
    $\mathbf{Q}(j,:)^{NS}_{step=i} = \mathbf{Q}(j,:)^{NS}_{step=i} \Big/ \left|\mathbf{Q}(j,:)^{NS}_{step=i}\right|$        (A.30)
end
```

We define the rotational matrix as the product of three sequential rotations; about the z-, y- and x-axis, respectively:

$$\mathbf{Q} = \mathbf{R}_x \cdot \mathbf{R}_y \cdot \mathbf{R}_z = \begin{bmatrix} 1 & 0 & 0 \\ 0 & c_x & -s_x \\ 0 & s_x & c_x \end{bmatrix} \cdot \begin{bmatrix} c_y & 0 & s_y \\ 0 & 1 & 0 \\ -s_y & 0 & c_y \end{bmatrix} \cdot \begin{bmatrix} c_z & -s_z & 0 \\ s_z & c_z & 0 \\ 0 & 0 & 1 \end{bmatrix} \tag{A.31}$$

$$\Rightarrow \mathbf{Q} = \begin{bmatrix} c_y \cdot c_z & -c_y \cdot s_z & s_y \\ s_x \cdot s_y \cdot c_z + c_x \cdot s_z & -s_x \cdot s_y \cdot s_z + c_x \cdot c_z & -s_x \cdot c_y \\ -c_x \cdot s_y \cdot c_z + s_x \cdot s_z & c_x \cdot s_y \cdot s_z + s_x \cdot c_z & c_x \cdot c_y \end{bmatrix} \tag{A.32}$$

where *s* and *c* denote the sines and cosines of the rotations about the x-, y-, and z-axis. The angles are determined from the rotational matrix **Q**:

$$\beta_{step=i}^{NS} = \arcsin(\mathbf{Q}(1,3)_{step=i}^{NS}) \tag{A.33}$$

$$\gamma_{step=i}^{NS} = -\arcsin\left(\frac{\mathbf{Q}(1,2)_{step=i}^{NS}}{\cos \beta_{step=i}^{NS}}\right) \tag{A.34}$$

$$\alpha_{step=i}^{NS} = -\arcsin\left(\frac{\mathbf{Q}(2,3)_{step=i}^{NS}}{\cos \beta_{step=i}^{NS}}\right) \tag{A.35}$$

The angles α, β and γ refer to the rotations about the x-, y- and z-axis, respectively. The relative rotation between the implant and the femoral cavity are then calculated:

$$\boldsymbol{\theta} = \begin{bmatrix} \alpha \\ \beta \\ \gamma \end{bmatrix}_{step=i}^{Implant} - \begin{bmatrix} \alpha \\ \beta \\ \gamma \end{bmatrix}_{step=i}^{Cavity} = \begin{bmatrix} \theta_x \\ \theta_y \\ \theta_z \end{bmatrix}_{step=i} \tag{A.36}$$

The axial rotation (θ_z), as plotted in figure 4.22, is the z-component of $\boldsymbol{\theta}$ in equation (A.36). The axial rotation during torsional load ($\Delta\theta_z$), as plotted in figure 4.23, is calculated from single leg stance to stairclimbing (step 4 and step 5):

$$\Delta\boldsymbol{\theta} = \boldsymbol{\theta}_{step=5} - \boldsymbol{\theta}_{step=4} = \begin{bmatrix} \Delta\theta_x \\ \Delta\theta_y \\ \Delta\theta_z \end{bmatrix} \tag{A.37}$$

"Reliability Analysis of Structural Systems using Nonlinear Finite Element Methods",
C. A. Holm, 1990:23, ISBN 82-7119-178-0.

"Uniform Stratified Flow Interaction with a Submerged Horizontal Cylinder",
Ø. Arntsen, 1990:32, ISBN 82-7119-188-8.

"Large Displacement Analysis of Flexible and Rigid Systems Considering Displacement-Dependent Loads and Nonlinear Constraints", K. M. Mathisen, 1990:33, ISBN 82-7119-189-6.

"Solid Mechanics and Material Models including Large Deformations",
E. Levold, 1990:56, ISBN 82-7119-214-0, ISSN 0802-3271.

"Inelastic Deformation Capacity of Flexurally-Loaded Aluminium Alloy Structures",
T. Welo, 1990:62, ISBN 82-7119-220-5, ISSN 0802-3271.

"Visualization of Results from Mechanical Engineering Analysis",
K. Aamnes, 1990:63, ISBN 82-7119-221-3, ISSN 0802-3271.

"Object-Oriented Product Modeling for Structural Design",
S. I. Dale, 1991:6, ISBN 82-7119-258-2, ISSN 0802-3271.

"Parallel Techniques for Solving Finite Element Problems on Transputer Networks",
T. H. Hansen, 1991:19, ISBN 82-7119-273-6, ISSN 0802-3271.

"Statistical Description and Estimation of Ocean Drift Ice Environments",
R. Korsnes, 1991:24, ISBN 82-7119-278-7, ISSN 0802-3271.

“Properties of concrete related to fatigue damage: with emphasis on high strength concrete”,
G. Petkovic, 1991:35, ISBN 82-7119-290-6, ISSN 0802-3271.

"Turbidity Current Modelling",
B. Brørs, 1991:38, ISBN 82-7119-293-0, ISSN 0802-3271.

"Zero-Slump Concrete: Rheology, Degree of Compaction and Strength. Effects of Fillers as Part Cement-Replacement",
C. Sørensen, 1992:8, ISBN 82-7119-357-0, ISSN 0802-3271.

"Nonlinear Analysis of Reinforced Concrete Structures Exposed to Transient Loading",
K. V. Høiseth, 1992:15, ISBN 82-7119-364-3, ISSN 0802-3271.

"Finite Element Formulations and Solution Algorithms for Buckling and Collapse Analysis of Thin Shells", R. O. Bjærum, 1992:30, ISBN 82-7119-380-5, ISSN 0802-3271.

"Response Statistics of Nonlinear Dynamic Systems",
J. M. Johnsen, 1992:42, ISBN 82-7119-393-7, ISSN 0802-3271.

"Digital Models in Engineering. A Study on why and how engineers build and operate digital models for decisison support", J. Høyte, 1992:75, ISBN 82-7119-429-1, ISSN 0802-3271.

"Sparse Solution of Finite Element Equations",
A. C. Damhaug, 1992:76, ISBN 82-7119-430-5, ISSN 0802-3271.

"Some Aspects of Floating Ice Related to Sea Surface Operations in the Barents Sea",
S. Løset, 1992:95, ISBN 82-7119-452-6, ISSN 0802-3271.

"Modelling of Cyclic Plasticity with Application to Steel and Aluminium Structures",
O. S. Hopperstad, 1993:7, ISBN 82-7119-461-5, ISSN 0802-3271.

"The Free Formulation: Linear Theory and Extensions with Applications to Tetrahedral Elements with Rotational Freedoms", G. Skeie, 1993:17, ISBN 82-7119-472-0, ISSN 0802-3271.

"Høyfast betongs motstand mot piggdekkslitasje. Analyse av resultater fra prøving i Veisliter'n",
T. Tveter, 1993:62, ISBN 82-7119-522-0, ISSN 0802-3271.

"A Nonlinear Finite Element Based on Free Formulation Theory for Analysis of Sandwich Structures", O. Aamlid, 1993:72, ISBN 82-7119-534-4, ISSN 0802-3271.

"The Effect of Curing Temperature and Silica Fume on Chloride Migration and Pore Structure of High Strength Concrete", C. J. Hauck, 1993:90, ISBN 82-7119-553-0, ISSN 0802-3271.

"Failure of Concrete under Compressive Strain Gradients",
G. Markeset, 1993:110, ISBN 82-7119-575-1, ISSN 0802-3271.

"An experimental study of internal tidal amphidromes in Vestfjorden",
J. H. Nilsen, 1994:39, ISBN 82-7119-640-5, ISSN 0802-3271.

"Structural analysis of oil wells with emphasis on conductor design",
H. Larsen, 1994:46, ISBN 82-7119-648-0, ISSN 0802-3271.

"Adaptive methods for non-linear finite element analysis of shell structures",
K. M. Okstad, 1994:66, ISBN 82-7119-670-7, ISSN 0802-3271.

"On constitutive modelling in nonlinear analysis of concrete structures",
O. Fyrileiv, 1994:115, ISBN 82-7119-725-8, ISSN 0802-3271.

"Fluctuating wind load and response of a line-like engineering structure with emphasis on motion-induced wind forces",
J. Bogunovic Jakobsen, 1995:62, ISBN 82-7119-809-2, ISSN 0802-3271.

"An experimental study of beam-columns subjected to combined torsion, bending and axial actions", A. Aalberg, 1995:66, ISBN 82-7119-813-0, ISSN 0802-3271.

"Scaling and cracking in unsealed freeze/thaw testing of Portland cement and silica fume concretes", S. Jacobsen, 1995:101, ISBN 82-7119-851-3, ISSN 0802-3271.

"Damping of water waves by submerged vegetation. A case study of laminaria hyperborea",
A. M. Dubi, 1995:108, ISBN 82-7119-859-9, ISSN 0802-3271.

"The dynamics of a slope current in the Barents Sea",
Sheng Li, 1995:109, ISBN 82-7119-860-2, ISSN 0802-3271.

"Modellering av delmaterialenes betydning for betongens konsistens",
Ernst Mørtsell, 1996:12, ISBN 82-7119-894-7, ISSN 0802-3271.

"Bending of thin-walled aluminium extrusions",
Birgit Søvik Opheim, 1996:60, ISBN 82-7119-947-1, ISSN 0802-3271.

"Material modelling of aluminium for crashworthiness analysis",
Torodd Berstad, 1996:89, ISBN 82-7119-980-3, ISSN 0802-3271.

"Estimation of structural parameters from response measurements on submerged floating tunnels",
Rolf Magne Larssen, 1996:119, ISBN 82-471-0014-2, ISSN 0802-3271.

“Numerical modelling of plain and reinforced concrete by damage mechanics”,
Mario A. Polanco-Loria, 1997:20, ISBN 82-471-0049-5, ISSN 0802-3271.

“Nonlinear random vibrations - numerical analysis by path integration methods”,
Vibeke Moe, 1997:26, ISBN 82-471-0056-8, ISSN 0802-3271.

“Numerical prediction of vortex-induced vibration by the finite element method”,
Joar Martin Dalheim, 1997:63, ISBN 82-471-0096-7, ISSN 0802-3271.

“Time domain calculations of buffeting response for wind sensitive structures”,
Ketil Aas-Jakobsen, 1997:148, ISBN 82-471-0189-0, ISSN 0802-3271.

"A numerical study of flow about fixed and flexibly mounted circular cylinders",
Trond Stokka Meling, 1998:48, ISBN 82-471-0244-7, ISSN 0802-3271.

“Estimation of chloride penetration into concrete bridges in coastal areas”,
Per Egil Steen, 1998:89, ISBN 82-471-0290-0, ISSN 0802-3271.

“Stress-resultant material models for reinforced concrete plates and shells”,
Jan Arve Øverli, 1998:95, ISBN 82-471-0297-8, ISSN 0802-3271.

“Chloride binding in concrete. Effect of surrounding environment and concrete composition”,
Claus Kenneth Larsen, 1998:101, ISBN 82-471-0337-0, ISSN 0802-3271.

“Rotational capacity of aluminium alloy beams”,
Lars A. Moen, 1999:1, ISBN 82-471-0365-6, ISSN 0802-3271.

“Stretch Bending of Aluminium Extrusions”,
Arild H. Clausen, 1999:29, ISBN 82-471-0396-6, ISSN 0802-3271.

“Aluminium and Steel Beams under Concentrated Loading”,
Tore Tryland, 1999:30, ISBN 82-471-0397-4, ISSN 0802-3271.

"Engineering Models of Elastoplasticity and Fracture for Aluminium Alloys",
Odd-Geir Lademo, 1999:39, ISBN 82-471-0406-7, ISSN 0802-3271.

"Kapasitet og duktilitet av dybelforbindelser i trekonstruksjoner",
Jan Siem, 1999:46, ISBN 82-471-0414-8, ISSN 0802-3271.

“Etablering av distribuert ingeniørarbeid; Teknologiske og organisatoriske erfaringer fra en norsk ingeniørbedrift”, Lars Line, 1999:52, ISBN 82-471-0420-2, ISSN 0802-3271.

“Estimation of Earthquake-Induced Response”, Símon Ólafsson, 1999:73, ISBN 82-471-0443-1, ISSN 0802-3271.

“Coastal Concrete Bridges: Moisture State, Chloride Permeability and Aging Effects”
Ragnhild Holen Relling, 1999:74, ISBN 82-471-0445-8, ISSN 0802-3271.

”Capacity Assessment of Titanium Pipes Subjected to Bending and External Pressure”,
Arve Bjørset, 1999:100, ISBN 82-471-0473-3, ISSN 0802-3271.

“Validation of Numerical Collapse Behaviour of Thin-Walled Corrugated Panels”,
Håvar Ilstad, 1999:101, ISBN 82-471-0474-1, ISSN 0802-3271.

“Strength and Ductility of Welded Structures in Aluminium Alloys”,
Miroslaw Matusiak, 1999:113, ISBN 82-471-0487-3, ISSN 0802-3271.

“Thermal Dilation and Autogenous Deformation as Driving Forces to Self-Induced Stresses in High Performance Concrete”,
Øyvind Bjøntegaard, 1999:121, ISBN 82-7984-002-8, ISSN 0802-3271.

“Some Aspects of Ski Base Sliding Friction and Ski Base Structure”,
Dag Anders Moldestad, 1999:137, ISBN 82-7984-019-2, ISSN 0802-3271.

"Electrode reactions and corrosion resistance for steel in mortar and concrete",
Roy Antonsen, 2000:10, ISBN 82-7984-030-3, ISSN 0802-3271.

"Hydro-Physical Conditions in Kelp Forests and the Effect on Wave Damping and Dune Erosion. A case study on Laminaria Hyperborea",
Stig Magnar Løvås, 2000:28, ISBN 82-7984-050-8, ISSN 0802-3271.

"Random Vibration and the Path Integral Method",
Christian Skaug, 2000:39, ISBN 82-7984-061-3, ISSN 0802-3271.

"Buckling and geometrical nonlinear beam-type analyses of timber structures",
Trond Even Eggen, 2000:56, ISBN 82-7984-081-8, ISSN 0802-3271.

”Structural Crashworthiness of Aluminium Foam-Based Components”,
Arve Grønsund Hanssen, 2000:76, ISBN 82-7984-102-4, ISSN 0809-103X.

“Measurements and simulations of the consolidation in first-year sea ice ridges, and some aspects of mechanical behaviour”, Knut V. Høyland, 2000:94, ISBN 82-7984-121-0, ISSN 0809-103X.

”Kinematics in Regular and Irregular Waves based on a Lagrangian Formulation”,
Svein Helge Gjøsund, 2000-86, ISBN 82-7984-112-1, ISSN 0809-103X.

”Self-Induced Cracking Problems in Hardening Concrete Structures”,
Daniela Bosnjak, 2000-121, ISBN 82-7984-151-2, ISSN 0809-103X.

"Ballistic Penetration and Perforation of Steel Plates",
Tore Børvik, 2000:124, ISBN 82-7984-154-7, ISSN 0809-103X.

"Freeze-Thaw resistance of Concrete. Effect of: Curing Conditions, Moisture Exchange and Materials", Terje Finnerup Rønning, 2001:14, ISBN 82-7984-165-2, ISSN 0809-103X

Structural behaviour of post tensioned concrete structures. Flat slab. Slabs on ground",
Steinar Trygstad, 2001:52, ISBN 82-471-5314-9, ISSN 0809-103X.

"Slipforming of Vertical Concrete Structures. Friction between concrete and slipform panel", Kjell Tore Fosså, 2001:61, ISBN 82-471-5325-4, ISSN 0809-103X.

"Some numerical methods for the simulation of laminar and turbulent incompressible flows", Jens Holmen, 2002:6, ISBN 82-471-5396-3, ISSN 0809-103X.

“Improved Fatigue Performance of Threaded Drillstring Connections by Cold Rolling”, Steinar Kristoffersen, 2002:11, ISBN: 82-421-5402-1, ISSN 0809-103X.

"Deformations in Concrete Cantilever Bridges: Observations and Theoretical Modelling", Peter F. Takâcs, 2002:23, ISBN 82-471-5415-3, ISSN 0809-103X.

"Stiffened aluminium plates subjected to impact loading", Hilde Giæver Hildrum, 2002:69, ISBN 82-471-5467-6, ISSN 0809-103X.

"Full- and model scale study of wind effects on a medium-rise building in a built up area", Jónas Thór Snæbjørnsson, 2002:95, ISBN82-471-5495-1, ISSN 0809-103X.

“Evaluation of Concepts for Loading of Hydrocarbons in Ice-infested water”, Arnor Jensen, 2002:114, ISBN 82-417-5506-0, ISSN 0809-103X.

”Numerical and Physical Modelling of Oil Spreading in Broken Ice”, Janne K. Økland Gjøsteen, 2002:130, ISBN 82-471-5523-0, ISSN 0809-103X.

”Diagnosis and protection of corroding steel in concrete”, Franz Pruckner, 20002:140, ISBN 82-471-5555-4, ISSN 0809-103X.

“Tensile and Compressive Creep of Young Concrete: Testing and Modelling”, Dawood Atrushi, 2003:17, ISBN 82-471-5565-6, ISSN 0809-103X.

“Rheology of Particle Suspensions. Fresh Concrete, Mortar and Cement Paste with Various Types of Lignosulfonates”, Jon Elvar Wallevik, 2003:18, ISBN 82-471-5566-4, ISSN 0809-103X.

“Oblique Loading of Aluminium Crash Components”, Aase Reyes, 2003:15, ISBN 82-471-5562-1, ISSN 0809-103X.

“Utilization of Ethiopian Natural Pozzolans”, Surafel Ketema Desta, 2003:26, ISSN 82-471-5574-5, ISSN:0809-103X.

“Behaviour and strength prediction of reinforced concrete structures with discontinuity regions”, Helge Brå, 2004:11, ISBN 82-471-6222-9, ISSN 1503-8181.

“High-strength steel plates subjected to projectile impact. An experimental and numerical study”, Sumita Dey, 2004:38, ISBN 82-471-6281-4 (elektr. Utg.), ISBN 82-471-6282-2 (trykt utg.), ISSN 1503-8181.

“Alkali-reactive and inert fillers in concrete. Rheology of fresh mixtures and expansive reactions.” Bård M. Pedersen, 2004:92, ISBN 82-471-6401-9 (trykt utg.), ISBN 82-471-6400-0 (elektr. utg.), ISSN 1503-8181.

“On the Shear Capacity of Steel Girders with Large Web Openings”. Nils Christian Hagen, 2005:9 ISBN 82-471-6878-2 (trykt utg.), ISBN 82-471-6877-4 (elektr. utg.), ISSN 1503-8181.

”Behaviour of aluminium extrusions subjected to axial loading”. Østen Jensen, 2005:7, ISBN 82-471-6872-3 (elektr. utg.) , ISBN 82-471-6873-1 (trykt utg.), ISSN 1503-8181.

”Thermal Aspects of corrosion of Steel in Concrete”. Jan-Magnus Østvik, 2005:5, ISBN 82-471-6869-3 (trykt utg.) ISBN 82-471-6868 (elektr.utg), ISSN 1503-8181.

”Mechanical and adaptive behaviour of bone in relation to hip replacement.” A study of bone remodelling and bone grafting. Sébastien Muller, 2005:34, ISBN 82-471-6933-9 (trykt utg.) (ISBN 82-471-6932-0 (elektr.utg), ISSN 1503-8181.

“Analysis of geometrical nonlinearities with applications to timber structures”. Lars Wollebæk, 2005:74, ISBN 82-471-7050-5 (trykt utg.), ISBN 82-471-7019-1 (elektr. Utg.), ISSN 1503-8181.

“Pedestrian induced lateral vibrations of slender footbridges”, Anders Rönnquist, 2005:102, ISBN 82-471-7082-5 (trykt utg.), ISBN 82-471-7081-7 (elektr.utg.), ISSN 1503-8181.

“Initial Strength Development of Fly Ash and Limestone Blended Cements at Various Temperatures Predicted by Ultrasonic Pulse Velocity”, Tom Ivar Fredvik, 2005:112, ISBN 82-471-7105-8 (trykt utg.), ISBN 82-471-7103-1 (elektr.utg.), ISSN 1503-8181.

“Behaviour and modelling of thin-walled cast components”, Cato Dørum, 2005:128, ISBN 82-471-7140-6 (trykt utg.), ISBN 82-471-7139-2 (elektr. utg.), ISSN 1503-8181.

“Behaviour and modelling of selfpiercing riveted connections”, Raffaele Porcaro, 2005:165, ISBN 82-471-7219-4 (trykt utg.), ISBN 82-471-7218-6 (elektr.utg.), ISSN 1503-8181.

”Behaviour and Modelling og Aluminium Plates subjected to Compressive Load”, Lars Rønning, 2005:154, ISBN 82-471-7169-1 (trykt utg.), ISBN 82-471-7195-3 (elektr.utg.), ISSN 1503-8181

”Bumper beam-longitudinal system subjected to offset impact loading”, Satyanarayana Kokkula, 2005:193, ISBN 82-471-7280-1 (trykt utg.), ISBN 82-471-7279-8 (elektr.utg.), ISSN 1503-8181.

“Control of Chloride Penetration into Concrete Structures at Early Age”, Guofei Liu, 2006:46, ISBN 82-471-7838-9 (trykt utg.), ISBN 82-471-7837-0 (elektr. utgave), ISSN 1503-8181.

“Modelling of Welded Thin-Walled Aluminium Structures”, Ting Wang, 2006:78, ISBN 82-471-7907-5 (trykt utg.), ISBN 82-471-7906-7 (elektr.utg.), ISSN 1503-8181.

”Time-variant reliability of dynamic systems by importance sampling and probabilistic analysis of ice loads”, Anna Ivanova Olsen, 2006:139, ISBN 82-471-8041-3 (trykt utg.), ISBN 82-471-8040-5 (elektr.utg.), ISSN 1503-8181.

“Fatigue life prediction of an aluminium alloy automotive component using finite element analysis of surface topography”. Sigmund Kyrre Ås, 2006:25, ISBN 82-471-7791-9 (trykt utg.), ISBN 82-471-7791-9 (elektr.utg.), ISSN 1503-8181.

”Constitutive models of elastoplasticity and fracture for aluminium alloys under strain path change”, Dasharatha Achani, 2006:76, ISBN 82-471-7903-2 (trykt utg.), ISBN 82-471-7902-4 (elektr.utg.), ISSN 1503-8181.
“Simulations of 2D dynamic brittle fracture by the Element-free Galerkin method and linear fracture mechanics”, Tommy Karlsson, 2006:125, ISBN 82-471-8011-1 (trykt utg.), ISBN 82-471-8010-3 (elektr.utg.), ISSN 1503-8181.

“Penetration and Perforation of Granite Targets by Hard Projectiles”, Chong Chiang Seah, 2006:188, ISBN 82-471-8150-9 (printed ver.), ISBN 82-471-8149-5 (electronic ver.) ISSN 1503-8181.

“Deformations, strain capacity and cracking of concrete in plastic and early hardening phases”, Tor Arne Hammer, 2007:234, ISBN 978-82-471-5191-4 (trykt utg.), ISBN 978-82-471-5207-2 (elektr.utg.) ISSN 1503-8181.

“Crashworthiness of dual-phase high-strength steel: Material and Component behaviour”, Venkatapathi Tarigopula, 2007:230, ISBN 82-471-5076-4 (trykt utg.) ISBN 82-471-5093-1 (elektr.utg.) ISSN 1503-8181.

“Fibre reinforcement in load carrying concrete structures”, Åse Lyslo Døssland, 2008:50, ISBN 978-82-471-6910-0 (trykt utg.), ISBN 978-82-471-6924-7 (elektr.utg.), ISSN 1503-8181.

“Low-velocity penetration of aluminium plates”, Frode Grytten, 2008:46, ISBN 978-82-471-6826-4 (trykt utg.) ISBN 978-82-471-6843-1 (elektr. Utg.) ISSN 1503-8181.

“Robustness studies of structures subjected to large deformations”, Ørjan Fylling, 2008:24, ISBN 978-82-471-6339-9 (trykt utg.) ISBN 978-82-471-6342-9 (elektro.utg.) ISSN 1503-8181.

“Constitutive modelling of morsellised bone”,Knut Birger Lunde, 2008:92, ISBN 978-82-471-7829-4 (trykt utg.) ISBN 978-82-471-7832-4 (elektro.utg.) ISSN 1503-8181.

“Experimental Investigations of Wind Loading on a Suspension Bridge Girder”, Bjørn Isaksen, 2008:131, ISBN 978-82-471-8656-5 (trykt utg.) ISBN 978-82-471-8673-2 (elektro.utg.) ISSN 1503-8181.

“Cracking Risk of Concrete Structures in The Hardening Phase”, Guomin Ji, 2008:198, ISBN 978-82-471-1079-9 (printed ver.), ISBN 978-82-471-1080-5 (electronic ver.) ISSN 1503-8181.

“Modelling and numerical analysis of the porcine and human mitral apparatus”, Victorien Emile Prot, 2008:249, ISBN 978-82-471-1192-5 (printed ver.), ISBN 978-82-471-1193-2 (electronic ver.), ISSN 1503-8181.

“Strength analysis of net structures”, Heidi Moe, 2009:48, ISBN 978-82-471-1468-1 (printed ver.), ISBN 978-82-471-1469-8 (electronic ver.) ISSN1503-8181.

“Numerical analysis of ductile fracture in surface cracked shells”, Espen Berg, 2009:80, ISBN 978-82-471-1537-4 (printed ver.), ISBN 978-82-471-1538-1 (electronic ver.) ISSN 1503-8181.